ACTIVE CONTROL OF SURFACE PLASMONS IN HYBRID NANOSTRUCTURES

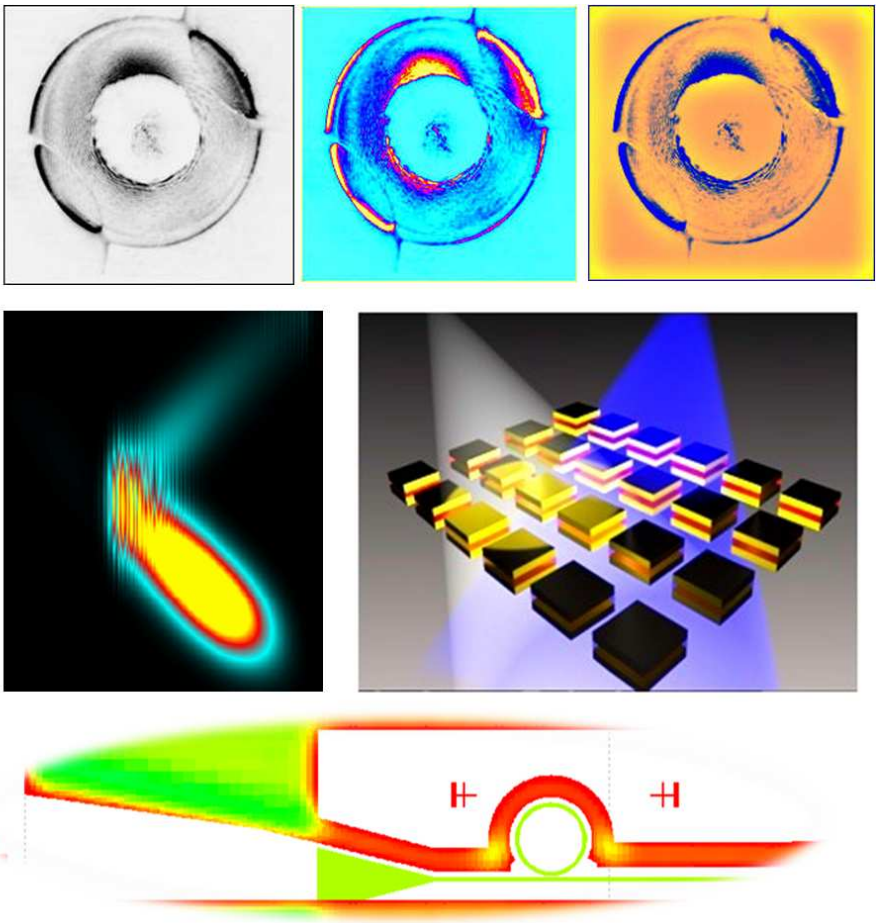

ACTIVE CONTROL OF SURFACE PLASMONS IN HYBRID NANOSTRUCTURES

Sukanya Randhawa

Thesis Advisor
Romain Quidant

Thesis Co-Advisor
Jan Renger

Dissertation Committee

President
Alain Dereux
Secretary
Valerio Pruneri
Member
Anatoly V. Zayats

Substitute Members
Gerasimos Konstantatos
Alexandre Bouhelier

ICFO, 2012

Institut de Ciències Fotòniques
Plasmon Nano Optics Group
Mediterranean Technology Park
Av. Carl Friedrich Gauss, num. 3
08860 Castelldefels (Barcelona), Spain
www.icfo.es

Abstract

Plasmonics nanostructures are becoming remarkably important as tools towards manipulating photons at the nanoscale. They are poised to revolutionize a wide range of applications ranging from integrated optical circuits, photovoltaics, and biosensing. They enable miniaturization of optical components beyond the "diffraction limit" as they convert optical radiation into highly confined electromagnetic near-fields in the vicinity of subwavelength metallic structures due to excitation of surface plasmons (SPs). These strong electromagnetic fields generated at the plasmonic "hot spots" raise exciting prospects in terms of driving nonlinear effects in active media.

The area of active plasmonics aims at the modulation of SPs supported at the interface of a metal and a nonlinear material by an external control signal. The nonlinear material changes its refractive index under an applied control signal, thereby resulting in an overall altered plasmonic response. Such hybrid nanostructures also allow for the creation of new kinds of hybrid states. This not only provides tools for designing active plasmonic devices, but is also a means of re-examining existing conventional rules of light-matter interactions. Therefore, the need for studying such hybrid plasmonic nanostructures both theoretically and experimentally cannot be understated.

The present work seeks to advance and study the control of SPs excited in hybrid systems combining active materials and nanometallics, by an external optical signal or an applied voltage. Different types of plasmonic geometries have been explored via modeling tools such as frequency domain methods, and further investigated experimentally using both near-field and far field techniques such as scanning near field optical microscopy and leakage radiation microscopy respectively. First, passive SP elements were studied, such as the dielectric plasmonic mirrors that demonstrate the ability of gratings made of dielectric ridges placed on top of flat metal layers to open gaps in the dispersion relation of surface plas-

mon polaritons (SPPs). The results show very good reflecting properties of these mirrors for a propagating SPP whose wavelength is inside the gap. Another passive configuration employed was a plasmonic resonator consisting of dielectric-loaded surface plasmon polariton waveguide ring resonator (WRR). Also, a more robust variant has been proposed by replacing the ring in the WRR with a disk (WDR). The performance in terms of wavelength selectivity and efficiency of the WDRs was evaluated and was shown to be in good agreement with numerical results.

Control of SPP signal was demonstrated in the WRR configuration both electro-optically and all-optically. In the case of electro-optical control, the dielectric host matrix was doped with an electro-optical material and combined with an appropriate set of planar electrodes. A 16% relative change of transmission upon application of a controlled electric field was measured. For all-optical control, nonlinearity based on trans-cis isomerization in a polymer material is utilized. More than a 3-fold change between high and low transmission states of the device at milliwatt control powers ($\approx$100 W/cm^2 intensity) was observed.

Beyond the active control of propagating surface plasmons, further advancement can be achieved by means of nanoscale plasmonic structures supporting localized surface plasmons (LSP). Interactions of molecular excitations in a π-conjugated polymer with plasmonic polarizations are investigated in hybrid plasmonic cavities. Insights into the fundamentals of enhanced light-matter interactions in hybrid subwavelength structures with extreme light concentration are drawn, using ultrafast pump-probe spectroscopy.

This thesis also gives an overview of the challenges and opportunities that hybrid plasmonic functionalities provide in the field of plasmon nano optics.

Resumen

Las nanoestructuras plasmónicas han adquirido una importante relevancia como herramientas capaces de manipular los fotones en la nanoescala, y pueden llegar a revolucionar un amplio abanico de aplicaciones tales como los circuitos ópticos integrados, la fotovoltaica o los dispositivos biosensores. Dichas estructuras hacen posible la miniaturización de los componentes ópticos más allá del "límite de difracción" de la luz, ya que convierten la radiación óptica en campos electromagnéticos fuertemente confinados en la proximidad de estructuras metálicas de tamaño inferior a la longitud de onda mediante la excitación de plasmones de superficie (SPs). Estos campos electromagnéticos tan intensos generados en los llamados "puntos calientes" plasmónicos brindan perspectivas muy interesantes para la generación de efectos no lineales en medios activos.

El área de investigación denominado plasmónica activa busca la modulación de los SPs sostenidos por la intercara entre un metal y un material no lineal mediante una señal de control externa. El índice de refracción del material no lineal cambia bajo la aplicación de la señal de control, lo cual da lugar a la modificaciión de la respuesta plasmónica. Estas nanoestructuras híbridas también hacen posible la aparición de nuevos tipos de estados híbridos, lo cual proporciona tanto herramientas para diseñar dispositivos plasmónicos activos como mecanismos que permiten re-examinar las reglas convencionales de la interacción luz materia. Por lo tanto, es necesario el estudio de dichas nanoestructuras plasmónicas híbridas de manera teórica y experimental.

En este trabajo de tesis se analiza el control de los SPs excitados en sistemas híbridos que combinan materiales activos y nanoestructuras metalicas mediante una señal óptica externa o un voltaje aplicado. Se han investigado distintos tipos de geometrías plasmónicas utilizando herramientas de simulación basadas en métodos en el dominio de la frecuencia, y posteriormente se han caracterizado experimentalmente dichas geometrías mediante técnicas de campo cercano y de campo lejano tales

como la microscopía óptica de campo cercano y la microscopía basada en pérdidas radiativas, respectivamente. En primer lugar se estudiaron elementos plasmónicos pasivos, en particular espejos plasmónicos dieléctricos que demuestran la capacidad que tienen las redes periódicas de caballones de material dieléctrico colocados sobre una superficie metálica plana para abrir intervalos prohibidos en la relación de dispersión de los plasmones de superficie propagantes o plasmones-polaritones de superficie (SPPs). Los resultados muestran que dichos espejos poseen muy buenas propiedades reflectantes para SPPs cuya energía está en el intervalo prohibido. Otra configuración pasiva analizada fueron los resonadores plasmónicos basados en anillos de guía de onda plasmónica fabricada a partir de estructuras dieléctricas sobre metal (WRR, del inglés *waveguide ring resonator*). Asimismo, se propone una versión más robusta de resonador plasmónico, basada en la sustitución del anillo del WRR por un disco (WDR, del inglés *waveguide disk resonator*). Se ha evaluado el funcionamiento de los WDRs en términos de selectividad en longitud de onda y de eficiencia, y los resultados obtenidos presentan un buen acuerdo con las predicciones numéricas.

Pasando a las configuraciones activas, se demuestra el control de la señal plasmónica en configuración WRR por medios tanto electro-ópticos como completamente ópticos. En el caso del control electro-óptico, el material dieléctrico que compone el WRR estaba dopado con un componente electro-óptico y a la estructura pasiva se le añadio un conjunto de electrodos planos. Bajo la aplicación de un campo eléctrico externo, se midió un cambio relativo en la transmisión a través de la guía plasmónica del 16%. En cuanto al control puramente óptico, se utilizó la no linealidad de un material polimérico con origen en una isomerización trans-cis. En este caso se detectó un factor 3 entre los estados de alta y baja transmisión del dispositivo con potencias de control del orden de milivatios (intensidad del haz óptico de control de unos 100W/cm^2 aproximadamente).

Además del control activo de los plasmones de superficie propagantes, la utilización de nanoestructuras plasmónicas que poseen resonancias plasmónicas localizadas puede dar lugar a nuevos fenómenos. En esta tesis también se han estudiado las interacciones entre las excitaciones moleculares en un polímero pi-congujado con las polarizaciones plasmónicas en nanocavidades plasmónicas híbridas. Utilizando espectroscopía de

tipo bombeo-sonda con pulsos ultrarápidos, se han analizado diversos aspectos del aumento en la interacción luz-materia para estructuras híbridas de dimensiones inferiores a la longitud de onda sometidas a concentraciones de luz muy altas.

Por último, esta tesis también proporciona una visión general de los desafíos y posibilidades que las funcionalidades plasmónicas híbridas ofrecen en el campo de la nano-óptica basada en plasmones de superficie.

Acknowledgements

This PhD would not have been possible without the support I received from different people in various forms during the course of these four years.

I am ever so grateful to my adviser Prof. Romain Quidant for giving me the opportunity to work in his group. Your novel ideas and perceptive approach during many enjoyable discussions have always been inspiring. Thanks for being so encouraging and supportive throughout these years, and for having played a key role in shaping my scientific career. I would like to thank my co-advisor Dr. Jan Renger for his insightful discussions and tremendous support, which have been instrumental in guiding me. Your discerning eye for detail, coupled with your good humor, made my PhD years so enjoyable and memorable. Also, I am very grateful to Dr. María Ujué González for being such a wonderful and thorough teacher of plasmonics during my first year at ICFO. I cannot thank you enough for your warm nature and extraordinarily helpful spirit, and for always being there.

Collaborations with several scientific groups during these years have been both enriching and enjoyable. I would like to thank all of my collaborators in the PLASMOCOM project as they have contributed in one way or another to the work presented here. Thanks to Dr. Alexey Krasavin for many intense discussions and to Dr. Tobias Holmgaard, Prof. Anatoly Zayats and Prof. Sergey Bozhevolnyi for various types of support and collaboration. I would also like to thank Sébastian Lachèze and Prof. Alexandre Bouhelier from l'Université de Bourgogne, Dijon, for their contributions. I would like to thank Prof. Stefan Enoch for access to his FMMDVL code for simulations, and several useful discussions. I would like to thank Dr. Gary Wiederrecht for giving me the opportunity to collaborate with his group in the Center for Nanoscale Materials, for all the encouragement and support during my research stint at Argonne National Labs, and for introducing me to the world of ultrafast spec-

troscopy. I would also like to thank Dr. Leo Ocola for being a fantastic advisor in the cleanroom, and Dr. Matt Pelton for many insightful discussions. This would not have been possible without the kind support from the BE-AGAUR scholarship, who sponsored my research stint at ANL. Besides, my heartfelt thanks to the others there who made my research stint productive yet fun, especially Dr. Ralu Divan, Dr. Daniel Rosenmann, Dr. Dave Gostola, Carrie Clark and many others. I would like to acknowledge the support from Dr. Xavier Elias Pera and Rafael Betancur at ICFO in providing me the polymer material for the mini-MIMs project.

I cannot thank Dr. Canek Hernandez enough for his support during my short stint at Georgia Institute of Technology, teaching me the tricks of polymer fabrication and characterization, and more so being a wonderful person to work with. I would also like to thank my advisor there, Prof. Bernard Kippelen, for giving me the chance to collaborate with his lab.

I am grateful to my current advisor Prof. Norbert Scherer at the University of Chicago for his patience and understanding towards the completion of my thesis. I acknowledge the financial support from him through the National Science Foundation (Grant CHE-1059057).

I would like to thank all the former and current members of the Plasmon Nano-Optics group at ICFO for an enjoyable and inspiring atmosphere. Dr. Guillaume Baffou, Dr. Mark Kreuzer, Dr. Matthieu L. Juan, Srdjan Aćimović, Jean Cesario, Dr. Maurizio Righini, Dr. Petru Ghenuche, Jan Gieseler, Michael Geiselmann, Jon Donner, Dr. Giorgio Volpe, Valeria Rodríguez Fajardo, María Alejandra Ortega, Dr. Sudhir Cherukulappurath, Dr. Christopher Galloway and Esteban Bermúdez Ureña. Having been a part of such a culturally diverse group, I have learnt a lot from each of one of you, be it during work hours or outside of it.

An important part of the daily research at ICFO is the solid support group for the technical research. I would like to thank Luis Enrique Romero and Francisco Javier Pérez Díaz for being excellent support in the cleanroom. A big thanks to everyone at the electronic workshop and IT support as well.

Finally, my heartfelt thanks to all the people at ICFO administration, especially Manuela Furkert, Anne Gstottner and Maria del Mar Gil Sanchez. I thank several other individuals who at some point have worked with me, and were a significant part of my research experience.

I feel so lucky to have done my PhD in an active and dynamic research environment at ICFO, which has not only been an excellent foundation, but also a great place to make friends from all over the globe.

I would like to thank all my friends and well wishers for their support. My special thanks to Susheel Sekhar for his unstinting support.

Even an iota of this would not have been possible without the unconditional love, support and cool genes of my beloved parents Alka and Kulbir, and my dear brother Guntaj.

Contents

Chapter 1

Introduction

1.1 More Control over Light

Optics is that branch of physics that involves the study and analysis of the behavior and properties of light. Light is, at once, both obvious and mysterious. It bounces off the skies of the Earth and interacts with material objects in its varied ways, some of which our senses can perceive. Light propagates through empty space, and through its many interactions, provides visual information about our world. When a sunbeam angles through a dust-filled room, or when a rainbow appears after a brewing storm, or when a drinking straw appears disjoint in a glass of water, we are provided with glimpses of its nature. The familiar effects of reflection, refraction, diffraction, absorption and scattering are evident in a wide variety of our visual experiences, from the focusing of light through a simple lens, to the colors of the rainbow.

Based on our understanding of light-matter interactions in different solids, the field of optics, in recent times, has been witnessing a surge in interest due to its many applications in diverse areas of science and technology. For instance, colorful gemstones such as rubies and sapphires are employed in high power lasers as gain media. Also, inorganic and organic materials have been used extensively as active media in the modern opto-electronics industry. Another burgeoning area is that of plasmonics, which pertains to the interaction of light with metals, be they nanoscale thin films or particles, with applications ranging from energy conversion to spectroscopy, waveguiding to cancer research.

The historical background behind the emergence of the field of plasmonics can be attributed to the following reasons. Since the middle of the

last century, electronics and telecommunications industries have ushered in an era of continued growth in technology and development. While the microelectronics industry of yesteryears has been relying mostly on electrons, information transmission over large distances has been revolutionized by the use of light as an information career, since photons interact only weakly with each other and with dielectric materials such as glass fibers. This weak interaction leads to less attenuation and lays the foundation for the success of fiber optic communications, which has made it possible to send optically encoded data at rates of terabits per second over thousands of kilometers, with minimal signal distortion. Even though the focus today is more on photons rather than electrons, both industries are now simultaneously facing a fundamental challenge relating to the size of electronic and photonic integrated components, which have reached the dimensions of electron and light waves, respectively. To close the size gap between microelectronic and photonic integrated devices, the fundamental block posed by the *diffraction limit* must be overcome. According to this limit, it is not possible to localize or focus a three-dimensional light beam to a lateral size smaller than about half its wavelength in the given material. In the context of opto-electronics, this opposes the creation of dielectric waveguides or fibres that can confine the guided light or an optical signal to a lateral dimension smaller than a couple hundred nanometres, in visible and near-IR region. In biology, the diffraction limit hampers the detection of ultra-small concentrations of molecules in the cell by limiting the focusing power of conventional lenses [1]. In this context, plasmonics enables the confinement of light into volumes smaller than the diffraction limit, for instance, inside the dielectric gap between two metallic nanoparticles. In this way, plasmonics not only provides a synergy between the photonics and electronics, but also acts as a promising tool to explore new phenomena at subwavelength scales.

1.2 Plasmonics: A Tool for Sub-Wavelength Light Control

Surface plasmons (SP) are coherent electron oscillations (in response to incident light) that exist at the interface between two materials, where

the real part of the dielectric function changes sign across the interface (e.g. a metal-dielectric interface). These couple with a photon to create a quasi-particle called a Surface Plasmon Polariton (SPP) in case of extended metallic films or localized surface plasmon (LSP) in case of nanosized metallic particles. The strong confinement of these waves along the interface has been of tremendous interest for the realization of ultra-compact photonic circuits, and for the closing of the miniaturization gap between photonics and nanoelectronics, mentioned in the previous section.

The first documented observation of surface plasmons dates back to 1902, when Wood illuminated a metallic diffraction grating with polychromatic light, and noticed narrow dark bands in the spectrum of the diffracted light, which he referred to as anomalies [2]. Theoretical work by Fano [3] concluded that these anomalies were associated with the excitation of electromagnetic waves on the surface of the diffraction grating. Later, pioneering work by Otto, Kretschmann and Raether [4–6] established a convenient method for the excitation of surface plasmons and their investigation, thus extending surface plasmons to modern optics.

Up until the 1980s, interests in metallic structures that sustain SPs, such as flat films and metal nanoparticles, have mostly been confined to the physical sciences. Since then, the ability of SPs to squeeze light into deep sub-wavelength volumes has rendered them useful in a vast array of interdisciplinary nanophotonic technologies and research endeavors, such as surface-enhanced Raman scattering [7] and biosensing [8–10]. One of the earliest landmarks has been the demonstration of single-molecule Raman sensing on roughened Ag surfaces [11, 12].

More recently, renewed interest in SPs has been energized by the advancements in nano-fabrication tools, such as electron-beam lithography and ion-beam milling etc. Chemical synthesis of colloidal metallic nanoparticles has also been developed, leading to easier implementation and access to different sizes of nanoparticles (as small as $\sim$ 5nm), and more severe control over their structure and crystalline properties in three dimensions. Besides, the development of more sophisticated electromagnetic modeling techniques have made it possible to numerically predict the optical properties of metallic nanostructures in various types of materials (linear

or nonlinear). All these have allowed for the creation of metallic micro- and nanostructures with designed functionalities, enabling plasmonics at subwavelength scales. The development of scanning near-field optical microscopy [13] and other advanced optical/electronic microscopies (for e.g. nonlinear microscopy, Photo Electro Energy Microscopy (PEEM), Electron Energy Loss Spectroscopy (EELS), Cathodoluminescence) has further empowered the field of plasmonics. These advances enable us to enter the realm of nanophotonics which is otherwise inaccessible to conventional optics due to diffraction limits.

However, in order to use the plasmonic configurations for many applications, it is important to be able to control the optical properties of surface plasmons. One way of achieving this is in conjunction with nonlinear materials that allow active modulation of their properties, and hence alter the overall plasmonic response in a unified configuration. A brief introduction about nonlinear materials is presented in the next section.

1.3 Nonlinear Materials

In general, the optical response of a material can be explained by a small set of parameters, including the polarizability and refractive index. Other important properties include light intensity, propagation direction, frequency or wavelength spectrum, polarization, and speed (3×10^8m/s in vacuum). Under normal conditions, the material parameters are constants for a given light frequency, independent of the intensity. This is the realm of linear optics, where the optical response of the material is linearly proportional to the intensity of light.

The magnitude of the electric field that binds an electron to an atom is typically around 10^{10}-10^{11}V/m. When the electric field of light is comparable to this value, nonlinear effects in materials can be induced. Such electric field magnitudes are generated when the optical intensities are of the order 10^{19}W/m^2. At such high intensities, the standard optical properties of a material, such as its refractive index at a particular frequency, cannot be considered constant anymore as they become functions of the light intensity. The optical response, in this regime, becomes nonlinear.

The invention of laser gave rise to the study of light-matter interaction at higher intensities, uncovering new phenomena not generally seen under normal conditions, such as the generation of new colors from monochromatic light in a transparent crystal, and the self-focusing of an optical beam in a homogeneous liquid.

Alternatively, it is possible to produce a sizeable nonlinear effect at much lower intensities due to cumulative nonlinear effects in very large number of atoms. This works when the nonlinear phenomena in individual atoms are in phase with each other (phase-matching). A more detailed description on nonlinear effects is presented in the next chapter.

Plasmonic effects are associated with high electromagnetic fields which enhance the nonlinear effects. Therefore, when nonlinear materials are integrated in plasmonic devices, they open up a possibility to control the overall plasmonic response.

1.4 Motivation

By coupling plasmonic modes to appropriately chosen active materials, *active* plasmonic devices can be designed for real-life applications demonstrating basic functionalities such as signal switching, modulation, amplification to compensate for losses, and the electrical generation and detection of plasmons. There have been preliminary demonstrations of the control of plasmonic excitations using all-optical [14], electro-optical [15], thermo-optical [16], and magneto-optical [17,18] techniques. These initial efforts have opened up the field for more exciting configurations, paving the way for a host of new devices with novel applications.

The motivation behind this thesis is to develop hybrid plasmonic components, e.g. plasmonic nanostructures that are hybridized with functional materials, to enable the control of SPPs. Design of such components is achieved through study of mixed (hybrid) modes by observing the interactions between metals and active dielectrics. These not only have various interesting applications, but they also aid in the understanding of the properties of such hybrid systems.

For the large part, nonlinear organic materials (NLO) have been used within the framework of this thesis. NLO materials have an advantage over crystalline inorganic materials as active chromophores in that the former can be optimized to increase their optical nonlinearity, thus enabling large hyper-polarizabilities. Also, NLOs can be readily integrated with semiconductor electronics and fiber optic transmission lines for future applications in energy conversion via optoelectronic devices and optical computing.

1.5 Objectives

This study focuses on acquiring a fundamental understanding for the development of hybrid plasmonic nanostructures towards the generation and active control of SPPs. Further, the active response of different nonlinear materials, in combination with several plasmonic geometries is studied using different control mechanisms. The thesis is organized as follows:

- **Chapter 2 - Active Plasmonics: The Fundamentals** A short introduction that explains the fundamental properties of surface plasmons is presented. The critical criteria for developing an active plasmonic functionality, combining active materials and plasmonics, is also discussed.
- **Chapter 3 - Passive Control I: Dielectric SPP Bragg Mirrors** Before extending the investigation to active plasmonic configurations, it is important to fully understand and develop passive plasmonic geometries. One such system is the dielectric SPP mirror, which shares analogies with the conventional optical Bragg stacks for propagating waves. In this study, the ability of gratings made of dielectric ridges placed on top of flat metal layers to open gaps in the dispersion relation of SPPs is analyzed both experimentally and theoretically. Also, the performance of these dielectric gratings as SPP Bragg mirrors is demonstrated.
- **Chapter 4 - Passive Control II: Dielectric-loaded Plasmonic-coupled Resonators** Next, the details of a second passive proto-

type, i.e. dielectric-loaded plasmonic waveguide (DLSPPW) based-coupled resonator system, are presented. Our approach is based on the plasmonic waveguide ring and disk resonators (WRR/WDR). In particular, a detailed experimental analysis of plasmonic WDRs operating at telecom wavelengths, using near field optical microscopy, is presented. The effects of critical parameters, such as the ring radius and the gap between the waveguide and the ring, on WDR characteristics are discussed.

- **Chapter 5 - Active Control I: Electro-active Plasmonic Component** After the detailed study of passive geometries, the transition towards active configurations is made by incorporating active materials, in hybrid plasmonic systems. In this chapter, the characteristics of an electro-optical DLSPPW WRR are presented. By doping the dielectric host matrix with an electro-optical material, and by designing an appropriate set of planar electrodes, a 16% relative change in the transmission is observed, by electrical control. The temporal response of the device is analyzed, and conclusions pertaining to the dominant role played by the electrostriction of the host matrix in the transmission response are drawn.

- **Chapter 6 - Active Control II: All-Optical Plasmonic Functionalities** Experimental and numerical analysis of a compact and efficient optically tunable plasmonic component, utilizing an DLSPPW WRR with the nonlinearity based on *trans-cis* isomerization in a polymer, are presented. Additionally, modulation of the LSP signal in a dimer configuration covered with an active layer is explored. The active polymer in both cases is realized by doping the host matrix (Poly Methyl Methacrylate: PMMA) with DR1 molecules, providing large changes in the refractive index due to the trans-cis isomerization, when pumped with light near the absorption resonance. In the case of DLSPPW WRR, transmission changes by a factor of 4 are observed between high and low transmission states of the device, at milliwatt control powers (100W/cm^2 intensity), with the performance limited by the slow relaxation of the disperse red 1 (DR1) molecules (cis-trans).

- **Chapter 7 - Active Control III: Hybrid Plasmonic Nanoresonators** In this chapter interactions of molecular excitations within a π-conjugated polymer with plasmonic polarizations are investi-

gated in hybrid plasmonic cavities. The active polymer has been integrated in the Metal-Insulator-Metal (MIM) cavity and an array of such hybridized cavities, so called mini-MIMs, were characterized using transient absorption spectroscopy which allows for the observation of the interactions in 'real time'. The resonances of such hybrid cavities could be tuned based on the length of the cavity, the core refractive index and the core thickness. Strong field confinement inside the core results in enhanced sensitivity of the mini-MIM resonance to the changes in the polymer under the influence of the pump pulse. The pump drives a nonlinear change in the polymer core whereas the probe pulse feels the altered optical response of the system. Strong spectral shifts in the mini-MIM transient signature accompanied by novel narrowing at early times are observed.

Chapter 2

Active Plasmonics: The Fundamentals

2.1 The Optical Properties of Metals

A review of the free electron contribution to the optical properties of metals begins with the Drude model of free electrons [19], which describes the kinetics of the interaction between a free electron cloud and the crystal lattice of the metal (electron-phonon interaction). This model describes the response of the electron cloud to an oscillating electric field, and can, therefore be used to model the response of a metal to light (assuming light to be an electromagnetic wave). However, according to the classic Drude model, the plasma frequency alone should dictate the optical appearance of metals. This model explains the optical properties of many metals (e.g. zinc), but does not account for the reddish appearance of copper, or the yellowness of gold or the colorlessness of silver. That is because the optical properties of these metals are characterized by an edge in their reflectance spectrum due to interband transitions of the bound electrons from the d-band to the empty states above the Fermi level (over a fairly narrow band of energies), which can be modeled by a simple Lorentz oscillator. For gold and copper the onset of interband transitions occurs in the visible spectrum and extends to higher frequencies, while for silver, the onset occurs in the ultra-violet spectrum. This can also be verified in the optical response for these metals where individual absorption peaks can be calculated from the respective band models. [20, 21].

Thus, the combined effects of the free electrons (Drude model) and the bound d-electrons (Lorentz model) influence the optical properties of metals. According to the modified Drude model which accounts for the contributions from both bound and free electrons, the complex dielectric

permittivity or dielectric constant (ϵ) can be expressed as:

$$\epsilon = \epsilon_B + \frac{\omega_p^2}{\omega^2} + i\frac{\omega_p^2\Gamma}{\omega^3} \tag{2.1}$$

where, ϵ_B is the sum of the interband contributions (bound electrons), ω_p is the bulk plasma frequency, and Γ is the damping constant. In a metal, the damping term describes the electron collision rate, which is the inverse of the mean electron collision time (τ), i.e. $\Gamma = \tau^{-1}$. Experimental work on a variety of metals has shown Γ to be modified by a frequency dependent term β [22–25]:

$$\Gamma_{\text{mod}} = \Gamma + \beta\omega^2 \tag{2.2}$$

where ω is the angular frequency. This frequency-dependent term is significant near the infrared and visible portions of the spectrum for noble metals, which are the areas of interest in many of the topics covered in this study.

The modified Drude model predicts the optical behavior of metals fairly well. It shows that the permittivity becomes negative below the bulk plasma resonance, i.e. ω_p characteristic of each metal, while above the resonance, the permittivity is positive. In other words, below the resonance frequency, the incident electromagnetic waves oscillate slow enough for the electrons to follow. This enables the metal to behave as a good conductor as the induced electron currents or oscillations cancel out the incident waves, making them excellent reflectors. However, above the resonant frequency, the inertia of the electrons prevents in-phase oscillations. Therefore, the currents cannot be excited properly to eliminate the incident wave, and the metal is rendered transparent, with additional properties of being dispersive and lossy for the wavelengths that it transmits.

The spectral region where the metal permittivity is negative, i.e. below the bulk plasma resonance, is of more interest in the context of surface plasmons, as $\epsilon < 0$ is an important criterion for the existence of a surface plasmon mode. The origin and properties of surface plasmons, and their relevance to passive and active plasmonic-based applications are the subjects of the next sections.

2.2 Surface Plasmons: Extended vs. Localized

Surface plasmons are quantized electromagnetic surface waves that are localized at the interface between a plasma (in this case metal) and a dielectric material [26]. According to Maxwell's theory, electromagnetic surface waves can propagate along the metallic surface or film. These transverse magnetic waves, which are solutions to the Maxwell's equations propagate along the metal-dielectric interface at a broad spectrum of eigen frequencies, ranging from $\omega = 0$ to $\omega_p/\sqrt{2}$ and have a fixed wave vector (κ). However, for these surface modes to exist at the interface of the two media, having frequency dependent complex dielectric functions ϵ_1 and ϵ_2, the real part of the dielectric functions of the two media must be of opposite signs. Typically, a polariton is an electromagnetic mode related to the oscillation of the polarization charge density. In the case of metal interfaces, where the polarization charge density oscillations correspond to the oscillations of the electrons, the surface polariton is called a surface plasmon polariton (SPP).

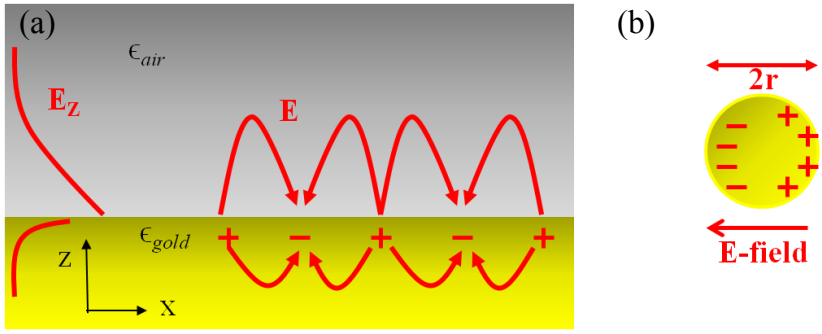

Figure 2.1: *(a)Surface plasma oscillations at the surface of an extended (planar) metal-dielectric interface; (Inset)Schematic of the electric field intensity associated to a SPP propagating at this interface; (b)Surface plasma oscillations localized in a metallic nanoparticle*

As shown in Fig. 2.1(a), the wave is assumed to be propagating along the x-direction. The strong localization of the electromagnetic field of SPPs to the interface is characterisitic of surface waves. These fields are evanescent, decaying exponentially perpendicular to the surface, i.e. in the z-direction (Fig. 2.1(a)). The decay length into the metal is comparable to the skin depth, while the decay into the dielectric is of the order

of 100nm in the visible.

The SPP dispersion relation is given by:

$$\kappa_{\mathrm{SPP}} = \frac{\omega}{c}\sqrt{\frac{\epsilon_1\epsilon_2}{\epsilon_1+\epsilon_2}} \tag{2.3}$$

with κ_{SPP} and c being the in-plane wave vector of the SPP, and the speed of light, respectively. The dispersion curve for SPPs propagating at the interface between a Drude metal and a dielectric is shown in Fig. 2.2. These modes lie on the right side of the light line ($\omega = c\kappa_x$), which indicates that they have a larger wave vector than light waves of the same energy ($\hbar\omega$). At low frequencies, SPPs have a very photon-like character, and the dispersion relation lies close to the light line, whereas at higher frequencies SPPs deviate further from the light line, towards larger wave vectors. Since these modes are non-radiative by nature, they can be excited by light only if the momentum mismatch is compensated through a suitable coupling technique. A periodic grating or a subwavelength scatterer, such as a groove or a slit in the metal, is commonly used for the excitation of SPPs [6]. Additional methods, such as the classic attenuated total reflection technique to couple evanescent field components to SPPs [4, 27], or via electron irradiation, have also been used [28, 29].

As a part of the SPP field propagates in the metal, it is attenuated by Ohmic losses, which increase for wavelengths that are close to the surface plasmon resonance. The intensity decreases as $e^{-2\kappa''_{\mathrm{SPP}}}$, where κ''_{SPP} is given by:

$$\kappa''_{\mathrm{SPP}} = \frac{\omega}{c}\sqrt{\left(\frac{\epsilon_1\epsilon_2}{\epsilon_1+\epsilon_2}\right)^3}\frac{\epsilon''_1}{2\epsilon_1^2} \tag{2.4}$$

Here, κ''_{SPP} and ϵ''_1 are the imaginary parts of κ_{SPP} and ϵ_1, respectively. The propagation length, L_{SPP}, beyond which the intensity decreases to $1/e$, is given by:

$$L_{\mathrm{SPP}} = 2\kappa''_{\mathrm{SPP}}{}^{-1} \tag{2.5}$$

Close to the visible spectrum ($\lambda = 800$nm), SPPs on a Au surface can propagate on the order of 25μm, and this increases in the near-infrared

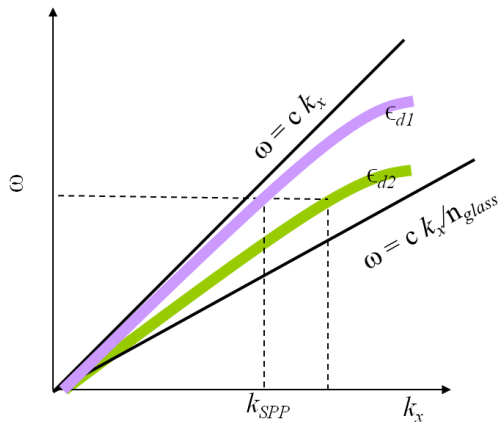

Figure 2.2: *Sketch depicting the dispersion relation for SPP propagating at the metal-dielectric interface. A change in the dielectric constant of the dielectric material from ϵ_{d1} to ϵ_{d2} changes the dispersion curve from purple to green. The light line in vacuum and in glass are shown in black.*

region to approximately 60μm. Besides the spatial decay of the SPPs along the propagation direction, the temporal decay time (T_{SPP}) can also be of interest, and is measured to be $\approx$ 626fs for a Au film, at $\lambda = 800$nm.

While SPPs occur at extended metal interfaces, charge density oscillations confined to metal nanoparticles and metal clusters, are called localized surface plasmons (LSPs)(see Fig. 2.1(b)). These collective oscillation of the conduction electrons are responsible for the distinctive colors of metal particle solutions. A quantitative explanation of the color of metal particles in a solution was given by Mie in 1908 [30]. Mie's theory allows the extinction spectra of spherical particles to be calculated from the dielectric constants of the metal and the surrounding medium.

The excitation of LSPs by an electromagnetic field (light), at an incident wavelength where the resonance occurs, results in strong light scattering and the appearance of strong absorption bands both in the far field and near field. This also corresponds to an intense enhancement of the local electromagnetic fields in the near-field of the particle. The dipolar LSP modes, in contrast to SPPs, can be excited easily as they can couple with the radiation modes. The optical properties of metal nanoparticles

have played a key role in the development of physical chemistry and nanotechnology.

2.3 Plasmon Sensitivity to Refractive Index Change

Due to the strong confined electromagnetic field of surface plasmons (SP)[1] to the metal surface, SPs are sensitive to any perturbation at the surface, allowing for an extensive tuning of both the spectral properties and the associated electromagnetic field distribution by engineering an appropriate structural design. Any minor change to the refractive index of materials in close proximity to the metal, or conversely that of the supporting metal, could alter the plasmonic mode conditions and hence the mode distribution, thereby effecting SP propagation. Figure 2.2 shows the modification of the dispersion relation for slight changes in the refractive index of the dielectric at the interface with a metal, according to Eq. 2.3. Due to the increase in the refractive index of the dielectric at the interface, the in-plane momentum of the modes also increases, which moves further to the right of the light line.

Alternatively, changes can also be induced by structuring the metal/dielectric interface of the geometry. One such strategy relies on the interaction of SPs with scattering defects and the design of periodic corrugated structures. Based on this principle, one- and two-dimensional gaps in the SPP dispersion relation can be engineered, and SP optical elements such as Bragg mirrors and demultiplexors, among others, can be obtained. The design of prisms and lenses based on the refraction induced by the surface corrugation is also possible. Figure 2.3(a) shows the the dispersion relation for a planar layered system consisting of a 50nm-thick Au film, covered by a 100nm-thick dielectric ($n = 1.49$) film, as shown in the inset. As a comparison, Fig. 2.3(b) depicts what happens when the 50nm-thick Au surface is instead covered by a structured dielectric layer for a wave incident perpendicular to the grating lines. The dielectric layer consists of a grating of ridges of height $h = 100$nm and width $d_1 = 150$nm, separated by air gap of width $d_2 = 205$nm, as shown in inset.

[1] SP refers to both SPPs and LSPs

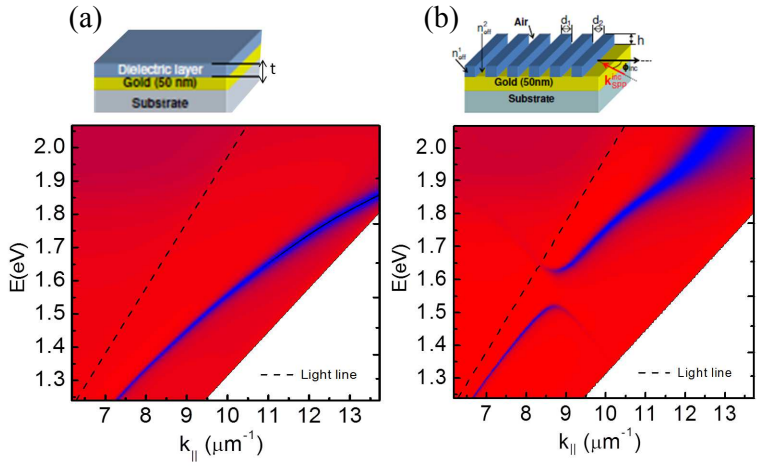

Figure 2.3: *(a)Reflectivity map for a layered system consisting of a 50nm-thick Au film covered by a* $100nm$*-thick dielectric* ($n = 1.49$) *film as shown above. The SPP dispersion curve is clearly visible in blue; (b)Reflectivity map of a* $50nm$ *thick Au surface covered by a structured dielectric layer for waves incident perpendicular to the grating lines. The dielectric layer consists of a grating of ridges of height* $h = 100nm$ *and width* $d_1 = 150nm$ *separated by air* ($d_2 = 205nm$)*, as shown in the schematic above, where the* $\kappa_{\mathrm{SPP}}^{inc}$ *corresponds to the SPP wave vector incident on the grating, and* ϕ_{inc} *represents the angle of incidence.*

LSPs are also very sensitive to changes in size, shape, size distribution of the nanoparticles and their environment. This property of LSPs is well-known and along with that of SPPs, has been exploited for years in the field of sensing, which utilizes metal nanoparticles for the construction of LSP-based sensors. Figure 2.4 shows a spectral shift in the LSP resonance for a dimer configuration (in an array) with a gap of $\approx$ 10nm (originally in air) when covered with a polymer layer ($n = 1.5$). Dimers are particularly sensitive to any changes that occur at the gap where the mode is confined [31].

Therefore, the sensitive nature of surface plasmons enables control over

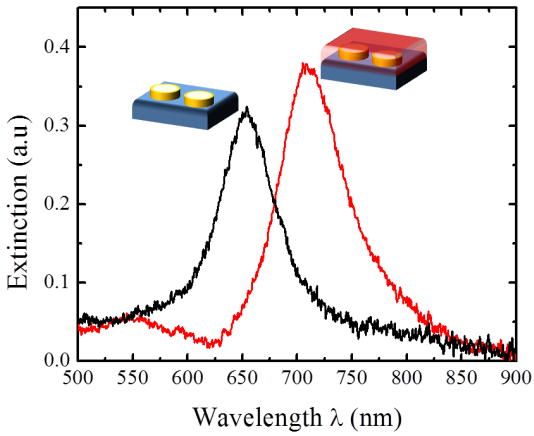

Figure 2.4: *Extinction spectra of dimers with gap* $\approx 10nm$ *with the peak corresponding to the plasmonic resonance recorded experimentally for an array of dimers in air and in a dielectric with* $n = 1.5$

the propagation, which is useful for building an active plasmonic functionality. Such a functionality offers the advantage of full on-a-chip integration due to the intrinsically two-dimensional nature of SPs. In additions, the compact size of SP-based-devices enables one to overcome the diffraction limit and opens a route to a vast plethora of new-age nanophotonic studies and applications.

2.4 Control of SPPs - Background

Different methods for controlling the propagation of surface plasmons (specifically SPPs) have been analyzed in the past. This has been an extensive area of research in the recent years, as it provides a valuable platform for achieving compactness and a high level of integration of photonic devices compatible with current electronic architectures [32, 33]. The control of the surface plasmon field is usually obtained by structuring the metal surface supporting the SPPs. Passive elements, such as waveguides [34, 35], routers [36–38], multiplexers [39] and more advanced devices [40], have been successfully integrated in planar all-

metal configurations.

Alternative strategies rely on the interaction of SPPs with scattering defects and the design of periodic corrugated structures. Based on such principles, gaps in the SPP dispersion relation can be engineered [41–44] and SPP optical elements such as Bragg mirrors [45–47], demultiplexors [39] and plasmonic crystals with guiding channels [48–50], can be obtained. The design of prisms and lenses based on the refraction induced by arrays of surface corrugation is also possible [51]. Another approach, based on the use of dielectric loads on top of the metallic layer to alter the effective index of the propagating SPPs, has been used in tandem with the application of the same refraction laws as in conventional optics, and different elements, such as lenses [35], prisms [52, 53], in-plane Fresnel zone plates [54, 55] or waveguides [38, 56] have been designed.

More recently, demonstrations of active plasmonic functionalities were reported in prototype devices fabricated on a wide range of supports, including optical and electrical SPP modulations [14, 15], ultrafast responses [57], transistor-like elements [58], and plasmon-based lasers [59]. These demonstrations, however, are currently not compatible with existing CMOS industrial standard, and an alternative technology is therefore required to integrate active devices. Recently, a series of publications showed the potential of dielectric-loaded SPP waveguides (DLSPPW) to implement a plasmonic circuitry integrated on a Si architecture [60, 61]. Passive manipulation [62], loss compensation [63], power monitoring [64] and thermal control [16] are already part of DLSPPW subunits. Moreover, DLSPPWs have proven to be an efficient means of guiding and manipulating plasmonic signals due to the strong confinement of the plasmonic mode within the dielectric. This strong confinement within the dielectric renders the plasmonic mode sensitive to the refractive index changes in the dielectric, and hence, making it attractive for active control.

2.5 Hybrid Plasmonic Devices

The area of active plasmonics brings together nonlinear materials, which provide a change in refractive index under a given control signal, and

subwavelength plasmonic structures, which can convert optical radiation into intense, engineered, strongly confined field distributions. Such a combination can also be referred to as a hybrid nanostructure, as it allows for the creation of new kinds of hybrid states, i.e. excitations due to the mixing of distinct types of materials (e.g. plasmons and excitons). These are not only tools for designing active plasmonic devices but also an exciting opportunity to re-examine the existing conventional rules of light-matter interactions.

Exploiting the sensitivity of SPs to changes in its surrounding media (as discussed in previous sections), it is possible to achieve active control of SPs by realizing hybrid plasmonic components, which combine active organics and metallic nanostructures. As highlighted before, this is a step towards designing active devices that demonstrate basic functionalities, such as switching, lasing, energy storage and conversion. However, to reach the go for this purpose, it is important to be able to couple plasmonic modes to appropriately chosen active materials. The aim of this research has been to develop hybrid plasmonic systems, that is a system sustaining SP, coupled to an active material allowing its modulation. Depending on the application and desired modulation and timescale, a suitable active material is selected and implemented in an optimized plasmonic configuration.

If one were to broadly classify the different underlying aspects that mark the development of a hybrid plasmonic system, two distinct parts could be easily identified as shown in Fig. 2.5. One first needs to choose a suitable active material, which is determined by many factors, such as the type of modulation desired, the nature of the nonlinearity, its potential, and its availability. Another important aspect is to select and recognize the best SP geometry or device configuration, which incorporates the chosen active material. Several passive configurations that have been recently explored and implemented offer a good platform for building active devices that extend the functionality of the passive ones to active control. Understanding the workings of a passive plasmonic device is crucial before its combination with an active material. This requires a thorough analysis of the optical response of a system, both near- and far-field, with respect to different system parameters, such as the geometry and composition. The extent to which these parameters can be tuned to

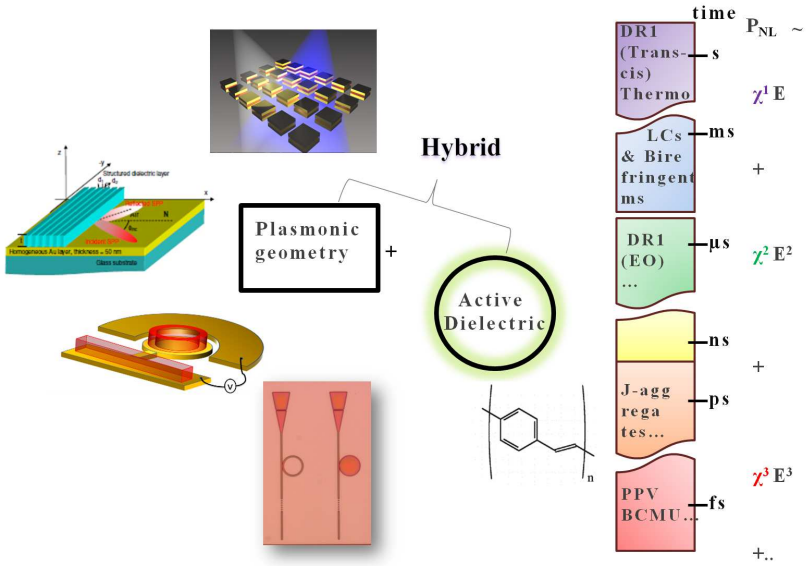

Figure 2.5: *A hybrid plasmonic system combines a sensitive plasmonic geometry with an active dielectric layer. Different plasmonic configurations developed within the framework of the thesis are shown on the left (a)Mini-MIMs (b)Dielectric SPP Bragg mirrors (c)Waveguide ring resonator (WRR) with electrodes (d)WRRs and WDRs (disks) on planar Au. On the right, different options for active materials are arranged vertically having different timescales of the nonlinearity. They are also classified based on the type of nonlinearity as shown by the nonlinear equation.*

achieve an optimal optical response with respect to the interaction with the the active molecular layer(s) is key to this analysis.

In order to accomplish the goal of fabricating a hybrid plasmonic component that provides control of SPs, various approaches were studied in parallel, where the possibilities of combining active materials with different potential SP device geometries have been explored. In the subsequent sections the details are elaborated.

Figure 2.6 provides a more detailed framework describing the general process for developing an active SP functionality. A plasmonic device

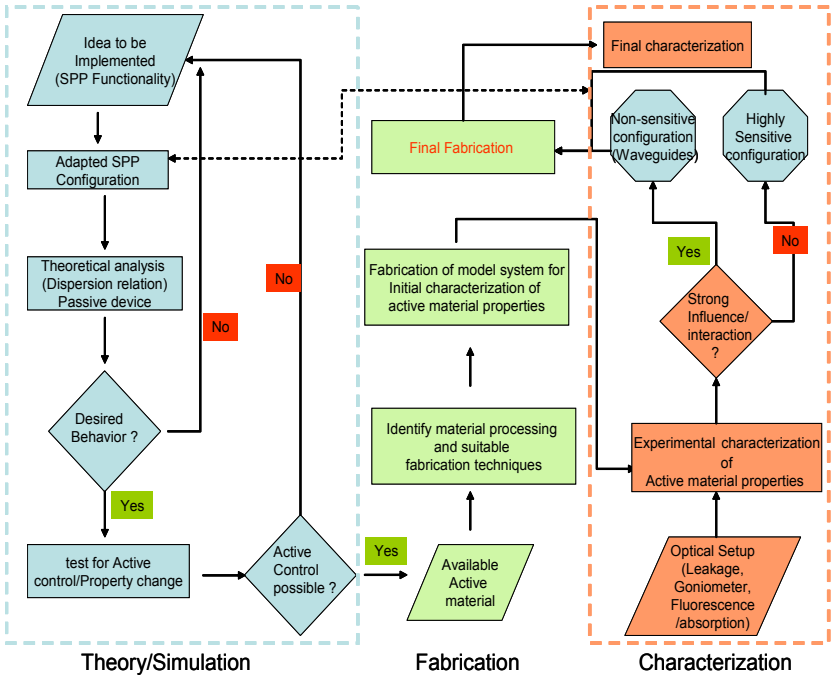

Figure 2.6: *Flowchart describing the processes involved during various stages of development of active SP functionality*

configuration is chosen based on theoretical predictions. With the help of simulation tools, the dispersion characteristics of the given configuration are calculated in order to assess the modes supported by the structure. Using this information optical properties of the desired configuration are estimated and verified experimentally. Once these are confirmed and a reference system is finalized, the next step is to proceed to the active functionality. The change in the surrounding refractive index is simulated in order to estimate the potential control over the plasmonic mode, taking into account realistic index changes for existing active materials. If the given configuration shows promising results, it is worthwhile to start with the initial steps of fabrication. The best methods for processing the given active material are chosen and tested. Fabrication techniques are optimized and improved for good quality production. The next step is the preparation of layers of active materials, to characterize the nonlinear coefficient for the given material, or a corresponding relevant property for the given material. The results can be used to decide whether the type

of configuration is appropriate, depending on how strong is the nonlinear response. In the case of a small nonlinear response ($\leq 10^{-3}$), a highly sensitive configuration is needed, such as ring resonators. However, for bigger changes ($\geq 10^{-2}$), one could use simpler strategies, such as a waveguide configurations. Once this is accomplished, the process for the final fabrication can be followed, and optical characterization can be commenced, for measuring the device specifications.

2.6 Active Plasmonics: Components & Criteria

In order to build a successful hybrid prototype, it is crucial to optimize both the plasmonic geometry and the active media. Apart from an optimized plasmonic geometry, the choice of active media is based on factors such as strong nonlinear response, preferably accompanied by very fast time response of at least $\mathcal{O}$(nano-seconds), and low losses due to absorption and scattering.

For both cases, fabrication compatibility needs to be fulfilled in order to successfully create a resulting hybrid component. Fundamentally, apart from a good spatial overlap, good spectral and temporal overlaps are also necessary in many cases for strong coupling. Figure 2.7 depicts different temporal regimes of plasmonic modes supported by different types of layered structures for two common plasmonic metals, Au and Ag. The data was derived numerically from the dispersion relations which were calculated using a code based on frequency domain method for each of the different geometries. When the temporal responses of the plasmon and an exciton (in an active material) match, it leads to strong interaction between the two, resulting in a tightly coupled mode.

2.6.1 Plasmonic Configuration

The design of the plasmonic system plays a pivotal role in the overall magnitude of the modulation of a given hybrid system. The limitation posed by the active material in terms of small changes in optical constants, due to its inherent properties, can be overcome by choosing an appropriate

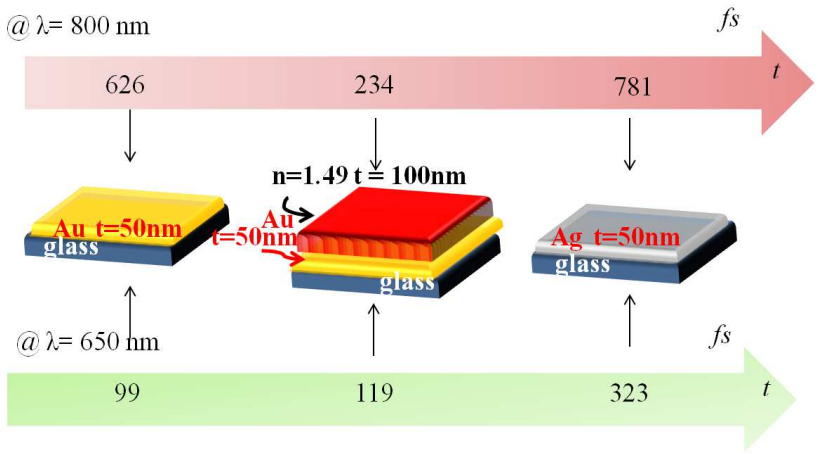

Figure 2.7: *Lifetimes for SPP in different plasmonic configurations at wavelengths $\lambda = 650nm$ and $\lambda = 800nm$. The three different geometries consist of a 50nm Au layer on glass, 100nm dielectric layer on a 50nm Au layer on glass and a 50nm of Ag layer on glass. Ag has shorter lifetimes than Au and for each case the lifetime decreases significantly as the refractive index increases at the interface.*

and well-optimized geometry. The goal in terms of an ideal plasmonic configuration would be a geometry that is able to capture optical energy and generate intense, highly confined electromagnetic fields while overcoming the losses due to radiative coupling and absorption. Also essential is a compact geometry, that enables true nanoscale integration, which is also compatible fabrication-wise. When considering the case of SPPs along planar metal-dielectric interfaces for waveguiding purposes, the design must ensure strong vertical and lateral confinement with sufficiently long propagation lengths. Though SPPs feature a strong inherent confinement in the direction perpendicular to the interface (i.e. vertical) due to the exponential decay of the evanescent fields, confinement in lateral direction is controlled by varying the width of the waveguide, since at unstructured surfaces, there exists no lateral confinement of the SPP modes. This is also important in determining several waveguiding properties, as small mode widths enable large bending angles with acceptable losses.

During the course of this thesis several different configurations were tested and tried. A few of these were shortlisted based on their performance in terms of sensitivity, strong mode confinement, novel design and fabrication compatibility. Two key factors that have influenced the design of the chosen plasmonic configuration are listed and discussed below.

2.6.1.1 Strong Mode Confinement

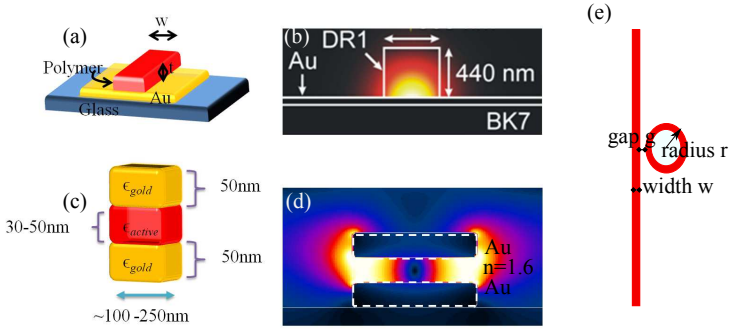

Figure 2.8: *(a)Schematic illustration of a straight dielectric-loaded SPP waveguide (DLSPPW) which consists of a rectangular dielectric ridge of thickness t and width w placed on top of a smooth gold film on a glass substrate; (b)The electromagnetic field distribution in the cross section of a DLSPPW with $h = 440nm$ and $w = 500nm$. (Courtesy: A. Krasavin, King's College); (c)Schematic illustration of a MIM plasmonic nanoparticle in the size range of 100-250nm. The central layer in this geometry consists of an active material (thickness $\approx$ 30-50nm) sandwiched between two metal layers each 50nm thick; (d)The electromagnetic field distribution shows that the mode at the MIM resonance is strongly confined within the active polymer layer. (Courtesy: J.Renger, ICFO); (e)Schematic of a waveguide ring resonator(WRR)*

Surface plasmon modes are by nature vertically confined to the interface at which they are propagating, for applications such as active data processing, it is important to also laterally confine the modes. There are several different methods to achieve this. In the case of SPPs, one such technology that has been developed in recent years is the dielectric loaded SPP waveguide (DLSPPW) configuration, which has proven to be an effi-

cient means of manipulating plasmon signals. This configuration consists of a dielectric ridge placed on a metal surface (as shown in Fig. 2.8(a)), where the lateral SPP mode confinement is achieved due to the fact that the SPP load effective index is larger for the SPP mode supported by the metal interface (even for thin dielectric layers) than for that supported by the metal-air interface. The SPP effective index n_{eff}, is defined as $n_{\text{eff}} = \kappa_{\text{SPP}}/\kappa_0$ where κ_0 is the wavevector of light. The effective index of the SPP plays the role of the refractive index of conventional integrated optics. The strong confinement within the dielectric, as shown in Fig. 2.8(b), renders the plasmonic mode sensitive to refractive index changes in the dielectric load, making it attractive for active control. Moreover, as an added advantage, this technology is easy to fabricate and can be implemented for large scale industrial fabrication.

Another interesting configuration (involving LSPs) is where light is squeezed into the subwavelength volume by designing ultra-compact Metal-Insulator-Metal (MIM) resonators, where it is possible to engineer cavity-like modes of the order of $\lambda/4$ sizes. These nano-resonators support a plasmonic mode which is strongly confined within the dielectric sandwiched between the two metal layers (see Figs. 2.8(c) & (d) showing the MIM configuration and the corresponding field map at a plasmonic resonance for a given system, respectively). Again, this strong confinement could be used for driving various nonlinear processes within the dielectric, if one renders it active by doping or by replacing it with a nonlinear material.

2.6.1.2 Coupled Nanostructures with enhanced Sensitivity

The quality of the plasmonic resonance supported is crucial in terms of its modulation response. The sharper this resonance is, the more favorable it is for tuning purposes when combined with active media. High quality factors increase the prospect of a sensitive overall response for the given configuration.

In order to achieve high quality factors in a hybrid plasmonic system, we chose to work with coupled systems whose output plasmonic response is defined as being a result of the coupling between its individual com-

ponents. In the case of SPP propagation in a DLSPPW geometry, the means of altering the transmission of the SPP through a waveguide is by rendering the transmission resonant due to coupling to an adjacent ring. This is as shown in Fig. 2.8(e) as demonstrated subsequently in Chapters 4 and 5.

Similarly, for localized surface plasmons, bringing two metallic nanoparticles close to each another, so that they interact in the near-field, leads to efficient near-field coupling. This is associated with a spectral shift in the collective plasmon resonance. Near field coupling between the nanoparticles also leads to a highly confined electromagnetic mode in the gap between the particles. This enhanced field can be of several orders of magnitude larger than for a single particle, and can be used for sensing, trapping and nonlinear applications [31]. Coupled plasmonic systems support sharp Fano-type resonances provided the symmetry conditions are satisfied [65] .

2.6.2 Active Materials

Typically, the magnitude of the nonlinearity, as well as the switching speed of a plasmonic modulator, are largely dependent on the physical process responsible for the index change of the active medium. Typically, thermally driven changes are much slower than optically induced electronic transitions or phenomena associated with nonlinear polarization, as shown in Fig. 2.5. Pacifici et al. demonstrated all optical modulatoion based on the interaction between SPPs in a thin layer of CdSe quantum dots (QDs). The switching speed was <40ns, limited by the fast intraband transition in the CdSe quantum dots [14]. Pala et al. showed switching using photochromic molecules, but the switching speed for useful modulation is slow ($\approx$ 10s) [66]. Evans et al. demonstrated an electro-optical cell consisting of gold nanorods covered with Liquid Crystals (LC), where the switching speed is depending on the LC polarization properties [67]. Gosciniak et al. demonstrated a thermo-optic plasmonic modulator where the switching speeds are much slower ($\mathcal{O}$(seconds)) [16].

2.6.2.1 Fundamentals of Nonlinear Optics

Most of the equations and some parts of the discussion in the following text have been reproduced from Boyd et al. [68], a reference which provides an excellent general treatment of nonlinear optics. To understand an optical nonlinearity, it is important to consider how the dipole moment per unit volume, or polarization P of a material system depends on the electric field strength E of the applied optical field. In the case of conventional (i.e. linear) optics, the induced polarization depends linearly upon the electric field strength in a manner that can be described generally as:

$$P = \epsilon_0 \chi^1 E \tag{2.6}$$

where, χ^1 is the linear susceptibility.

An instantaneous response by the material is assumed when writing the above equation as a function of time. However, a causality relation should be applied as the response cannot be instantaneous. Instead, polarization should be expressed through a convolution in the time domain between the susceptibility and the electric field. But in the frequency domain a direct product of χ^1 and E is appropriate.

In nonlinear optics, the optical response can often be described by expressing the polarization P as a power series of the electric field strength E which in the frequency domain would be:

$$P = \epsilon_0[\chi^1 E + \chi^2 E^2 + \chi^3 E^3 + \ldots] \tag{2.7}$$

where, χ^1 is the linear susceptibility, χ^2 and χ^3 are the second and third order susceptibilities, etc.

With the addition of each new term in the polarization, new sets of optical phenomena are introduced. For example, the second-order susceptibility is responsible for second-order effects such as second harmonic generation, sum and difference frequency generation and optical parametric oscillation. Whereas, the third-order susceptibility is responsible for effects such as the third harmonic generation, two-photon absorption, optical Kerr effect, Raman scattering, etc. While all materials exhibit

third-order nonlinear optical effects, only non-centrosymmetric materials are capable of displaying second-order effects.

Typically, the values of nonlinear susceptibilities for many materials are very small, and hence, the nonlinear optical effects are relevant only when the strength of the fields involved approaches that of typical internal electric fields encountered in atoms and molecules, in the range of 10^{10}V/m.

A way of expressing the intensity-dependent refractive index is by the means of the following equation:

$$n = n_0 + n_2 I \tag{2.8}$$

where, I denotes the time averaged intensity of the optical field, given by:

$$I = \frac{n_0 c}{2\pi} |E(\omega)|^2 \tag{2.9}$$

If I is measured in W/cm^2, then n_2 is measured in the units of cm^2/W. Numerically, one can express n_2 as:

$$n_2(\frac{\text{cm}^2}{\text{W}}) = \frac{12/\pi^2}{n_0^2} 10^7 \chi^3(\text{esu}) = \frac{0.0395}{n_0^2} \chi^3(\text{esu}) \tag{2.10}$$

The physical mechanisms responsible for the nonlinear change in the refractive index could be electronic polarization, molecular orientation, electrostriction, saturated atomic absorption, or other effects. For each of these processes, the magnitude and time response of the nonlinearity varies.

Within the framework of the materials explored in this work, it is perhaps noteworthy to mention the electro-optic effects that induce a refractive index change to a given material when a DC or a low frequency electric field is applied. If the refractive index changes linearly with respect to the electric field, the effect is referred to as Pockels electro-optic effect. If the change is quadratic, the effect is called the Kerr electro-optic effect.

The Pockels effect can be described through a second-order nonlinear polarization term, given by:

$$P(\omega) = 2\epsilon_0 \sum \chi^2(\omega = \omega + 0)E(\omega)E(0) \tag{2.11}$$

and is linear with respect to the applied field. Also, this applies to non-centrosymmetric, anisotropic materials alone.

Nonlinear optical materials can often be classified according to their atomic composition into organic and inorganic materials. Typical inorganic materials range from dielectric lithium niobate ($LiNbO_3$) to semiconductor materials, such as gallium arsenide (GaAs). Organic materials can be either crystalline, such as polydiacetylene, or polymeric materials incorporating a variety of organic chromophores, such as DR1, often embedded in a host matrix, such as PMMA. This work is restricted to organic polymers, according to their availability and flexibility of fabrication. To select a suitable polymer, other important criteria, such as the feasibility of the existing fabrication process, low losses due to absorption, high magnitude of the nonlinearity, and high damage threshold were also considered. Also, the timescale of the nonlinear process should be within the limit of the characterization process. Most of these are discussed below in further detail, especially in the context of different active media explored during the course of this research.

2.6.2.2 Fabrication Compatibility

In order to fabricate a hybrid plasmonic device it is important that the active medium is compatible with the existing fabrication techniques for plasmonic devices. For example, in the case of electro-optical (EO) plasmonic devices, the structures of the EO materials were patterned via e-beam lithography; one of the candidate materials chosen was the low glass transition temperature (T_g) chromophores that exhibited high index changes, but were unfortunately too readily dissolved by the developer. Considerable efforts were made to find alternative low T_g EO materials, by testing out various combinations of different chromophores and plasticizers doped into a PMMA matrix. But the lack of success in this respect pointed to the fundamental limitation of a low T_g material.

They are naturally rendered porous when chromophores are doped into the PMMA matrix making it easily dissolvable in the developer MIBK (methyl isobutyl ketone), which has a strong chemical impact on such materials. Therefore, DR1 was chosen as the suitable electro-optic material given its compatibility with the fabrication process, though showing a lower index change. Hence, fabrication compatibility and availability of an active medium cannot be ruled out during the selection of an apt candidate for active plasmonics.

2.6.2.3 Magnitude of Nonlinear Response vs. Time Response

As aforementioned, the timescale of the nonlinear response largely depends on the driving process within the active medium, and Fig. 2.5 depicts different time scales involved for different nonlinear processes. χ_3 processes, which are typically quadratically proportional to the intensity of the light, take place on very fast timescales (usually $\mathcal{O}$(femto-seconds)). Electro-optical responses are expected within a few nano-seconds, whereas the birefringent and thermal responses are much slower ($\mathcal{O}$(milli-seconds), or even seconds).

However, sometimes the temporal response is a trade-off with the magnitude of the nonlinearity. For example, the trans-cis isomerization of azobenzene molecules produces a large refractive index change ($\delta n \approx 10^{-3}$), but the relaxation time ($\mathcal{O}$(seconds)) poses a limitation for designing ultrafast switching components. Similarly, certain EO chromophores that induced big index changes ($\delta n \approx 10^{-3}$) based on birefringence of the molecules, have a slow time response ($\mathcal{O}$(milli-seconds)).

2.6.2.4 Magnitude of Nonlinear Response vs. Absorption

The real and imaginary components of the refractive index are connected (Kramers-Kronig relationship) and changes in one component leads to a subsequent change in the other. Nonlinear refractive index changes associated with the real part are typically exploited in spectral regime where the material is fairly transparent, i.e. regions far from one-photon absorption resonances. This is because large absorption coefficients near

resonance increases losses which are often undesirable. However, even though the change in the index is felt across the entire spectrum, it weakens considerably as one moves farther away from resonance. In contrast, nonlinear absorption phenomena are usually exploited near resonance. For organic materials, the trade-off between optical nonlinearity and optical transparency continues to be a problem. Materials having large d (second order nonlinear coefficient) values (e.g. 50-400pm/V) typically exhibit finite absorption at the second harmonic. Hence, a careful choice of spectral and temporal parameters to enhance the nonlinear effect provided by the active material are necessary for SP modulation, given the inevitable trade-offs one often encounters for different materials.

It is also important to understand "passive" plasmonic configurations since they serve as prototypes for effective integration with active materials in a hybrid functionality. The next chapter discusses in detail the first passive prototypal SP configuration, i.e. the dielectric SPP mirrors.

Chapter 3

Passive I: Dielectric SPP Bragg Mirrors

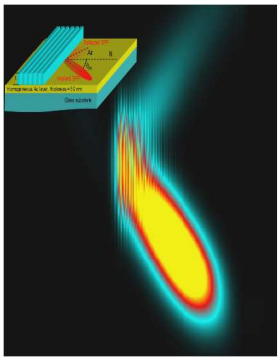

The first passive plasmonic configurations that was studied and analyzed was the dielectric-based SPP mirrors. Not only did this work provided one of the reference configurations for analyzing the active control of SPPs, but it also served as an introduction towards gaining familiarity with the required computational tools, fabrication methods and leakage radiation microscopy, for the characterization of SPP devices.

In this chapter, the ability of gratings made of dielectric ridges, placed on top of flat metal layers, to open gaps in the dispersion relation of SPPs was studied, both experimentally and theoretically. The possibility of using dielectric gratings on top of a continuous Au-film as Bragg mirrors for SPPs was analyzed as an analogy to the conventional dielectric Bragg mirrors used in classical optics. The chapter is divided in two main sections: in the first part, the propagation of surface plasmons on interfaces consisting of flat metal layers covered with periodically structured

dielectric loads was investigated. The alternation of the effective refractive index opened a gap in the SPP dispersion relation, analogous to the propagation of light in periodically layered dielectrics. The properties of the gaps opened in these systems were studied in detail as functions of different dielectric load parameters, such as height, relative thickness and the angle of SPP propagation. The gaps opened by the periodic dielectric loads were compared with those opened using metallic gratings. The significant differences in the properties of these two kinds of gratings have been addressed, and the underlying mechanisms for opening the gap in each case are discussed. The second section demonstrates the performance of this system as dielectric Bragg mirrors for SPPs, both theoretically and experimentally.

3.1 SPP along periodically structured Interface

As mentioned earlier, SPPs are evanescent waves bounded to the interface of a metal and a dielectric, whose dispersion relation is determined by the dielectric permittivity of the metal and the dielectric constituting that interface, and the interface geometry [6]. In the case of a semi-infinite homogeneous dielectric on top of a semi-infinite homogeneous metal, the SPP dispersion relation is given by Eq. 2.3. For more complex geometries (multilayers, corrugations, etc.), analytical expressions for the dispersion relation are difficult to derive, and numerical calculations are needed. In this work, a Fourier Modal Method (FMM) [69, 70] has been employed to compute the dispersion relations of SPPs propagating on Au surfaces, covered by homogeneous and patterned dielectrics. Specifically, the reflectivity of the dielectric/metal film system was calculated when illuminated with p-polarized light from a glass substrate, as a function of both the angle of incidence and the wavelength. The minima in this reflectivity are associated with the transfer of energy to the SPP mode, and therefore, represent the SPP dispersion relation. This method has been demonstrated to provide good results in Au surfaces decorated with Au ridge gratings or Au plot arrays [47, 49].

Figure 3.1(a) depicts one of these reflectivity maps for a 50nm-thin Au layer on a glass substrate, loaded by a homogeneous dielectric thin film (100nm SiO_2, with a refractive index $n = 1.49$) exposed to air, as sketched

in the inset of the figure. The reflectivity minima curve (in blue) provides the dispersion curve of the SPP mode, which, within the considered wavelength range, is located well to the right of the light line, due to the presence of the thin dielectric film. The SPP dispersion can be expressed in terms of the effective index of the mode, n_{eff}, defined as $n_{\text{eff}} = \kappa_{\text{SPP}}/\kappa_0$. The effective index of the SPP plays the role of the refractive index of conventional radiative optics [35]. Figure 3.1(b) shows the evolution of n_{eff} with the thickness of the dielectric layer, t, for a fixed wavelength ($\lambda_0 = 800$nm, where λ_0 is the wavelength in vacuum). As expected, n_{eff} increases with the thickness t, and it reaches a saturation around 350nm, which is related to the exponential decay of the SPP electric field within the dielectric medium.

When SPPs travel through a vertical boundary between two dielectrics of different thicknesses, n_{eff} will be discontinuous, and the SPPs will experience Fresnel refraction and reflection [52]. In the same way, when SPPs propagate through a periodic stack of interfaces with different n_{eff}, the reflection from the subsequent boundaries will interfere, and may give rise to constructive interference of the reflected waves, which opens a gap in the SPP dispersion relation. Such a stack of interfaces with different n_{eff}-s can be achieved by alternating dielectric ridges of different thicknesses on top of the metal surface, or, by arranging ridges of height h, spaced by air ($h = 0$nm), as depicted in Fig. 3.1(d). As an example, Fig. 3.1(c) shows the SPP dispersion curve for ridges of SiO_2 with $h = 100$nm on top of a 50nm Au film. The SPP travels in the direction perpendicular to the grating ($\phi_{\text{inc}} = 0°$). The condition for constructive interference, or, equivalently, for opening the gap is:

$$\kappa^1_{\text{SPP}} d_1 + \kappa^2_{\text{SPP}} d_2 = \pi \tag{3.1}$$

which can be expressed in terms of the effective refractive index:

$$n^1_{\text{eff}} d_1 + n^2_{\text{eff}} d_2 = \lambda_0/2 \tag{3.2}$$

where, d_1 and d_2 correspond to the widths of different dielectric ridges (see Fig. 3.1(d)). The widths d_1 and d_2 of the stack shown in Fig. 3.1(c) are calculated after Eq. 3.2, for providing a gap in the dispersion relation at $\lambda_0 = 800$nm; $d_1 = 150$nm, $d_2 = 205$nm ($n^1_{\text{eff}} = 1.27, n^2_{\text{eff}} = 1.02$). As

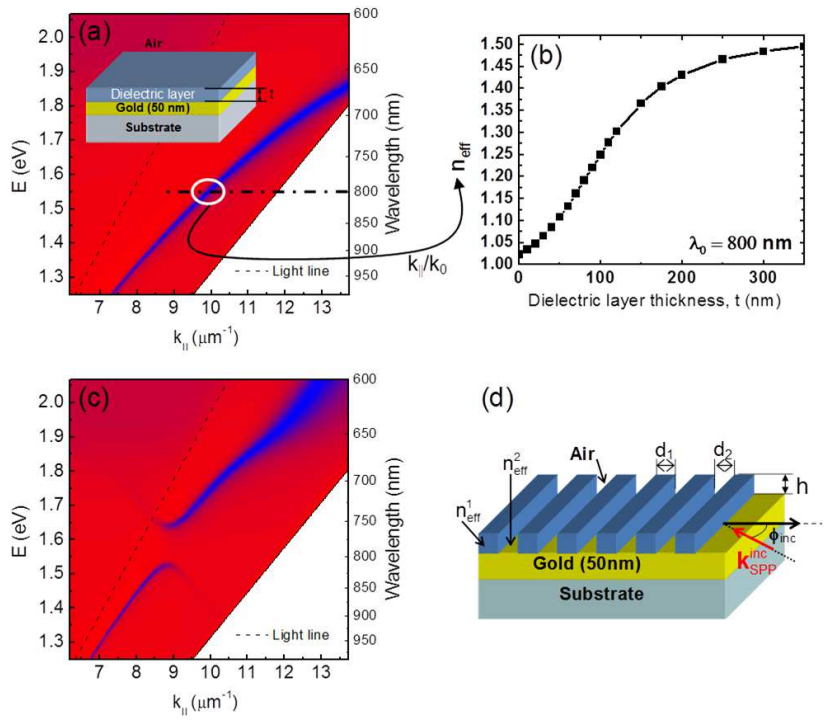

Figure 3.1: *(a)Reflectivity map for a layered system consisting of a 50nm-thick Au film covered by a 100nm-thick dielectric (n =1.49) film as shown in the inset. The SPP dispersion curve is clearly visible in blue; (b)Effective index, n_{eff}, of SPPs propagating on a 50nm-thick Au film covered by a dielectric layer of thickness t for $\lambda_0 = 800nm$; (c)Reflectivity map of a 50nm thick Au surface covered by a structured dielectric layer for wave incident perpendicular to the grating lines. The dielectric layer consists of a grating of ridges of height $h = 100nm$ and width $d_1 = 150nm$ separated by air ($d_2 = 205nm$) as shown in (d). In this sketch, $\kappa_{\text{SPP}}^{\text{inc}}$ corresponds to the SPP wave vector incident on the grating, and ϕ_{inc} represents the angle of incidence.*

can be seen in Fig. 3.1(c), the dispersion relation presents a gap centered at $\lambda_0 = 785$nm, which is in good agreement with the expected value. This result implies that Eq. 3.2, although not exact, provides a good approximation for the design of dielectric SPP Bragg mirrors, at least at normal incidence. For the design of dielectric SPP Bragg mirrors for

other incidences, the in-plane wave vector component perpendicular to the grating alone has to be taken into account in Eq. 3.1. This leads to the following general expression for any incident angle ϕ_{inc}:

$$n^1_{\text{eff}} d_1 \cos\phi_1 + n^2_{\text{eff}} d_2 \cos\phi_2 = \lambda_0/2 \tag{3.3}$$

where the angles ϕ_{inc}, ϕ_1 and ϕ_2 are related by Snell's law ($n^{\text{inc}}_{\text{eff}} \sin\phi_{\text{inc}} = n^1_{\text{eff}} \sin\phi_1 = n^2_{\text{eff}} \sin\phi_2$). Throughout this paper, it is assumed that $n^{\text{inc}}_{\text{eff}} = n^2_{\text{eff}}$ and $\phi_{\text{inc}} = \phi_2$.

The SPP dispersion relation was then computed for gratings with $h =$ 100nm, for different angles ϕ_{inc} and parameters d_1 and d_2 calculated from Eq. 3.3, to provide a gap centered at $\lambda_0 = 800$nm. The results are shown in Table 3.1, where the intended gap center position is compared with that obtained from the dispersion relations. According to the results, Eq. 3.3 predicts the gap position for small angles of incidence quite accurately, but the deviation becomes more significant as ϕ_{inc} increases, being as strong as 100nm for $\phi_{\text{inc}} = 60°$. This deviation can be attributed to the estimation of the effective index of the dielectric ridges. An isotropic n_{eff} value was used, obtained from continuous dielectric layers of the same height ($n_{\text{eff}} = 1.27$ in this case). However, one can expect that n_{eff} is anisotropic, as is the structure itself. This value makes sense only when SPPs propagate perpendicular to the ridge. SPPs travelling along the ridge, on the other hand, will be guided inside the ridge, and experience a $n_{\text{eff}} = 1.06$ of this guided mode is approximately 1.06, for the particular ridge dimensions here [56]. Therefore, the n_{eff} for SPPs going through the ridges at angles other than 0° or 90° would be in between these two extreme values, moving towards smaller values as the angle of propagation increases. The actual gap position should then move towards smaller wavelengths, as ϕ_{inc} increases, as can be seen in Table 1. A accurate determination of the ridges n_{eff} for the different angles of propagation would improve the validity of Eq. 3.3.

3.1.1 Gap Properties for different Grating Parameters

After gaining some insight into the design of the dielectric gratings, now the dependence of the gap position and width is analyzed on the grating

ϕ_{inc} Degrees	d_1 (nm)	d_2 (nm)	Intended GC eV (nm)	Obtained GC eV (nm)
0	150	205	1.55 (800)	1.58 (785)
30	169	231	1.55 (800)	1.61 (772)
45	197	269	1.55 (800)	1.66 (747)
60	248	340	1.55 (800)	1.78 (698)

Table 3.1: *Comparison between the intended gap center (GC) position as calculated by Eq. 3.3 and the actual gap center (GC) position obtained from the computed dispersion relation*

parameters: filling factor, height of the dielectric ridges and the angle of incidence. The grating filling factor, FF, is defined as the ratio of the surface occupied by the dielectric ridge to the length of the unit cell or periodicity $d = d_1 + d_2 : FF = d_1/d$. Figure 3.2(a) shows how the gap width evolves as the filling factor varies from 0.1 to 0.9, for a grating of 50nm-high SiO_2 ridges with d = 355nm (d1 then varies from 35 to 320nm). The SPP propagates perpendicularly to the grating ($\phi_{inc} = 0°$). These results show that the maximum gap width is obtained when the filling factor is around 0.50. In fact, for both very small and very high FFs, the perturbation of the grating is so small that the open gap is very narrow. The grating effect is stronger for FF around 0.50, providing a bigger gap width around these values. Moreover, for traditional Bragg mirrors, it is known that the optimum ratio between the thicknesses of the composing layers corresponds to the lambda/4 condition (where lambda refers to λ in the media). In the case of dielectric SPP Bragg mirrors, the most favorable FF obtained is 0.42. Taking into account that n^1_{eff} is higher than n^2_{eff}, this indicates that the $\lambda/4$ condition, although not exact, can be considered as a good condition for the design of these mirrors. Interestingly, the gap width is higher for FF = 0.1, than for FF = 0.9, where the gap disappears. This reveals that very narrow dielectric stripes on top of the Au surface are more efficient as Bragg mirrors than a dielectric layer engraved with very narrow air grooves.

In Fig. 3.2(b), the evolution of the gap position as a function of FF is shown. The graph shows that the gap center is red shifted almost linearly as the filling factor increases. This result is in good agreement with Eq.

3.3. For a fixed period, an increase in FF increases d_1 and decreases d_2. This implies that the SPP travels longer through a medium with a higher n_{eff}. Therefore, the dispersion relation of the SPP propagating through the grating shifts towards higher in-plane wave vectors, as FF increases. As the first Brillouin zone boundary is fixed for a given period, the gap position moves towards lower energies. Regarding the gap edges, they are accordingly red shifted as FF increases. Figure 3.2(c) accounts for the evolution of the gap width as the height of the grating, h, is varied from 10nm to 250nm, assuming a grating period and width of 355nm and 150nm, respectively. From the results plotted, it can be observed that the gap width increases monotonically with h. Besides, the gap width reaches values as large as 125nm for $h = 250$nm. Since the increase in h implies an increase in n^1_{eff}, the index contrast of the media composing the Bragg grating raises, and as a consequence, the gap width is enlarged. In Fig. 3.2(d), the dependence of the gap center and edges position on the grating height is plotted. The center wavelength increases linearly with h, until the height is about 120nm. Thereafter, the increase is slower towards an asymptote. The upper and lower edges follow the same evolution. The red shift of the gap center can be understood from Eq. 3.3 as h increases, so does n^1_{eff}, and therefore $\lambda_0/2$ increases. Since n_{eff} reaches a saturation value as h increases (see Fig. 3.2(b)), related to the exponential decay of the SPP electric in the dielectric, the same behavior is seen for the gap center wavelength.

Figures 3.2(e) and 3.2(f) show the evolution of the gap width with the angle of incidence, for gratings of height $h = 100$nm and FF $= 0.42$. In Fig. 3.2(e), the periodicity d, calculated from Eq. 3.3, is used to obtain a gap centered at $\lambda_0 = 800$nm. It is known that the actual gap position deviates strongly for this wavelength, for large angles of incidence. So, in order to prevent conclusions associated with the variation of the gap center position, for Fig. 3.2(f), the periods are corrected accordingly so that the center wavelength is the same for all angles of incidence. It can be seen that these variations do not considerably affect the gap width, which remains around 65nm. The main parameters governing the gap width are FF and the height of the ridges, which determine the optical contrast along the grating. There is, however, a weak tendency of increasing the gap width with ϕ_{inc}, similar to the occurrence in classical optics dielectric Bragg mirrors.

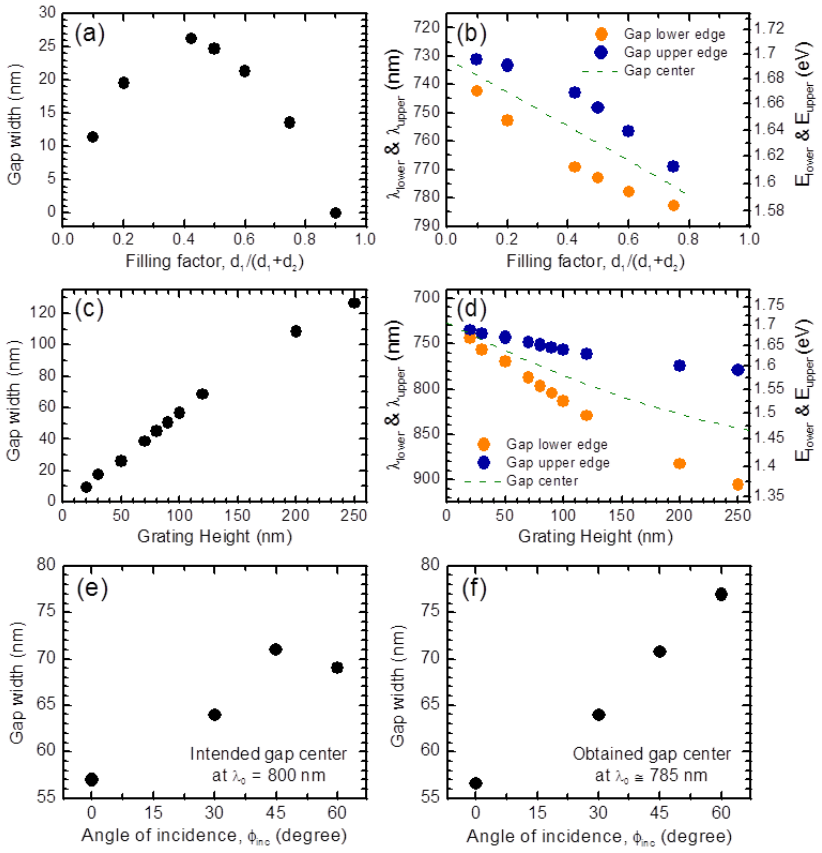

Figure 3.2: *(a)Gap width evolution with the filling factor for dielectric gratings of $h = 50nm$ and $d = 355nm$; (b)Gap position with respect to filling factor for the same system; (c)Gap width versus grating height for a system with $d = 355nm$ and optimum filling factor (FF=0.42); (d)Gap position with respect to height for the same system; (e)Gap width versus the angle of incidence for gratings of $h = 100nm$ and d calculated from Eq. 3.4 to obtain a gap at $\lambda_0 = 800nm$; (f)Gap width versus angle of incidence for gratings with gaps centered at $\lambda_0 = 785nm$*

3.1.2 Comparison with Gaps opened in Metallic Corrugated Layers

As already mentioned, the properties of SPP Bragg mirrors based on metallic gratings have been analyzed extensively, both theoretically and experimentally [45–47]. In this subsection, the behavior of the dielectric and metallic gratings is compared, in order to gain an insight into their differences and similarities. In particular, the dependence of the gap properties on the grating filling factor, and on the angle of incidence is presented.

Figures 3.3(a) and 3.3(b) show the gap width and the gap position evolution with the mirror filling factor, respectively, for a grating consisting of 50nm-high Au stripes on a 50nm-thick Au film. The grating periodicity is $d = d_1 + d_2 = 355$nm. The design of the metallic SPP Bragg mirrors is based on the purely geometrical Bragg relationship [46]:

$$d = \frac{\lambda_0}{2n_{\text{eff}} \cos \phi_{\text{inc}}} \tag{3.4}$$

since, in this case, $n^1_{\text{eff}} = n^2_{\text{eff}}$. Thus, the metallic Bragg mirror with, $d = 355$nm, is designed for showing a gap centered at $\lambda_0 = 724$nm, at normal incidence. The results plotted in Figs. 3.3(a) and 3.3(b) point out several differences between metallic and dielectric based SPP Bragg mirrors. First, the gap width is much larger for metallic mirrors: it can achieve 130nm for a 50nm-high Au grating, while the maximum value obtained for a 50nm-high SiO_2 grating is only 26nm. This was attributed to the higher scattering power of the Au grating. Nevertheless, a gap width of 125nm can also be attained with dielectric mirrors by using 250nm-high dielectric stripes. Moreover, with the propagation of the SPP through the dielectric ridges being much smoother, one expects smaller losses associated with the dielectric gratings. Regarding the evolution of the gap width with the grating filling factor, the behavior is similar for both kinds of gratings, showing the maximum gap width for filling factors around 0.50. Indeed, the maximum gap width occurs exactly at FF = 0.5 for the metallic grating, in perfect agreement with the "$\lambda/4$" condition (since here $n^1_{\text{eff}} = n^2_{\text{eff}}$).

As for the gap center position, the behavior of the two kinds of grat-

ings is completely different. For the dielectric gratings [Fig. 3.2(b)], the evolution of the gap center is monotonic with FF, and the gap edges movement compensates for the gap width evolution. This is not the case for metallic gratings. From Eq. 3.4, the gap center should not change with FF. However, it decreases slightly as FF increases. On the top, the gap edges evolution is quite asymmetric. The lower gap edge moves with the filling factor, as expected, favoring a larger gap width at FF around 0.5. The upper gap edge, on the other hand, moves very little. In fact, this can be explained in terms of the SPP dispersion relation [41]. The SPP Au/air dispersion relation lies very close to the light line, and the movement of the upper edge is highly limited, lest the mode should turn into a radiative one [see Fig. 3.3(c)]. The lower edge, in contrast, is free to move as much as the grating parameters determine. Since this effect is more significant in the conditions providing a bigger gap width, such as FF <0.6, the gap center position is shifted towards longer wavelengths, as can be seen in Fig. 3.3(b). As a consequence, the gap center position is higher than the design value $\lambda_0 = 724$nm; the limited opening of the upper gap edge artificially shifts the gap center to a lower energy. In the case of dielectric mirrors, the limitation of the movement of the gap upper edge is less strict. This is attributed to the fact that the SPP dispersion relation is shifted towards larger in-plane wave vector values (away from the light line), due to the presence of the dielectric load [see Fig. 3.1(c)].

Figures 3.3(d) and 3.3(e) show the evolution of the gap width and the position with the angle of incidence. The grating height was $h = 50$nm for all the cases, and the grating period was calculated using Eq. 3.4, to get a gap centered at $\lambda_0 = 724$nm in each case. A strong reduction in the gap widths with ϕ_{inc}, in this case [see Fig. 3.3(e)], was observed. This behavior was already been predicted in metallic gratings [71, 72]. This was attributed to a reduction in the scattering power of the metallic defects (ridges) with the angle of incidence [72]. The dielectric gratings, on the other hand, show a much smaller dependence of the gap width on ϕ_{inc}. Therefore, when considering gratings for the design of SPP Bragg mirrors, the dielectric based design is more consistent for different angles of incidence, while the properties of the metallic ones are strongly affected by the angular change, making the first system more flexible.

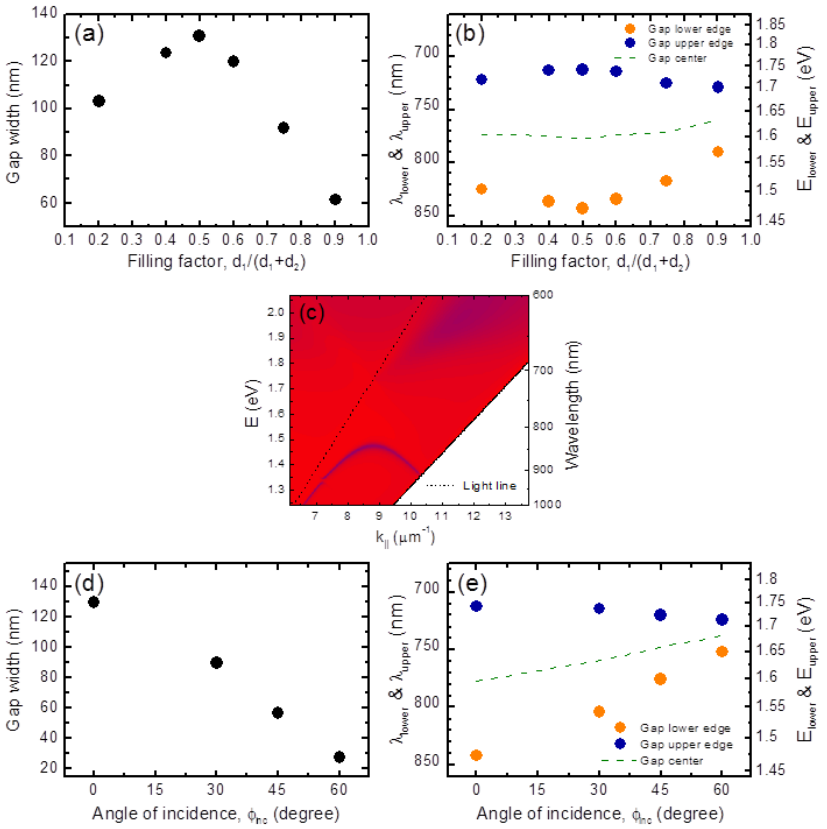

Figure 3.3: *(a)Gap width evolution with the filling factor (FF) for metallic gratings with $h = 50nm$, $d = 355nm$ and $\phi_{\text{inc}} = 0°$; (b)Gap position with respect to filling factor for the same system; (c)Dispersion relation for a metallic grating with $h = 50nm$, $d = 355nm$ and FF=0.50; (d)Gap width versus the angle of incidence for metallic gratings with $h = 50nm$ and d calculated according to Eq. 3.4 for providing a gap centered at $\lambda_0 = 724nm$; (e)Gap position with respect to angle of incidence for the same system as (d)*

Back again with the metallic gratings, the gap center position [Fig. 3.3(e)] moves closer to the nominal value for bigger angles of incidence as a consequence of the asymmetry in the gap edges movement. The upper gap edge remains almost insensitive to the angle of incidence, all the influence of the reduction in scattering power being taken by the lower

gap edge.

3.1.3 Experimental Observation of SPP Band-Gaps in Dielectric Gratings

After presenting the theoretical basics for the design of dielectric SPP mirrors, the creation of a gap is experimentally proven using leakage radiation microscopy (LRM). LRM is a far-field technique designed to recover the radiation leaking towards the substrate, while the SPP propagates on a thin metal film deposited on glass [35, 73–75]. This technique gives images whose intensities are proportional to that of the propagating SPP, and has already been demonstrated to provide quantitative information on SPP devices, such as mirrors [47, 76] and waveguides [56]. With an appropriate lens configuration, the leakage radiation microscope can capture not only the real plane, but also the conjugated (Fourier) plane [74, 75], which allows a direct observation of the κ-space. For a fixed wavelength, this provides images of the two-dimensional iso-frequency SPP dispersion relation, and hence it discloses the gap [47, 77].

In the experiment, the Fourier plane for surface plasmons propagating on Au surfaces, decorated with several dielectric gratings of different periods and widths, was imaged. The gratings on the measured sample are 95nm-high PMMA ridges, deposited on top of a 60nm thick Au film. The gratings have been fabricated by electron-beam lithography, on top of a Au film, deposited by thermal evaporation. The gratings parameters have been designed to open gaps for SPPs of λ_0 around 800nm at 0°, and 45° with respect to the grating normal (d = 360nm and 466nm, respectively). The chosen filling factor is FF=0.42, the most optimized value in order to obtain the widest gap width as has been shown in the Section 3.1.1.

Figures 3.4(a) and 3.4(b) show the obtained images corresponding to a SPP of energy 1.6eV (λ_0 = 775nm), propagating on the gratings with periodicities of 360nm and 466nm, respectively. The SPPs are launched by focusing a circularly polarized Ti:sapphire laser on top of the dielectric grating. The presence of defects on the Au surface provides the needed momentum to excite the SPP [47]. For a Au thin film having small

defects, the Fourier image would show a circle whose radius is the SPP in-plane wave vector, κ_{SPP}. The presence of the dielectric grating opens a gap in the dispersion relation, as can be seen in the images. This gap appears at around 0° for Fig. 3.4(a), and 45° for Fig. 3.3(b), as expected. By using the FMM method, the isofrequency SPP dispersion relations of the dielectric gratings have also been calculated, for comparison with the experimental images. A good agreement is found with the calculated maps in Figures 3.4(c) and (d) and the measured ones in Figs. 3.4(a) and (b). In order to get the best match in the angular position of the gap for a given SPP energy, $n_{PMMA} = 1.47$ is set, which conforms well with the optical properties of this resist.

Regarding the gap angular width, in the first case, an experimental width of $\Delta\alpha = 32°$ and a predicted value $\Delta\alpha = 42°$ were obtained, and in the second case, $\Delta\alpha = 6°$ for both situations. This angular gap provides information on the angular acceptance of these systems, when used as SPP Bragg mirrors [47]. The angular acceptance decreases as the angle of incidence increases. The good agreement between the experimental Fourier images and the simulated ones indicates excellent suitability of FMM to characterize these gratings.

3.2 Design and Characterization of Dielectric SPP Bragg Mirrors

In the previous section, the band gap of dielectric grating on a metal were studied and demonstrated. In this section the idea is extended by assuming a finite grating of dielectric ridges on a metallic surface, to create an effective mirror for propagating SPPs. The Fourier Modal Method (FMM) was used to compute the reflectivity of different Bragg mirrors composed of SiO_2 ridges, and designed for $\phi_{inc} = 45°$ ($h = 100$nm, $d1 = 200$nm, $d = 466$nm). The calculated gap of this dielectric grating is centered at $\lambda_0 = 750$nm, and the gap width is 65nm.

Figure 3.5(a) depicts the schematic of the calculated configuration, and Fig. 3.5(b) presents the electric field map distribution of the SPP impinging on a Bragg mirror made of 10 ridges. The SPP energy corresponds

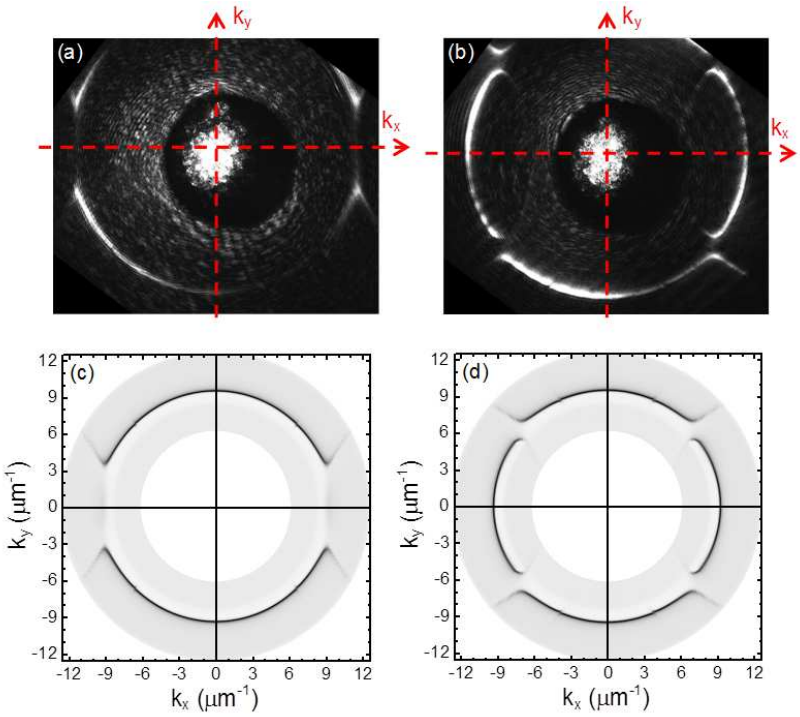

Figure 3.4: *(a)Experimental leakage radiation microscopy (LRM) image of the Fourier plane of a SPP ($\lambda_0 = 775nm$) propagating on a Au surface decorated with a dielectric grating consisting of PMMA ridges of $h = 95nm$, $d = 360nm$ and FF=0.42; (b)Same as in (a) but for a grating with $d = 466nm$; (c)Calculated iso-frequency map at $\lambda_0 = 775nm$ for a SPP traveling on a Au surface decorated with a dielectric grating ($n = 1.47$, $h = 95nm$, $d = 360nm$ and FF=0.42); (d)Same as (c), but for the grating with $d = 466nm$*

to $\lambda_0 = 765$nm, well inside the gap of this grating. As can be seen in the image, after reaching the mirror, the SPP is reflected at $2 \times 45°$. The mirror reflectivity, as calculated from the field map following the procedure described in [46], is $R = 72\% \pm 2\%$. It should be noted here the reflectance calculation takes into account the intrinsic SPP propagation losses, since it is based on the ratio of the SPP intensity after a certain propagation distance, with and without mirror. The transmittance of the mirror is zero, as can be seen in Fig. 3.5(b), from the absence of any in-

tensity on the other side of the mirror. The mirror introduces then a 26% loss, which could be due to absorption when traveling through the mirror, or due to the scattering losses due to radiation in air or in the glass substrate. Figure 3.5(c) shows the evolution of the calculated reflectance, transmittance and losses, with the number of dielectric ridges. All the curves show saturation when the number of dielectric ridges approaches 20.

At this point, it is important to note that even if the gap width opened by metallic gratings is much higher than the one for dielectric gratings of comparable heights, as has been shown in the previous section, the efficiency of the system as SPP Bragg mirrors is not that better. From the results shown in Ref. [46], the calculated reflectivity for a mirror composed of 20 Au ridges at $t = 50$nm is $R = 70\%$. The reflectance obtained by 20 SiO_2 ridges is found to be higher [$R = 76\%$, see Fig. 3.5(c)]. This reduced efficiency of metallic gratings is attributed to the higher losses. For dielectric gratings, lesser scattering is expected, as the losses are attributed mainly to the smaller propagation distance of the SPP through a dielectric load, than through air, implying then that losses are higher where transmission is higher. In this way, the losses decrease with the number of lines for dielectric mirrors unlike metallic ones, for which the losses increase as the number of scattering centers increases.

Finally, to confirm that the effect of the Bragg mirror is due to the gap opening, Fig. 3.5(d) shows the electric field map for a SPP of $\lambda_0 = 800$nm, hitting a mirror designed for a different wavelength ($h = 50$nm, $d = 416$nm; $d_1 = 150$nm, calculated gap centered on 586nm). Out from the gap in this case, the SPP travels through the mirror with a transmittance of 71% and a very small portion being reflected ($R = 1\%$). The load leads to stronger, larger field penetration within the metal and thus larger absorption. This means reduced propagation distance of the SPP on a dielectric load.

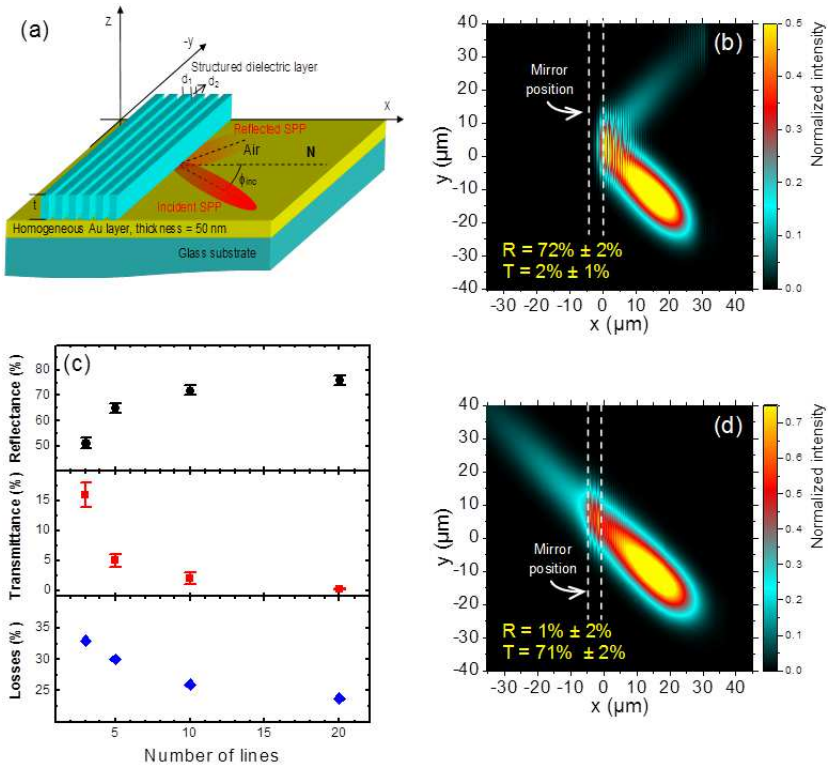

Figure 3.5: *(a)Sketch of the geometry used for the calculation of the reflectivity of a dielectric based SPP Bragg mirror; (b)Electric field map distribution of a SPP ($\lambda_0 = 765nm$) propagating on a 50nm thick Au film and impinging on a grating composed of 10 SiO_2 ridges ($h = 100nm$, $d_1 = 200nm$ and d=466nm); (c)Evolution of reflectance, transmittance and losses with respect to number of lines composing the mirror ($h = 100nm$, $d_1 = 200nm$ and d=466nm); (d)Electric field map distribution of a SPP ($\lambda_0 = 800nm$) impinging on 10 lines SiO_2 Bragg mirror designed for a different wavelength ($h = 50nm$, $d_1 = 150nm$, d=416nm, gap centered around 586nm)*

3.2.1 Experimental Characterization of Dielectric based SPP Bragg Mirrors

The LRM technique was used to characterize experimentally the performance of the dielectric based SPP Bragg mirrors. For that mirrors

composed of different numbers of dielectric ridges on top of a 60nm thick Au substrate were fabricated. To reduce the fabrication time, a negative resist (SU-8, $n = 1.57$) was used, instead of PMMA. The SU-8 ridges height was fixed at $h = 100$nm. The period of the grating was chosen to be $d = 436$nm, and the width $d_1 = 184$nm (FF $= 0.42$). The nominal gap center associated to these parameters, according to Eq. 3.3, is 775nm; so, the actual gap is expected to be around $\lambda_0 = 725$nm, following Table 3.1. The same geometry, as in Ref. [47], was employed to image the SPPs interacting with the dielectric mirrors. SPP on the Au surface was excited by focusing a linearly polarized laser on top of a 200nm wide line [78], and the SPP travels 25μm until they reach the mirror [see Fig. 3.6(a)].

Figure 3.6(b) shows the direct space leakage radiation image of a SPP impinging on a mirror made of 20 SU-8 ridges. The laser excitation wavelength is $\lambda_0 = 750$ nm. The image shows how most of the SPP is nicely reflected when hitting the mirror and no transmission through it is observed. In the case of Fig. 3.6(b), the objective used to focus the light on the launching line has a numerical aperture, N.A. $= 0.65$, resulting in a broad angular distribution of the excited SPPs. This becomes even more obvious when looking at the conjugated Fourier plane as shown in Fig. 3.6(c). The SPPs excited at the launching line travel in opposite directions, giving rise to the two opposite bright circular segments [74]. The significant spreading of the circular segments reflects the broad angular distribution of the excited SPPs. The bright circle in the center corresponds to the directly transmitted light from the excitation, and the grey band is due to light diffracted in all angles by the excitation line. Once excited, the downwards propagating SPP travels towards the mirror, where it becomes reflected. This generates another circular segment in the Fourier image located at 90° with respect to the incident one. The reduced angular width of the reflected beam indicates that the angular acceptance of the Bragg mirror was smaller than the angular distribution of the incident SPP beam. This large angular spreading of the incident and reflected beams prevents any quantitative analysis of image Fig. 3.6(b). Therefore, the numerical aperture of the focusing objective was reduced and the obtained direct and conjugated space images are shown in Fig. 3.6(d) and (e). Here, the incident and reflected SPPs beams appear much more collimated. The direct transmission of the laser located in the center of the Fourier plane has been blocked by

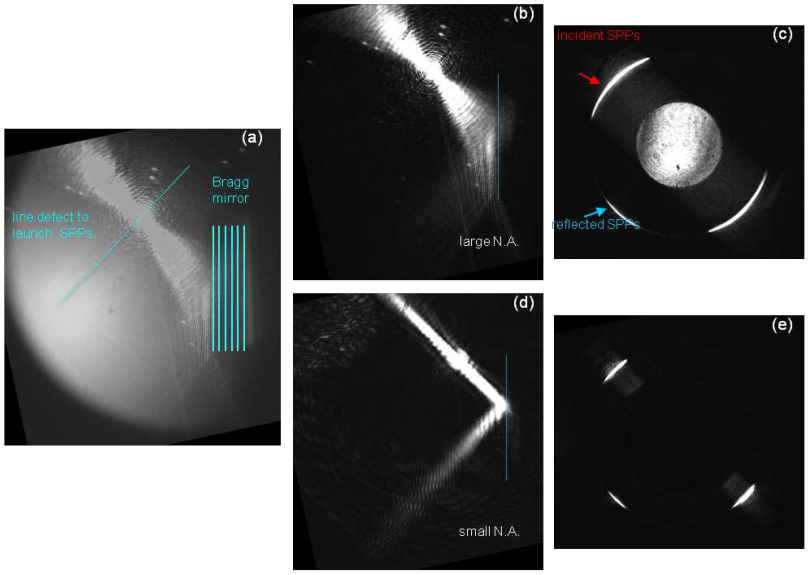

Figure 3.6: *(a) CCD image of leakage radiation by SPPs hitting a dielectric Bragg mirror. The SPPs are excited in two counter-propagating directions by focusing a laser on top of a narrow dielectric ridge, and the mirror is indicated by the lines. The sample is additionally illuminated by a white light lamp to show the excitation line and the mirror position. (b) Direct space leakage radiation (LRM) image for a SPP ($\lambda_0 = 750nm$) impinging at 45° on a dielectric mirror made of 20 ridges of SU-8 ($d = 436nm$). The numerical aperture of the objective that focuses the laser on the launching line to excite the SPP is 0.65. (c) Fourier space image of the same mirror as in (b). (d) Same as in (b) but reducing the numerical aperture of the focusing objective. (e) Fourier image corresponding to (d). The direct transmission of the laser has been blocked by a mask.*

a mask to image only the leakage radiation coming from the SPPs. Still some diffraction coming from the launching line and the grating lines is visible, as shows the grey stripe on the Fourier image [Fig. 3.6(e)].

Figure 3.7 shows the profile of the measured leakage intensity along the incident and reflected SPP beams, for the mirror shown in Fig. 3.6(d) (for the location of the intensity profile, see inset in the figure). The SPP intensity decays exponentially, as expected [6]. By fitting the ex-

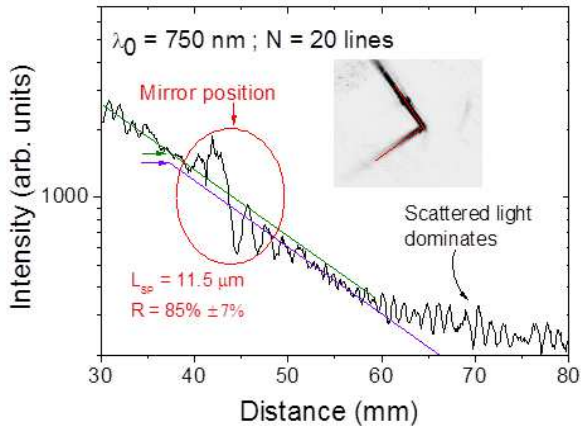

Figure 3.7: *Evolution of the intensity along the incident and reflected beams for a mirror composed of 20 SU-8 ridges (d = 436nm, d_1 = 184nm). The inset shows the corresponding LRM image, and the red line marks the position of the intensity profile.*

perimental data, the SPP propagation distance (L_{SPP}) can be obtained. In this case, one gets $L_{\mathrm{SPP}} = (11.5 \pm 0.6)\mu$m, smaller than the expected value for a film of 60nm Au at $\lambda_0 = 750$nm, L_{SPP} (theoretical) $= 24\mu$m. This can be attributed to resist residues remaining on the Au surface after the lithography process, or to thinner than nominal Au layers. The mirror position can be identified by the presence of some small peaks in the intensity. Interestingly, the intensity profile evolution after the mirror shows an interference pattern which indicates that the reflected SPP interacts with the scattered light produced when the incident SPP hits the first line of the grating. It is observed that this scattered light dominates the signal, as the reflected SPP propagates and decays further away from the grating: unlike the SPPs, the light scattered by the dielectric ridges into the substrate does not decay exponentially, and hence contributes stronger at larger distances. Taking into account this effect, the reflectivity of the mirror is calculated by dividing the exponential fit of the intensity profile after the mirror (violet line) by the fit before the mirror (green line): $R = (85 \pm 7)\%$. The large error is mainly caused by the arbitrariness of the chosen position of the fitted curves. Also measurements at $\lambda_0 = 800$nm (close to band edge) were performed. In this

case, L_{SPP} increases to 16μm, as expected for longer wavelengths (L_{SPP} (theoretical) = 32μm). Again, the mirrors reflectivity for N = 5 lines is very high and close to 85%. A similar result can be obtained for mirrors designed for other angles of incidence. Thus, it could be concluded that the dielectric Bragg mirrors are indeed very efficient, for reflecting SPPs propagating on planar surfaces, even more efficient than theoretically expected, a result that was also observed with the metallic mirrors [46].

These high values obtained for the reflectivity prompts the question whether all the analyzed intensity was coming from the SPP, or whether some light coming from diffraction on the launching line and on the mirror was interfering with our measurements and artificially increasing the obtained reflectivity. However, as can be seen from the Fourier images in Fig. 6, the effect of the diffracted light is quite strong along the incident beam propagation direction, but it is almost imperceptible in the direction of the reflected beam. Therefore, if important, the effect of the diffracted light would be added to the intensity of the incident SPP, providing a reduced value of reflectivity. Other experimental limitation that can result in an overestimated value of reflectivity is the dynamical range of the CCD camera used for taking the images (12 bits). Due to the strong attenuation of the plasmon propagation, the intensity decreases by 3 orders of magnitude and enters in the background level in around 50-60 m, which is our analysis range. If this was disturbing our results, the LSP values obtained from our exponential fits would also be affected; however we obtain very consistent results when we compare different images and wavelengths.

3.3 Summary

This chapter shows how the concept of dielectric bragg mirrors also applies to the context of propagating SPPs. It has been demonstrated that a grating composed of dielectric ridges on a flat Au layer can be used to control the propagation of SPPs, by opening a gap in its dispersion relation. The position of this gap has been predicted by directly applying the analogy to standard optical Bragg stacks for different angles of incidence. Even though the prediction is quite accurate for normal incidence, there is a deviation of the calculated results from the theory for bigger angles.

The properties of the gap have been analyzed as a function of varying grating parameters. The influence of the dielectric grating height and the filling factors conform well to the analogy with the standard optical system. From the comparison of these gratings with their metallic counterparts, notable differences have been observed, which can be attributed to the different mechanisms responsible for the opening of the gap in each case. The gap is opened, in the case of dielectric mirrors, by the contrast in effective index of the SPP, whereas the phenomena mostly responsible for gap opening in metallic mirrors is the strong scattering power of these gratings. The gap has been experimentally confirmed by leakage radiation microscopy in Fourier plane, and a good agreement has been obtained between experiments and simulations.

A step further was taken and the idea extended to using a grating of dielectric ridges as mirrors for propagating SPPs. The properties of these SPP Bragg mirrors have been analyzed both experimental and theoretically. The results show very good reflecting properties upto 85%.

Chapter 4

Passive II: Dielectric-loaded Plasmonic Resonators

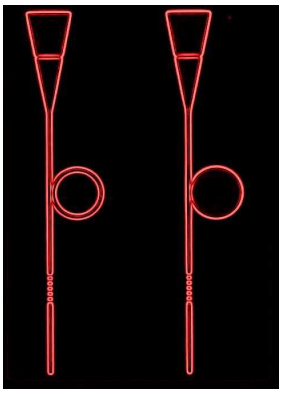

Dielectric resonators which are coupled to optical waveguides have been an important area of research and development since many years now. An extension of this concept applied to the dielectric-loaded plasmonic waveguide platform helps towards building efficient wavelength selective plasmonic components. As mentioned previously in Chapter 2, in the recent past in the field of plasmonics, dielectric-loaded SPP waveguides (DLSPPWs) proved to be an efficient means of guiding and manipulating plasmonic signals due to the strong confinement of the plasmonic mode within the dielectric [79]. The realization of single-mode waveguides with sub-wavelength confinement and relatively low propagation loss has been demostrated [75, 80]. In addition compact basic plasmonic components based on DLSPPW technology such as bends, splitters and Mach-Zehnder interferometers have been implemented [38]. DLSPPWs are promising to achieve integrated active plasmonic components for

nanophotonic circuits [60, 80–82]. The strong confinement within the dielectric renders the plasmonic mode sensitive to a change of its refractive index.

If one replaces the dielectric load with an active material, it makes it possible to realize SPP modulation. However, as highlighted in Chapter 2, significant modulation is conditioned by the sensitivity enough to a small change of refractive index. We have explored modified dielectric-loaded geometries formed by disk or a ring disk or a ring coupled to a straight waveguide. The performance of passive dielectric loaded plasmonic WRRs, was demonstrated previously studied by using near-field optical microscopy [62].

In the coming sections, different types of coupled resonator systems were analyzed. The transmission and coupling for a WRR along with effects on the quality factor, (Q), is discussed. Next, detailed experimental analysis for plasmonic WDRs operating at telecom wavelengths was done using near-field optical microscopy. The effect of parameters like ring radius and gap between the waveguide and the ring on the WDR characteristics such as free spectral range (FSR) and modulation depth is presented. This characterization of the samples was performed by Dr. Tobias Holmgaard at Aalborg University, Denmark. The Finite Element Method (FEM) calculations were done in collaboration with Dr. Alexey Krasavin at King's College, London.

4.1 Plasmonic Resonators: Ring-Disk-Racetrack

The systems under study typically consists of a waveguide coupled to a resonator element such as a ring (WRRs). Electromagnetic coupling between the waveguide and the resonator makes the transmission output of the waveguide wavelength dependent. This type of configuration makes an excellent candidate for wavelength selection finding many applications such as optical filtering. The ring could also be replaced by a disk or racetrack, each geometry having its pros and cons. Fig. 4.1 shows optical images of the three different resonators. When compared amongst each other, while the ring resonator shows excellent filtering properties and makes it possible to achieve high Q factors, but it is more challenging to

fabricate compared to a disk. Indeed, WDRs are much easier to fabricate than WRRs as no proximity effect corrections are required for clearing out the center area. Besides, in order to fabricate very homogenous rings, one has to have excellent alignment conditions for the exposure. Finally, the factors such as astigmatism of the writing beam and its spot size do not play a critical role in case of disks. More details with respect to waveguide disk resonators will be discussed in later sections. Besides, the race-track resonator enables the precise control of coupling efficiency by changing the coupling length.

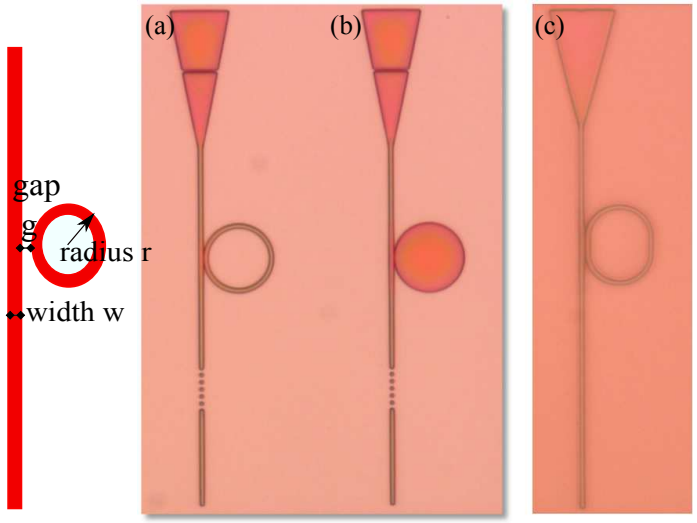

Figure 4.1: *(a) Brightfield microscopy images show fabricated dielectric ring resonator made of DR1:PMMA on top of a (unstructured) planar Au film (gap width = 300 nm, radius = 5.086μm). (b) a disk resonator with same radius as (a). (c) A racetrack resonator made of pure PMMA instead of doped one.*

In the following section we discuss the different parameters impacting the performance of ring resonators. Subsequently, the experimental demonstration of plasmonic disk resonators will be presented.

4.2 Coupling and Transmission through Ring Resonators

In a ring resonator geometry, the transmission of the DLSPPWG is highly wavelength dependent as shown in Fig.4.2(a). In the first approximation, when the optical path around the ring is equal to an integer number of mode wavelengths, the coupling from the waveguide mode to the mode in the ring becomes very efficient, leading to sharp minima in the WRR spectral transmission characteristic as shown in Fig. 4.2(b).

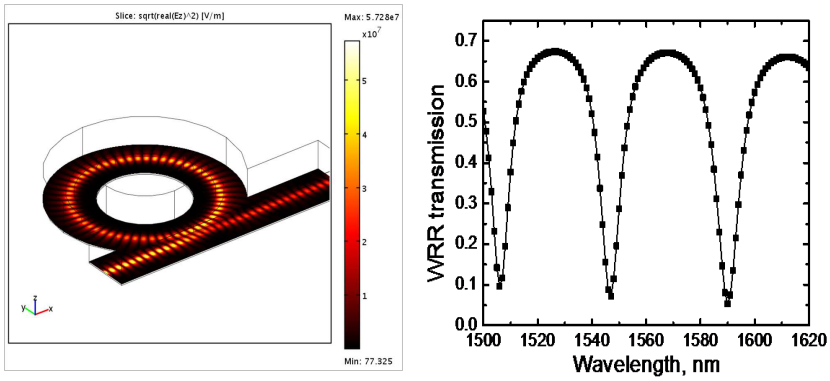

Figure 4.2: *(a) Distribution of the electric field intensity in a DLSPPW-ring resonator coupled to a straight DLSPPW(section* $600 \times 600nm^2$*, gap 250 nm,* $R = 5.486\mu m$ *and wavelength = 1547 nm). (b) Output transmission of the straight waveguide featuring dips due to the coupling to the ring.(Courtesy of A. Krasavin, King's College)*

Several parameters impact the performance of a WRR. The bandwidth or the free spectral range (FSR) of the WRR is determined by the radius of the ring resonator along with the wavelength dependent mode effective index of the bent waveguide, whereas the extinction ratio (ratio between minimum and maximum signal output) is determined by the coupling strength to the ring and the attenuation due to SPP propagation and bend loss around the ring. The gap between the waveguide and the ring plays an important role in the coupling between them. Weak coupling takes place for waveguide-ring gaps $g > 0.5\mu$m due to the very strong mode confinement [80, 83] and short interaction region. A spectral analysis of the WRR with a gap $\approx$ 300nm reveals that the output signal is

strongly modulated with a period that is determined by the radius.

In order to investigate the periodic behavior of the WRR transmission the main system parameters for the transmission throught the WRR under the condition that a single unidirectional mode of the ring resonator is excited and that the coupling is lossless, there is [84]:

$$T = \exp(\frac{-l}{L_{spp}(\lambda)})\frac{\alpha^2 + t^2 - 2\alpha t\cos\theta}{1 + \alpha^2 t^2 - 2\alpha t\cos\theta} \tag{4.1}$$

where the scattering losses at the interaction region have been disregarded. The first factor in the equation represents the propagation loss from cross section A to B given by length l. $\alpha = exp(-2\pi R\beta'')\sigma$ is the inner circulation factor or the field attenuation factor per round trip around the ring of radius R, β'' being the imaginary part of the propagation constant of the DLSPPW mode and σ being a parameter accounting for the pure bend loss. t is the field transmission through the interaction region in the straight waveguide. The phase change around the ring is $\theta = (2\pi/\lambda)n_{\text{eff}}(\lambda)2\pi R$, where λ is the free space excitation wavelength, and R is the ring radius. $L_{spp}(\lambda)$ is the wavelength dependent propagation length and $n_{\text{eff}}(\lambda)$ is the mode effective index.

Most of the interesting features of this resonator occur near resonance (corresponding to a dip) where ($\theta = m2\pi$) (m being an integer). The equation then simplifies to:

$$T = \exp(\frac{-l}{L_{spp}(\lambda)})\frac{(\alpha - t)^2}{(1 - \alpha t)^2} \tag{4.2}$$

It suggests that for $\alpha = t$, i.e. when the internal losses (represented by α) are equal to the coupling losses, the transmission power vanishes or in other words the critical coupling criteria is met due to the perfect destructive interference in the outgoing waveguide between the transmitted field and the internal field coupled into the output waveguide.

A resonator figure of merit, i.e. the Q factor is given by:

$$Q = \frac{\omega}{(\triangle\omega)_{FWHM}} = \frac{2\pi^2 R n_{\text{eff}}}{\lambda(1 - t_{res}^2)} \tag{4.3}$$

where t_{res} is the transmission at the resonance. For high Q resonators, with α near unity, the portion of the curve to the right of the critical coupling point is extremely steep. Small changes in α for a given t , or vice versa, can control the transmitted power between unity and zero. By controlling α and/or t_{res}, a basis for a switching technology is laid. If it happens sufficiently rapid, this can be used as an optical modulator.

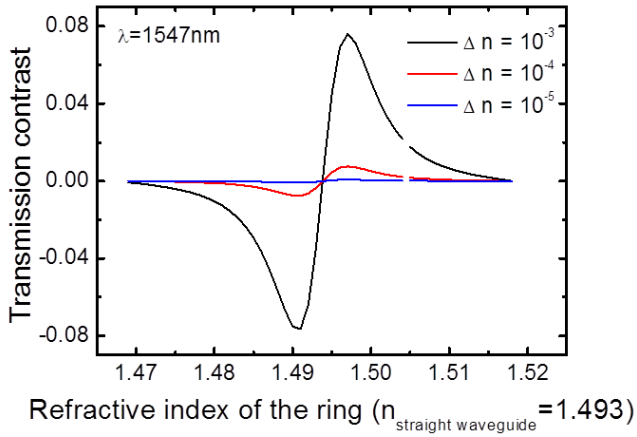

Figure 4.3: *Calculated transmission contrast for* $\Delta n = 10^{-3}, 10^{-4}$ *and* 10^{-5}

Sharp resonances are a very important features for building efficient active functionalities. Beyond sharp resonances, we are interested in maximizing the WRR sensitivity to the change in refractive index Δn of one of the constituting blocks of the coupled system, for e.g. the ring. If the refractive index of the ring material n is changed by an external signal (either optical or electric), the effective index of the ring mode is modified and the resonance is shifted. In Fig. 4.3 the transmission contrast for specific values of $\Delta n = 10^{-3}, 10^{-4}, 10^{-5}$ is derived from DLSPPW transmission data, for a fixed wavelength $\lambda = 1447$nm. In order to get a $\Delta T \approx 8\%$, one needs to induce a refractive index change of $\Delta n = 10^{-3}$.

4.2.1 Fabrication of a DLSPPWG Resonator

Samples containing WRR/WDR structures were fabricated using the following procedure. A 50nm thick Au film was deposited on a glass sub-

strate via thermal evaporation. Then, a 560nm-thick polymer (PMMA) layer was spin-coated onto the Au film. Finally, plasmonic waveguides and ring/disk/racetrack resonators were fabricated by directly patterning the PMMA film with a 30keV electron beam and further chemically developed. Low resolution effects previously observed in small separation regions between straight waveguides and the resonators were successfully overcome by using advanced proximity correction in the design. Figure 4.4 shows a snapshot of a fabricated disk resonators of various disk sizes. Scanning electron microscopy was used to confirm the waveguide width of $\approx$ 500nm and thus ensure single-mode DLSPPW operation.

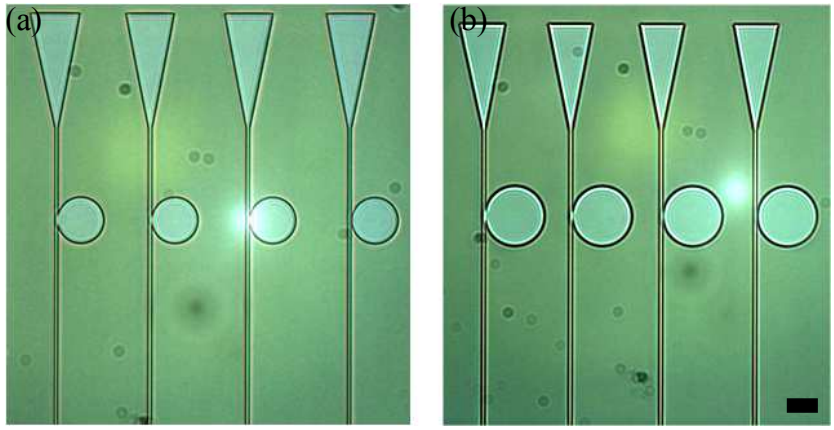

Figure 4.4: *Brightfield images of fabricated disk resonators of different radii (a) 5μm and (b) 7μm. In each image the gap between each disk and waveguide is varied from 300nm (left) to 0nm (right) in steps of 100 nm. Scale bar is 5μm.*

4.3 Optical Characterization of DLSPPW at Telecom Wavelengths

To characterize the fabricated DLSPPW components, a collection mode Scanning Near-field Optical Microscope (SNOM), operating in the telecommunication range was used. As mentioned in previous sections, SPPs are strongly confined to a metal-dielectric interface with exponentially decreasing (evanescent) fields extending only a few hundreds of nanometers

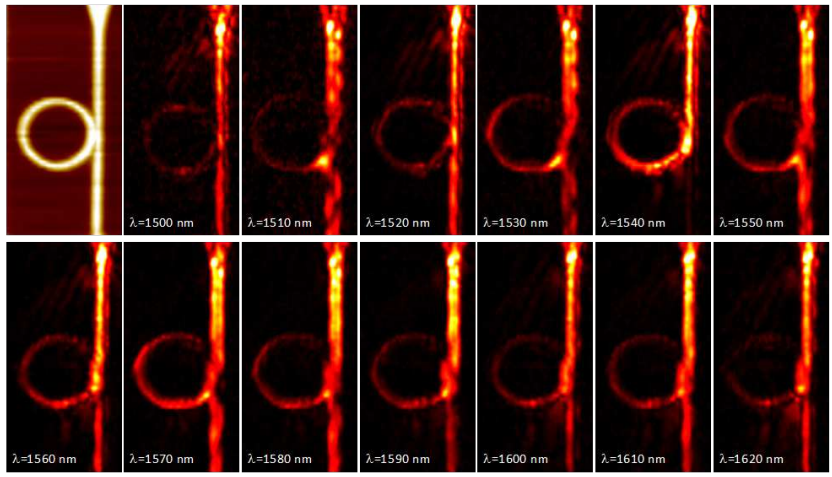

Figure 4.5: *Topography (left) shows the dielectric ring resonator made of DR1:PMMA on top of a (unstructured) planar Au film (gap width = 300 nm, radius* $= 5.086\mu m$*). The optical near-field intensity measured at various* λ *shows a stop-band filter behavior whenever the DLSPPW mode is coupled to the ring, e.g.* $\lambda = 1540nm$ *Courtesy of T. Holmgaard.*

into the dielectric [85], which makes near field investigation with conventional far-field imaging systems impossible. The SNOM operate by controlling the tip-sample distance by measuring the shear force between them and this technique allows simultaneous imaging of a sample topography and the optical near-field.

In the design of the fabricated waveguides a fixed ring radius of $R = 5.48\mu$m was used and the optical near-field intensity measured for different wavelengths. When the coupling condition is met, the mode is strongly confined within the ring, minimizing the waveguide output transmission as can be seen for $\lambda = 1540$nm in Fig. 4.5.

The coupling and transmission analysis for ring resonators can also be extended to understand the behavior for similar resonator shapes especially disk resonators. Although waveguide disk resonators (WDRs) have similar geometries to WRRs, in DLSPPW realization WDRs are easier since the SPP mode can be easily coupled and guided along the rim of the disk. Recent theoretical studies have shown that the WDR design

offers several advantages in terms of smaller radiation losses (or higher quality factors) [86], with WDRs being also easier to fabricate due to less rigid requirements on fabrication tolerances and are more apt candidates for tuning purposes. Numerical simulations on plasmonic disk resonators show that for smaller radii, i.e. $\approx 3.5\mu$m, disks have quality factors double than that of rings since the radiation losses in microdisk resonators in the absence of an inner cylindrical boundary permits the supported mode to reside closer to the resonator center. The supported mode shows stronger confinement due to weaker penetration of field components in the surrounding air [86].

The fabrication and optical characterization of dielectric-loaded plasmonic WDRs operating at telecom wavelengths are presented below. Based on the experimental data, the performance of WDRs is examined with respect to several key parameters, such as the disk radius and separation gap. Experimental data are compared to rigorous 3D numerical simulations.

A SNOM, having an uncoated fiber tip, was used for the characterization of the SPP transmission through the WDRs [83]. To facilitate efficient excitation of the DLSPPW mode, all waveguides were connected to taper structures. The mode at $\lambda = 1540 - 1620$nm was excited inside the taper by matching the excitation angle in the Kretschmann configuration and then was funneled into the waveguide. The first set of structures investigated were WDRs with a radius of 4μm and the separation gap varying from the contact case ($g = 0$nm) to values of 100nm, 200nm and 300nm. Good coupling to the disk was observed for $g = 100$nm, as shown in Fig. 4.6(b) by the optical near-field intensity images acquired at various wavelengths. Whenever the DLSPPW mode was coupled to the disk, a stop-band filter behavior was observed. A plot of the WDR transmission taken at the output waveguide section, normalized to the input, demonstrates a strong decrease in the output signal at the resonant wavelength (Fig. 4.6(d)), which occurs at $\lambda = 1620$nm and 1540nm. In the first approximation, this corresponds to the case when the optical path of the disk mode is equal to an integer number of the mode wavelengths. (Fig. 4.6(c) also shows the numerically calculated field maps $\mid Re(E_z) \mid$ for resonant case ($\lambda = 1550$nm) and a non-resonant case ($\lambda = 1575$ nm), whereby E_z is the main component of the electric field per-

pendicular to the metal surface. In the same time this corresponds to the destructive interference of the waveguide mode propagating through the coupling region and the component of the disk mode coupled back into the waveguide. The jumps in the experimental transmission between the two dips (see Fig. 4.6(d)) are most likely caused by damages to the waveguide during scanning. The experimental results were found out to be in good agreement with numerical prediction (Fig. 4.6(d), red line). Here, the ring radius R, which can be different due to the limited fabrication precision, was used as fitting parameters ($R_{\text{num}} = 4.063\mu\text{m}$). The transmission curve was found to be rather independent on the gap in the range of 100-200nm, so it was kept at 100nm as specified during fabrication.

4.3.1 WDRs - Disk Radius Dependence

One of the main characteristics of WDR performance is the transmission period between two neighboring minima, also called the bandwidth or the free spectral range (FSR) [87]. From the simple WDR transmission model described above it follows that the transmission period is mainly defined by the n_{eff} of the disk mode and the disk radius R. A simple estimation:

$$FSR = \frac{\lambda^2}{(2\pi n_{\text{eff}} R)} \tag{4.4}$$

gives a correct idea about its value observed in the experiment. However, due to the fact that n_{eff} is actually wavelength-dependent and there exists coupling-induced phase shift (CIFS, also wavelength-dependent [88]), more comprehensive theoretical approach is necessary. Full 3D numerical simulations based on the finite element method were employed to study the WDR transmission. In order to study the WDRs performance based on the important design parameters, structures with different disk radii and various gaps sizes were fabricated (Fig. 4.4). The length of the funnel region $L1$ was chosen to be 25μm, whereas $L2$ and $L3$ were 70μm and 50μm, respectively.

The dependence of the transmission period on the disk radius was also studied, while keeping constant the separation gap g at 100nm. As can

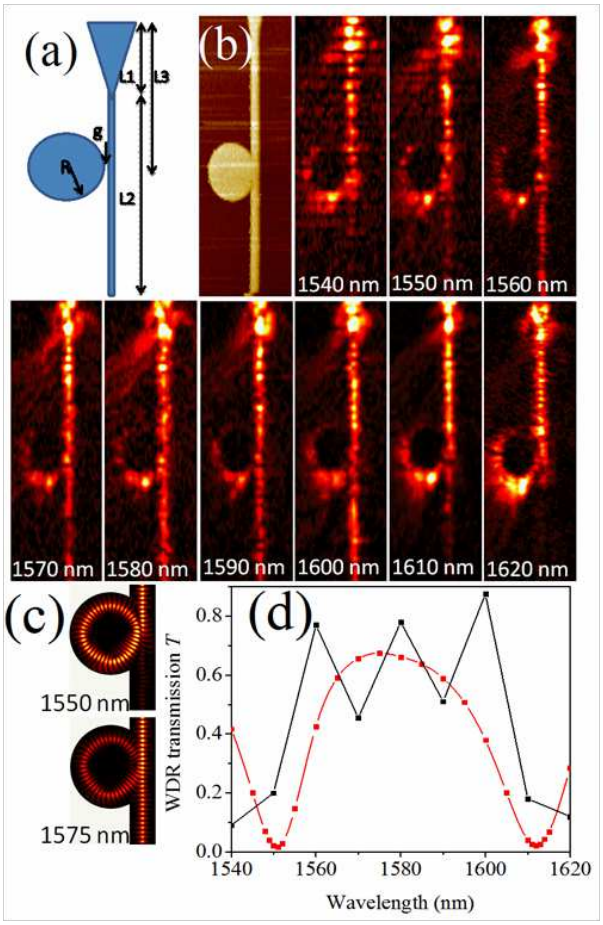

Figure 4.6: *(a) Schematic of the WDR: the dielectric disk resonator made of PMMA on top of a (unstructured) planar Au film (g = 100nm, R = 4μm); (b) Topography and near-field intensity measured with SNOM for different wavelengths in 1540-1620nm range; (c) Numerically calculated field maps | $Re(E_z)$|, (E_z is the main component of the electric field perpendicular to the metal surface) for the same parameters as in (b), for resonant case(λ = 1550nm) and a non-resonant case (λ = 1575nm; (d) Comparison of the WDR transmission measured at the output waveguide section (black) with the numerical modeling (red) for the WDR parameters in (b). Courtesy of T. Holmgaard.*

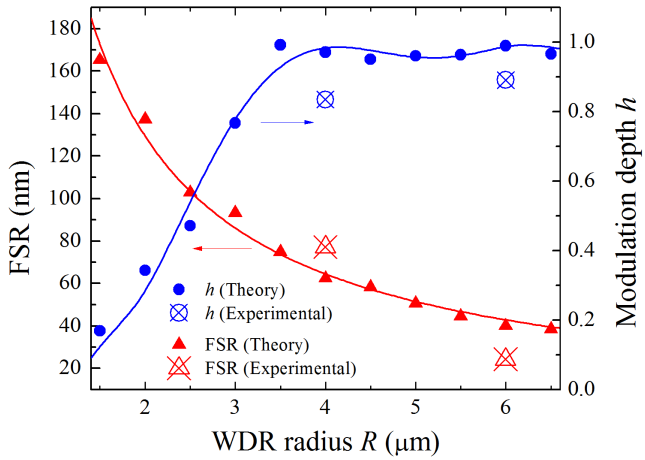

Figure 4.7: *Evolution of the FSR (triangles) and modulation depth h (circles) with the disk radius at a constant gap g=100 nm. The crosses represent the experimental data, solid lines represent numerical results. No fitting parameters were used for numerical modeling.*

be seen from Fig. 4.7, the numerical curve (triangles) for FSR, follows the 1/R dependence, predicted by Eq. 4.4. The simulation curves have been validated by experimental results (data points). The transmission period (data points) decreases from 64 to 25nm as the disk radius is changed from $\approx$ 4 to 6μm, also which is in general agreement with theoretical predictions. The difference between the experimental points compared to the simulation values have to be attributed to the fact that the WDR configuration is very sensitive to slight changes in geometry due to fabrication imperfections.

Another important parameter which benchmarks the disk performance is the modulation depth $h = (T_{\max} - T_{\min})/(T_{\max} + T_{\min})$. Numerical simulations performed for all the considered radii from 1.5 to 6.5μm, in incremental steps of 0.5μm, with a fixed gap g = 100nm, show that for smaller radii the modulation depth is rather small. This is due to the fact that the mode suffers from significant radiation losses, [86] and thus, coupled in the waveguide output does not significantly influence the interference outcome. Then, through the region of R = 2.5 to 3.5μm, the modulation depth increases and at radii larger than 3.5μm, it saturates

at the level close to 100%. Taking into account that the maximum transmission $T_{\max}$ (as defined in Fig. 4.6(d)) monotonically decreases for radii $R > 4.5\mu$m (from $T_{\max} = 0.7$ at $R = 4\mu$m to $T_{\max} = 0.5$ at $R = 6.5\mu$m), it can be concluded that the WDR disk radius around $R = 4\mu$m is the optimal in terms of modulation depth-maximum transmission trade-off.

4.3.2 WDRs - Separation Gap Dependence

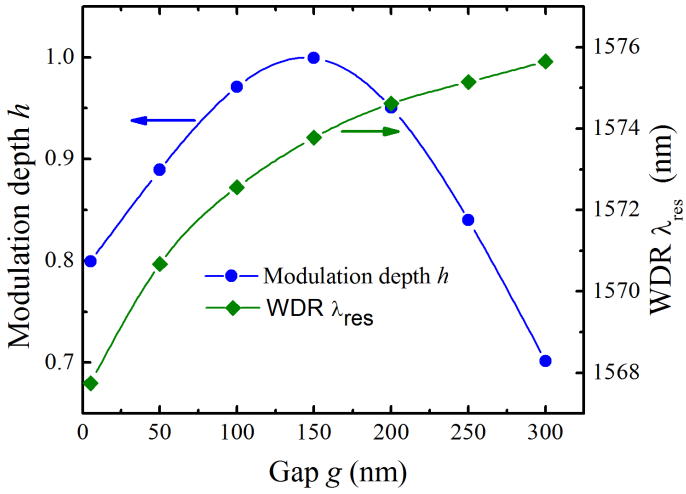

Figure 4.8: *Numerical results: dependence of the modulation depth h(circles) and WDR resonant wavelength λ_{res} (diamonds) and on the separation gap at a constant disk radius $R = 4\mu$m*

The separation gap between the waveguide and the resonant disk plays an important role in determining the coupling strength of the resonant mode. For each disk radius there is an optimal gap corresponding to the largest modulation depth. This has been confirmed by the experimental data for $R = 4\mu$m (not shown here) and different gap sizes ranging from the contact case ($g = 0$nm) to $g = 300$nm. Figure 4.8 shows the simulated response of the WDR resonant wavelength λ_{res} and modulation depth h, when the gap is varied (circles). A drop in the modulation depth or extinction ratio is observed when the gap is too large or when it is zero. For modulation depth an optimal evolution is seen with respect to the increasing gap size between the waveguide and the disk. It is

largely dependent on the coupling strength and the SPP propagation loss. The bend losses which are associated with the radius of the disk do not play an important role in this study, as the radius of the disk is kept constant. Naturally, there is a slight change in the resonant wavelength λ_{res} (Fig. 4.8, diamonds) when the gap changes, which is connected with the coupling-induced phase shifts (CIFSs) [88].

4.3.3 WDRs - Quality Factor

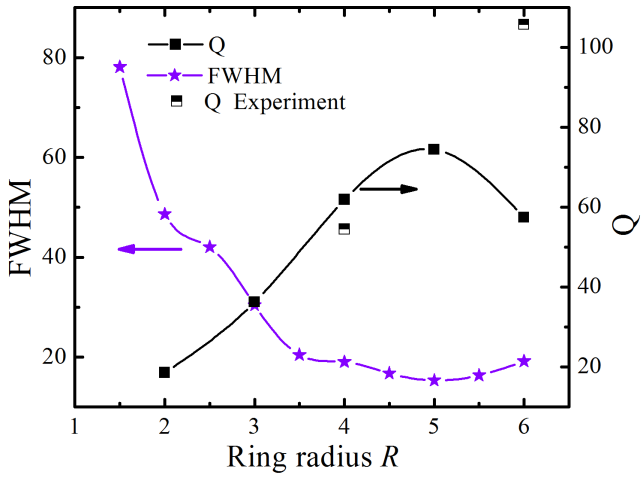

Figure 4.9: *Calculated dependence of the quality factor Q on the disk radius. Experimental data for $R = 4$ and $6\mu m$ is indicated by half filled black points. The numerical dependence of the full width half maximum (FWHM) of the resonance on the disk radius is also shown.*

A maximum quality factor Q is obtained when $Q = \lambda_{res}/\Delta\lambda$, and ($\lambda_{res}$ is the resonant wavelength, $\Delta\lambda$ is its full width half maximum. For optimal radius at $R = 5\mu$m with $Q \approx 75$ (see Fig. 4.9) is not much different from the optimum radius in terms of modulation depth. From the experimental results the estimated values were $Q \approx 55$ for $R = 4\mu$m and $Q \approx 105$ for $R = 6\mu$m. The trend for Q is largely due to the full width half maximum $\Delta\lambda$, which shows a sharp decrease (more than 50%) when the radius increases from 1 to 3μm (see Fig. 4.9). It continues to show slight decrease further as the radius increases to 5μm. These sharp resonances enables high Q factors, which makes these type of resonators

very attractive for different tuning applications.

4.4 Summary

In conclusion, efficient and compact wavelength selective DLSPPW disk resonators operating at telecom wavelengths were realized. By combining SNOM characterization and numerical modeling, the role of various important parameters such as the disk radius and gap separation was analyzed, and it was shown how they can be used to optimize the device performance in terms of the modulation depth and wavelength selectivity. The disk resonator design is not just superior to its ring counterpart because of easier fabrication and smaller radiation losses but also provides slightly better performance in wavelength selection for integrated photonic circuitry.

Chapter 5

Active I: Electro-active Plasmonic Component

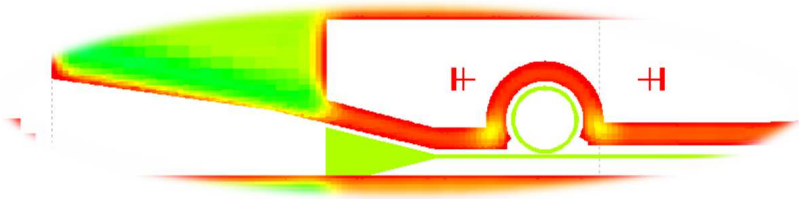

There has been previous demonstration of SPP modulation via different mechanisms including electro-optical (EO) control and thermo-optical control. [67]. In chapter 4, it was shown how a plasmonic element consisting of a waveguide ring resonator (WRR) makes a promising candidate for wavelength selection and moreover active control of surface plasmon polaritons (SPPs) [57] [37]. Additionally the WRRs are compact and thus promising in terms of achieving compactness and integration with current electronic devices [89]. According to the simulations shown in the previous Chapter, a refractive index change of just a fraction of a percent is expected to significantly alter SPP signal transmission through the coupling waveguide. These changes in refractive index can be introduced by doping the polymer with suitable electro-optic chromophores doped in the host polymer. For electro-optic modulation of SPP in WRR geometry we have chosen a strategy whereby we combine an active polymer with good electro-optical coefficients with a WRR operated with integrated in-plane electrodes. The major advantage of DLSPPW technology is in having simultaneously at hand a plasmonic and electrical circuit, whose metal stripes can be employed. e.g. for applying voltage thereby inducing a electro-optical effect in the plasmonic waveguides by changing

the refractive index of the ridge. While the resulting low modulation amplitudes, typically of a few percents, can barely be used for building switches and modulators, this configuration might be potentially attractive for out-of-band processing where low amplitude modulators are used to control the operations of the different elements of the chip without interfering with the data flow.

This chapter starts by considering different suitable electro-active materials, their nonlinear properties and the suitable processing methods. Subsequently, different electrode designs are discussed in terms of compatibility with fabrication and applying optimum electric field across the polymer load. Next, the implementation of the chosen design is shown and the fabrication of the complete EO device (including electrodes as well as the patterned waveguides) is discussed along with the challenges faced. The initial characterization of the EO samples was done via SNOM performed by Dr. Tobias Holmgaard Stær whereas later leakage radiation microscopy (LRM) was used to measure the performance of the electro-active WRR. It was found out to be a more reliable and faster technique than near-field microscopy for characterizing EO WRRs [35, 75, 90, 91]. The results (via LRM) presented in this chapter were performed by Sébastien Lachèze and Dr. Alexandre Bouhelier.

5.1 Electro-active Polymers

To achieve an optimal modulation of refractive index, it is important to choose the best nonlinear polymer amongst the available materials and further optimize the electro-active properties of the chosen material. The next section describes in details, the origin of nonlinearity, material processing and nonlinear optical characterization of the each of these active media. Based on the previous calculations, two families of polymers were identified.

- We identified first, a family of polymers with electro optical activity (Kerr EO activity) based on birefringence of chromophores in low glass transition (T_g) polymers, which offers high changes of index

$\Delta n = (10^{-3} - 10^{-2})$ without any need for poling, but with slower switching time (≈ 0.1ms).

- Second Disperse-Red 1 (linear or Pockels EO activity) was optimized to provide small refraction index changes of the order of 10^{-4} but with fast switching time (≈ 0.1ns).

5.1.1 Kerr-EO Polymers

Organic electro-active polymers composed by a mixture of polymer matrix serving as a host and a guest material, e.g. nano-meter sized, electro-optic active chromophores may feature a quadratic electro-optical effect (proportional to the squared of applied electric field). A typical polymer composite is produced by a host polymer matrix which is then doped with plasticizers to reduce the T_g of the composite. Then chromophores are added to confer electro-optic properties to the mixture. The chromophores play a central role for optimizing the properties of polymer composites, since they are responsible to provide the electro-optic response of the material. Their remarkable electro-optic properties allow them to be used in a wide range of photonic applications [92]. The electro-optical activity is here based on a space charge electric field due to the mobile electron-hole pairs, which gives rise to a change in the refractive index of the polymer because of the orientation of the chromophores by the external electric field.

The optimization of the effective electro-optic coefficient generally involves the synthesis of push-pull molecules with a strong permanent dipole moment and a large change in dipole moment upon excitation, as characterized by the molecular second order polarizability. Reorientation of the chromophores under the combined effects of the space charge and applied external electric fields leads to a modulated birefringence, further enhancing the refractive index modulation. Such polymeric materials are characterized by large electro-optic coefficients and simple preparation technology and have attracted much attention in the fields of integrated optics and optical telecommunications. The electro-optic properties of organic polymer composite materials have enabled designing and manufacturing optical switches and optical switch arrays [93, 94]. Recent studies by groups specialized in polymer and dye chemistry re-

ported on a new generation of electro-optical polymers featuring much stronger electro-optical coefficient (reaching up to 500pm/V) combined with very good stability [95–97]. At this stage, these polymers are not yet available commercially but can become particularly relevant for the future development of electro-optical plasmonics.

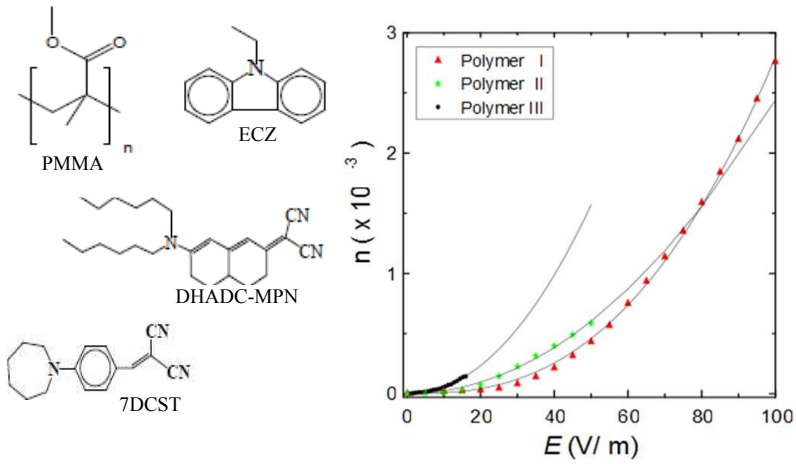

Figure 5.1: *(left) The different constituting nonlinear chromophores such as 7DCST and DHADC-MPN were mixed is different concentrations in a PMMA host matrix and a placticizer ECZ was mixed to lower T_g. (right) Δn shows a quadratic dependence on the applied electric field ($V/\mu m$). The electro-optical properties can be engineered by changing the ratios of the chromophores. The different electrical field ranges investigated, are due to the different breakdown field for the different layers.*

The Kerr electro-optic effect which induces an Δn change is proportional to the square of the electric field as can be seen by the quadratic dependency of Δn with respect to the applied voltage as displayed in the measurement in Fig. 5.1. Each polymer contains PMMA (Poly(methyl methacrylate)) matrix doped with different combinations and ratios of nonlinear chromophores such as 7DCST (4-homopiperidinobenzylidenemalononitrile), HR254 and GW83B. Also, a plasticizer ECZ (N-ethylcarbazole) was added to lower the glass transition temperature of the respective polymers (see Fig. 5.1). The displayed data for three different electro-active polymers displays the strong dependence of the Δn on the ratios of the different constituents.

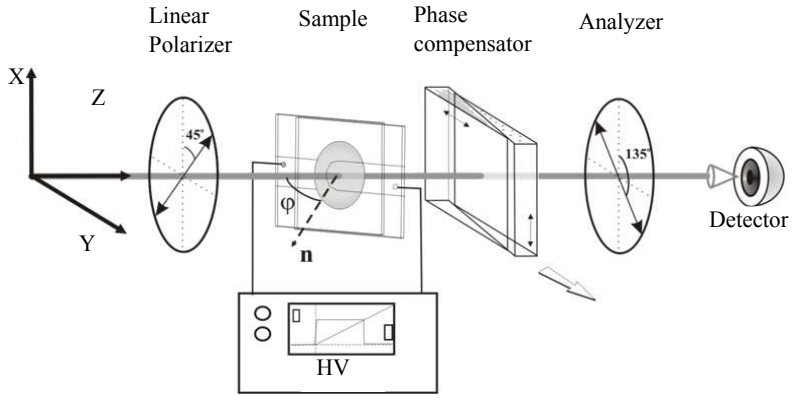

Figure 5.2: *Sketch of the ellipsometry set-up used for measuring the electro-optic coefficient. This figure is reproduced from Ref. [98].*

This way, one could prepare electro-active materials which exhibit Δn changes in the range from 10^{-4} to 10^{-2} (depending on the concentration of the constituting chromophores). The applied electric field can reach up to 150V/μm because of the high resistance of the photorefractive polymer layer. The total Δn change strongly depends on the concentration of each of the chromophores and other thermal factors such as glass transition temperature. We have optimized the concentration of the different constitutive chromophores in order to get Δn changes as large as possible. The prepared layers have been analyzed using ellipsometry [98, 99]. This technique (see Fig. 5.2) is based on the polarization rotation of a laser beam due to the electro optic effect.

Depending on the electrodes substrate chosen, the measurement can be performed either in reflection or in transmission. The samples for transmission measurements are typically made by melting polymer and sandwiching a few microns thick layer between glass substrate pre-coated with conductive indium tin oxide (ITO) electrodes. A laser beam is incident on the back of the glass substrate at an angle θ and travels through the substrate, the polymer layer and is transmitted in the case of a top ITO electrode or reflected back to the air in case of a top gold electrode. The polarization of the input beam is initially set to 45° with respect to the plane of incidence so that the parallel (p-polarized wave) and perpendicular (s-polarized wave) components of the optical field are equal in

amplitude. In this configuration, the phase delay between the s- and p-waves is modulated using the Soleil-Babinet compensator. The output laser intensity I at the detector or transmitted through the analyzer should be half of its maximum value and can be described by the Malus's law i.e. $I = I_{\max} \sin^2(\delta + \delta_{wp})$, where δ_{wp} is the phase delay introduced by the wave plate. When a modulating voltage is applied across the electrodes, a change in phase $\delta\Psi$ in both the s- and p-waves is induced by the change in refractive index Δn due to the electro-optic effect and orientational birefringence. This change in the refractive index can be estimated for a given thickness of the polymer film and the wavelength used for characterization.

The results for some of the studied material combinations are given in Fig. 5.1. The prepared samples have been characterized at a telecom wavelength of 1550nm. This type of EO polymer show a Δn of the order of 10^{-3}, change at least 10 times higher compared to linear EO polymers such as PMMA-DR1. The absorption peak for this material lies in the visible spectral region; hence, the working wavelength has to be chosen around 630nm or higher. The differences in the electro optical properties of the different materials considered in Fig. 5.1 are due to interactions between the different chromophores associated to the overlapping of their absorption peaks. Significantly higher Δn values, up to 10^{-2} for E-field of 50V/μm, are expected by further optimizing the concentration of different chromophores. Also a larger change in refractive index can be achieved by further increasing the applied voltage or decreasing the thickness of these films and bringing them down to the order of few hundreds or tens of nanometers.

5.1.2 Pockels EO Polymers

Commercially available polymers with linear electro-optical activity (Pockels-effect) such as disperse-red 1 (DR1) and disperse-red 13 (DR13) enable electro-optical coefficients (d_3) of the order of 30pm/V associated to changes in refraction index of $\Delta n \approx 10^{-4}$ (assuming an electric field of 2V/μm) as measured via a computer-controlled automated set-up based on attenuated total internal reflection (ATR) [100]. These polymers in contrast to the low T_g polymers require poling (process of

orienting molecules via applied electric field) before an EO effect can be observed.

A powder of DR1 molecules (Sigma-Aldrich) were dissolved in chlorobenzene, stirred for 24hours and filtered in order to obtain a more homogenous yet diluted solution. Then depending on the desired weight percentage, a given amount of DR1 is mixed with a solution of PMMA and chlorobenzene and kept stirring for about 2hours. We found a weight percentage of $\approx 25\%$ (calculated based on respective solution densities before filtering) for DR1-PMMA to be optimal in terms of maximizing the nonlinear activity yet avoiding high absorption losses. In order to obtain films of DR1, the solution was spin coated onto the substrates at thicknesses around 600nm, followed by drying of the spin-coated films at 65°C in an oven to evaporate the solvent.

5.1.3 Compatibility of EO Polymers

During our extensive work in the clean room we had realized, that the option of photorefractive materials is not compatible with the e-beam lithography, because the low glass transition temperature (T_g), chromophores are too readily dissolved by the developer (methyl isobutyl ketone or MIBK). Considerable efforts were made at the collaborating institute to find alternative low T_g EO materials by testing out various combinations of different chromophores and plasticizers doped into PMMA matrix. But the lack of success in this respect pointed out to the fundamental limitation of a low T_g material which is naturally rendered porous when chromophores are doped into the PMMA matrix, hence making it easily dissolvable in developer MIBK (Methyl isobutyl ketone), which has a strong chemical impact on these materials. Therefore we limited ourselves to DR1 given its compatibility with the fabrication process.

5.2 Electrode Design

In order to modulate the optical properties of the poled polymer, an electric field needs to be applied across the dielectric loading. This has been

realized by building a metal-polymer-metal planar waveguide structure for the electro-optical characterization of DR1. The electric field applicable in such planar metal-insulator-metal (MIM) structures was up 70V/μm. Unfortunately, simply using the electrode design of the MIM to the dielectric loaded waveguides further reduces the propagation length of the DLSPPW-mode. Moreover, these type of electrodes are very cumbersome to fabricate and raise problems in contacting the top electrode on the ring. Therefore, alternative electrode designs have been analyzed by FEM modeling.

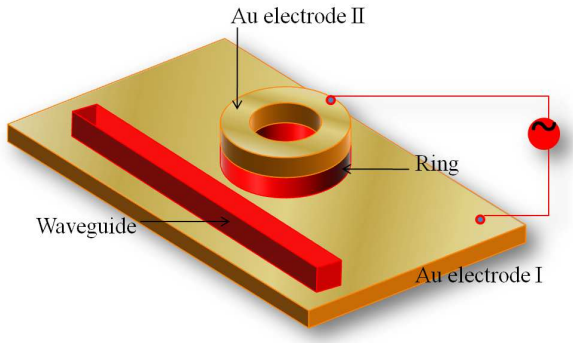

Figure 5.3: *Schematic of the vertical electrode design.*

In order to overcome the above mentioned issues of vertical electrodes (shown in Fig. 5.3), alternative in-plane electrode designs as depicted in Fig. 5.4 have been investigated by using FEM modeling.

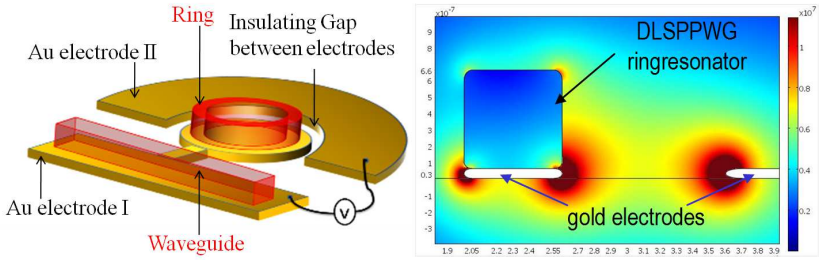

Figure 5.4: *Left: 3D view of the in-plane electrode design; Right: associated transverse electrostatic field distribution at one edge of the ring (10V bias).*

Figure 5.4 shows the electro-static field distribution calculated in the vicinity of such electrodes for polymer waveguides. The in-plane design served the dual purpose of not only providing electrodes with which an electric field could be applied but also for supporting the SPP at the Au-polymer interface. Also, the fabrication of such electrodes is technologically feasible via a two step-lithography. However, the disadvantage of using in-plane electrodes is that the electric field concentration within the polymer is lower which means the changes in refractive index could be relatively smaller. Figure 5.4 (left) shows a configuration where the otherwise homogeneous gold film is patterned to create an isolating tranche, enabling to apply an electric field across most of the polymer load forming the ring. Although weaker compared to vertical electrodes, FEM simulations show significant electric field gradient across the polymer section. In practice, the patterning of the electrodes and the dye-doped polymeric-DLSPPW has been realized by 2 successive steps of e-beam lithography. This method features a high flexibility for design adjustment and high resolution needed in particular to achieve gap of 250nm in between the straight DLSPPW and the ring resonator.

5.3 Fabrication

The fabrication of the DLSPPW ring resonators was done via a multi-step bottom-up fabrication routine as sketched in Fig. 5.5. It required two-step lithography, whereby the first step involved the exposure of a 250nm PMMA layer on Au. After the development, the pattern was exposed to argon plasma in a reactive ion etching chamber, which etched the Au below for areas that were exposed (PMMA being a positive resist). This way the fabrication of in-plane electrodes was achieved. Subsequently, the EO polymer was spincoated over the electrodes, followed by poling of the EO polymer via the in-plane electrodes. Finally, the overlay of the ring resonators on top of the designed electrodes was accomplished with precise alignment (with an accuracy of about 20nm). More details with respect to patterning of the electrodes and WRRs can be found in the following sections.

In fact, proximity effect corrections (PEC) were used for patterning both the electrodes and the waveguide ring resonators (Fig. 5.6) [101]. It was

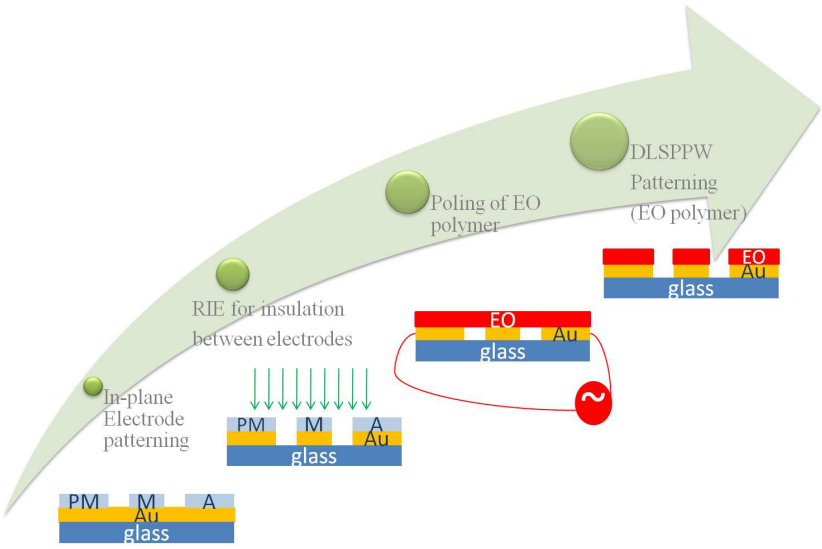

Figure 5.5: *An overview of the fabrication procedure which involves multi-step lithography and processing*

critical to invest big efforts in the overlay accuracy as well as on the calculation of the effectively deposited energy with respect to proximity effect, as the coupling efficiency of the waveguide to the ring depends strongly on the geometry and placement of the exposed structures. The proximity parameters are directly obtained from Monte Carlo simulation of the scattering process of the electrons in the resist/metal/substrate system as the actual dose basically depends on the applied beam energy, the substrate material, the resist type and the thickness and the development process. Before the real exposure is performed, the processing of the proximity effect corrected design is simulated by energy density simulation. This approach guarantees high efficiency and accuracy of the EBL process. Using the PEC, we could fabricate gaps as small as about 50nm.

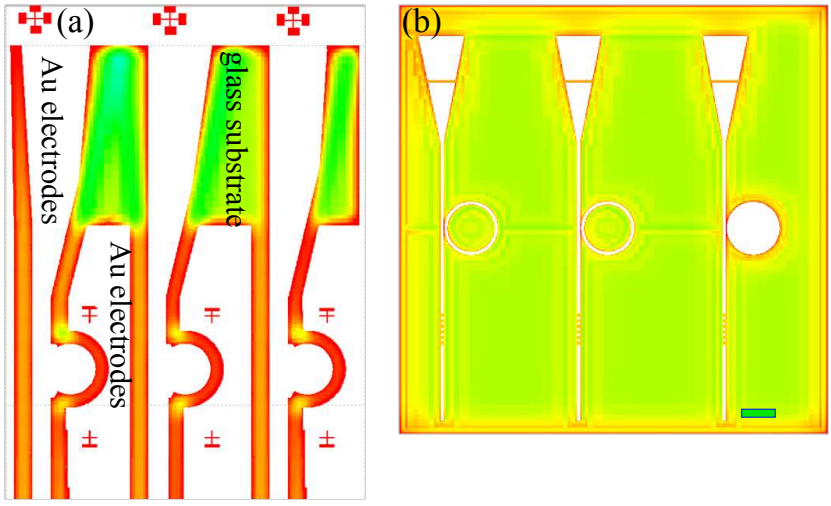

Figure 5.6: *(a) GDSII design after proximity effect correction of electrodes. (b) GDSII design after proximity effect correction of the waveguide ring and disk resonators. The cross-like structures are alignment marks for the second lithography. Note: Green/yellow and red colors indicate low and high doses, respectively. Scale bar is 5µm.*

5.3.1 Electrode Patterning

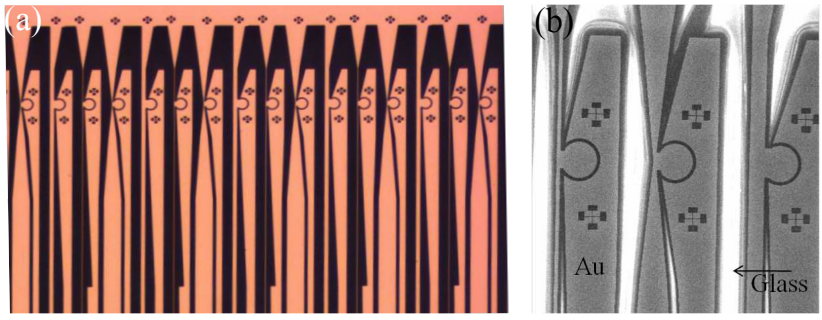

Figure 5.7: *(a) Optical microscope image showing a repeated unit cell; (b) SEM micrograph of an unit cell of electrodes.*

The electrode layout consists of an unit cell of three different geometries (in order to check the influence of the finite extension of the Au film),

repeated over 0.5mm as shown in Fig. 5.7(a) and (b). Different types of electrode layouts were tested out at the beginning, including both having both narrow (1μm-narrow Au stripe) and wider Au supports. However, due to possible charging effects during the second lithography step, wider electrodes were found out to be most suitable. The electrode design for subsequent samples was modified accordingly.

In our configuration, the edge of the straight waveguide is designed to be 700nm away from the metal edge to avoid unnecessary damping of the plasmon mode at the edges. Following the same argumentation, the metallic bottom of ring resonator extends beyond the ring diameter R by a value w_s of 700nm as shown in Fig. 5.8.

The fabricated electrodes were electrically tested in order to evaluate both their damage and short cut thresholds. Up to 100V (or 55MV/m) have been successfully applied on the three different geometries without obtaining structural damages.

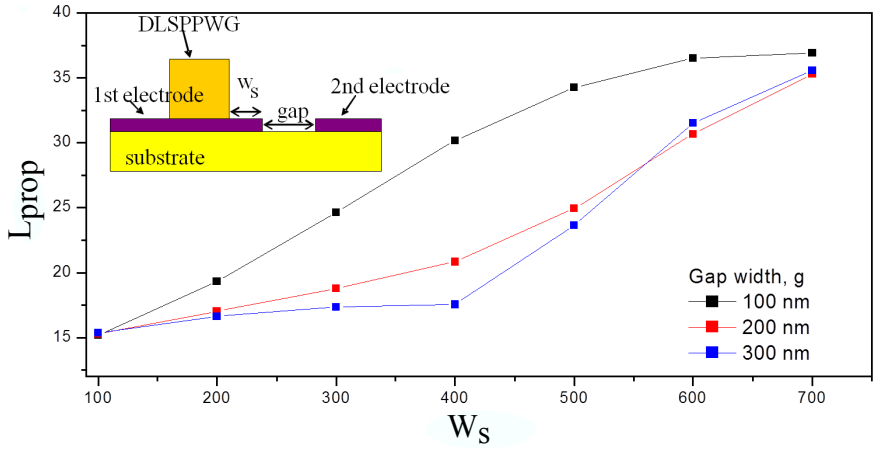

Figure 5.8: *The propagation length L_{prop} is reduced for DLSPPWs placed close to the edge of the electrode. Therefore, a sufficient overlap of around $w_s = 700nm$ is needed to avoid a strong damping of the mode. Based on FEM calculations. Courtesy of A.Krasavin, King's College.*

5.3.2 Waveguide Patterning

On the fabricated electrodes, a 500nm-thick EO polymer film was spin-coated and the waveguides are patterned by a second step of e-beam lithography. The cross-like structures were used as alignment marks (see Fig. 5.6(a)) in order to center the ring on the electrode with an accuracy of about 50nm.

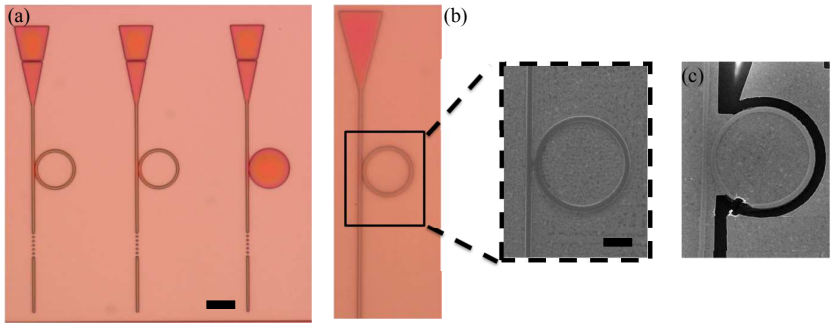

Figure 5.9: *(a) Brightfield microscope image of one write field area (100 by 150μm) containing two polymer waveguide rings and one disk resonator.Scale bar is 10μm, (b) SEM micrograph of a single ring resonator structure on a continuous Au film. Scale bar is 4μm, (c) SEM micrograph of a single structure with electrode below. The defect in the bottom left of the ring was most probably caused by a dust on the substrate.*

Strong proximity effects previously observed in the small separation region in between the straight waveguide and the ring resonator were successfully overcome by using advanced dose correction (see Fig. 5.6(b)).

After establishing the fabrication procedure for the DLSPPW ring resonator on unpatterned Au films (see Fig. 5.9 (a)) both lithography steps were combined to obtain the final structures with their in-plane electrodes. In order to avoid further e-beam exposure of the polymer structures (which would affect their optical properties) dark field microscopy was used for non destructive optical inspection. The success rate for structures that were not damaged or interrupted was initially of about 30%. This can be attributed to the fact that instead of having an extended Au film below them, there was instead a combination of Au and glass which gave rise to significant changes in exposure parameters and

conditions. (Fig. 5.9(c) shows SEM micrograph on one structure featuring a defect.

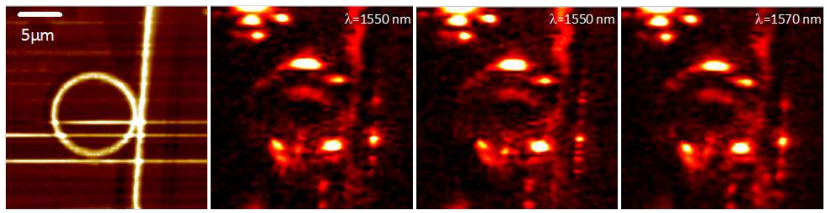

Figure 5.10: *Topography (left) shows the dielectric ring resonator made of DR1-PMMA on top of a structured Au film. The recorded optical near-field intensity shows bright spots at all wavelengths and has to be attributed to scattered background light from the illumination. Courtesy: Tobias Holmgaard, Aalborg Univerity*

The first batch of samples was analyzed (as shown in Fig. 5.10) using SNOM in order to check the stop-band like behavior (or dips in Transmission during wavelength scans). As per the recorded near-field images in Fig. 5.10, no wavelength selective coupling to the ring has been found despite the mode visible on the DLSPPW. Furthermore, plenty of bright spots at the ring resonator as well as on the alignment marks (located at the upper left corner) were observed, which originates most likely from scattered background light from the illumination.

In order to uncover the problem(s) the structures were refabricated on a planar gold film where much less background is expected. The SNOM images displayed in Fig. 5.11 clearly confirmed the expected stop-band like behavior, resulting in low transmission at certain λ, e.g. 1540nm and 1590nm.

The strong, clearly visible coupling at the stop-band such as $\lambda = 1540$nm, was not observed on the structured electrode pointing towards a problem with the quality factor of the ring resonator. This problem was addressed by a theoretical analysis and lead to the conclusion that a minimum distance $w_s = 700$nm in between the DLSPPW and the edge of the metal needs to be kept in order to not affect the propagation length of the DLSPPW. The graph in Fig. 5.8 could also explain the bad performance of the ring resonator used in former experiments shown in Fig. 5.9(c)

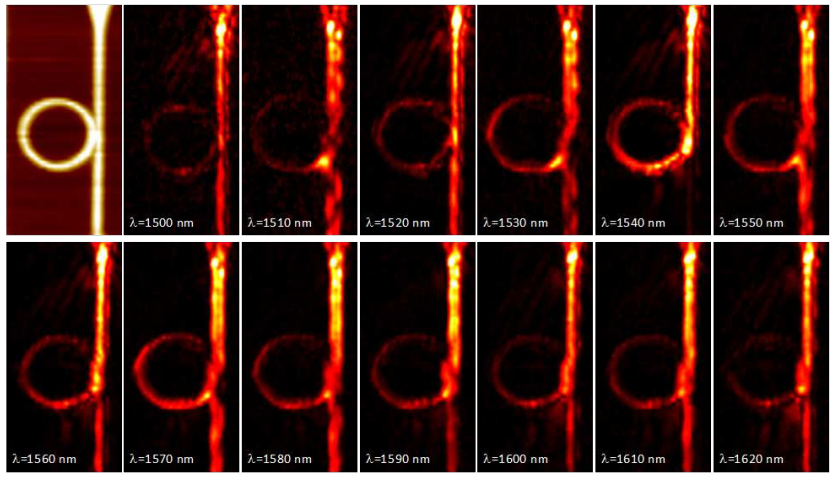

Figure 5.11: *Topography (left) shows the dielectric ring resonator made of DR1:PMMA on top of a (unstructured) planar Au film (gap width = 300 nm, radius = 5.086μm). The optical near-field intensity measured at various shows a stop-band filter behavior whenever the DLSPPW-mode is coupled to the ring, e.g. $\lambda = 1540nm$.*

in which w_s was negative in order to have a strong electrostatic field inside the DLSPPW as observed in theoretical simulations before. Such an arrangement introduces strong damping thereby circumventing the quality of the (optical) ring mode. Therefore new generation of samples were modified in order to let a distance of w_s = 700nm between the waveguide and the metal edge.

5.3.3 Electro-optical Functionalization

The electro-optic functionality originates from the oriented molecular dipoles of the DR1-dye in the PMMA matrix which can be achieved by so called poling. The poling process is done by heating the sample close to the glass transition temperature while applying an electric field. The orientation of the dipoles is then "freezed" when cooling the sample. Because of the elevated temperatures used, the poling process has to be done before structuring the DLSPPW. Typically, a sandwich electrode geometry is used in order to apply the poling field. For the EO DLSPPW

ring resonators that would require depositing a top metal layer above the DR1-PMMA layer which needs to be removed after poling. However, it turned out that after the poling process and etching of the top electrode via reactive ion etching (RIE), the following e-beam structuring of the DR1-PMMA layer was not successful because of changes of the layer by the etching process itself. Bubbles and craters in the polymer layer appeared as displayed in Fig. 5.12(a). After repeated tests it was concluded that RIE on polymer layers lead to this problem. This could have been due to either the temperature of the substrate in the RIE chamber or because of the bombarding ions were damaging the DR1-PMMA layer. Tests have shown that high vacuum inside the chamber was not a contributing factor and hence the argon-ion plasma or the UV light produced by it is the only remaining source of the polymer-modification.

Furthermore, we checked whether a macroscopic electrode separated by a spacer of a few tenth of microns away, could be used as counter electrode. Unfortunately, the dielectric breakdown took place at quite moderate poling electric field strengths leading to ablation of the Au electrode and the polymer. An alternative solution was to use the in-plane electrodes themselves for poling. The main advantage of using the in-built electrodes for poling is that there is no need for their removal after poling. The tested electrodes having a gap of 5microns could sustain up to 100V. Beyond this threshold value, the electrodes show slight signs of damage due to surface currents. Samples were poled by this way for about 30 minutes at 105°C and then cooled down to room temperature under applied electric poling field in order to freeze the oriented state of DR1 molecules.

Unfortunately, the patterning of the DLSPPWs was not always successful as displayed in Fig. 5.12 (b), even if the clearing dose for the polymer removal was checked before on the unstructured part of the electrode. It turned out that the second lithography is challenging because - beside the required accuracy in positioning (better than 100nm) - the poor conductivity of the 500nm-thick DR1-PMMA layer and the inhomogeneity of the patterned electrodes causes charging that reduces the lithographic resolution.

The characterization of the samples using SNOM revealed a poor coupling to the DLSPPW-mode. This unexpected problem was caused by the

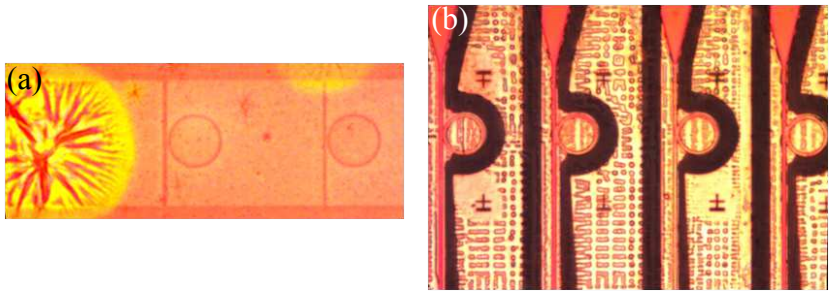

Figure 5.12: *(a) Optical images of structural damage of the DR1-PMMA layer during the RIE process which prohibits the use of a top Au electrode for poling. (b) Incompletely removed DR1-PMMA layer which has been poled using the in plane electrodes.*

increase of the refractive index of the DR1-doped PMMA compared to the undoped one as confirmed by ellipsometric investigations. The DR1 doping leads to an increase of the mode effective index above $n_{eff} = 1.5$, making an excitation based on the Kretschmann-Rather-configuration impossible in the triangular-shaped funnel region as illustrated by table 5.1.

Height (nm)	$Re(n_{\text{eff}})$	$Im(n_{\text{eff}})$
100	1.072986	2.61E-003
200	1.242404	5.68E-003
300	1.401866	6.04E-003
400	1.490402	5.28E-003
500	1.538104	4.01E-003
600	1.565317	3.58E-003

Table 5.1: *Real and imaginary part of the mode effective index of the SPP-mode in a layered system having a polymer layer with $n = 1.6$ on top of a 60nm-thin Au-film on BK7. The SPP can not be excited for polymer layers thicker than 400nm in Kretschmann-Raether-configuration.*

In order to facilitate the SPP coupling in the funnel region we had to reduce the thickness of the polymer layer to 300-400nm while keeping the other lateral dimensions constant. The SNOM characterization of these samples confirmed that the SPP excitation has been improved drastically.

In order to prove the stop-band characteristic of such a ring-resonator structure the wavelength has been swept from 1525 till 1625nm while scanning the exit side of the resonator structure as depicted in Fig. 5.13. This small scan area was chosen intentionally in order to minimize the impact/damage by the SNOM tip of the ring structure while measuring. Unfortunately, it turned out that scanning only the exit part and omitting to scan and optimize the in coupling funnel does not allow for the compensation of the different in-coupling efficiencies and small lateral drifts of the laser when changing the wavelength. Moreover the intensities shown in Fig. 5.13(c) have been drifting/fluctuating which prevented us from a more quantitative analysis. Especially the low quality factor of the stop-band characteristic of the measured ring-resonators hinders any measurement of the electro-optical modulation (because the EO induced change in transmission would be at maximum at the wavelengths where the slope in transmission is strongest). Moreover, the drift and fluctuation of the intensity turned out being larger compared to the expected electro-optical induced ones, making SNOM not the optimum method of choice for the EO characterization.

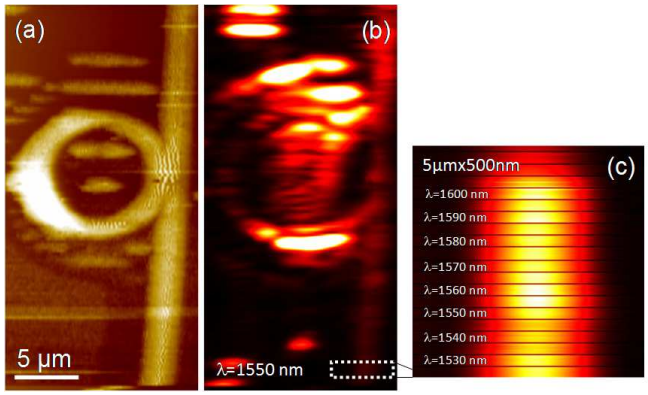

Figure 5.13: *(a) Topography of the ring-resonator structure measured by the SNOM-fiber tip. The edge of the electrode (outside the ring) is visible. (b) Corresponding optical near-field intensity map. Only the small marked area at the exit side of the straight DLSPPW has been scanned during the wavelength sweep shown in (c).*

5.3.4 Final Design of the EO Devices

After solving all the lithography problems, new modifications were added to the design. The electrode design was modified, based on the success rate of fabricating EO WRRs. Moreover, to simplify the fabrication we included disk resonators WDRs (more details in Chapter 4), apart from the ring resonators which proved to be much more robust. The final electro-optic samples contained several ring as well as disk like structures (Figure 5.14(a)).

It turned out that once these improvements were made, the SNOM characterization limited the detectable (small) change due to drift and fluctuations, and the scanning tip damages the structures during the scans. The scanning probe measurements revealed that the strong doping not only affects the electro-optical properties, it also modifies the mechanical ones. The brittleness is increased significantly making the structures more fragile compared to structures made of PMMA only. Hence, we had to replace the SNOM characterization by leakage radiation microscopy. This was done in collaboration with Alexandre Bouhelier and Sébastien Lachèze at l'Université de Bourgogne, France.

5.4 Characterization via Leakage Radiation Microscopy

LRM was also used for characterizing the dielectric plasmonic mirrors in Chapter 3, where it was also introduced.

In the LRM configuration, a diascopic illumination was used to couple a tunable infrared laser source emitting around $\lambda = 1500$nm in the telecom band. A long working distance objective with a numerical aperture of 0.52 focused the collimated laser beam on a $\approx 2\mu$m diameter spot. The lateral position of the objective and the focused spot was adjusted to overlap the taper geometry at the entrance of the waveguide. Typically a better coupling efficiency was obtained when the spot is diffracted by the slit opened in the taper. The polarization of the incident light was controlled by a combination of a polarizer and a half-wave plate. The

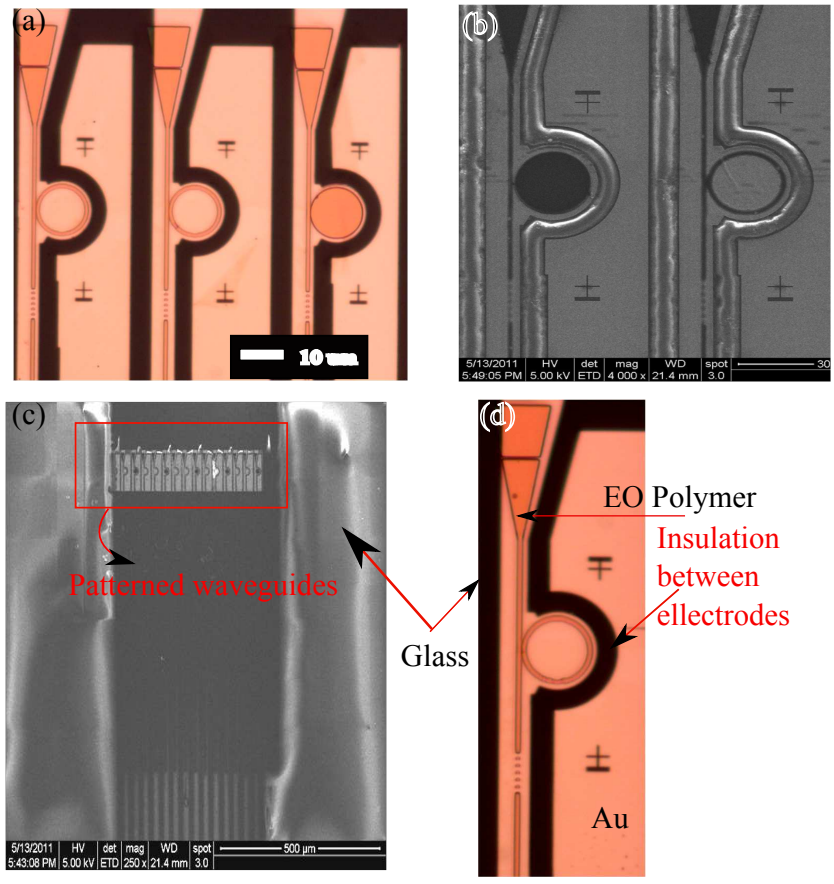

Figure 5.14: *(a) Brightfield image of one write-field(*100 *by* 150μm*)containing two rings and one disk resonator on top of electrodes. Scale bar is* 10μm*. (b) SEM images of the WRRs and WDRs, (c) Over view of the sample containing several areas such as shown in (a), flanked with glass on both sides to separate out the two electrodes, (d) Magnified Brightfield image of the WRR on top of the electrodes.*

leakage radiation of the DLSPP mode was collected by a high numerical aperture objective NA=1.49 and was sent to infrared sensitive camera for imaging purposes. In order to couple to the plasmonic mode in the waveguide an in-coupling defect of width $\approx$ 200nm was fabricated inside the funnel region, on which the laser was focused to launch the SPP waves. Similarly towards the output section of the waveguide a periodic

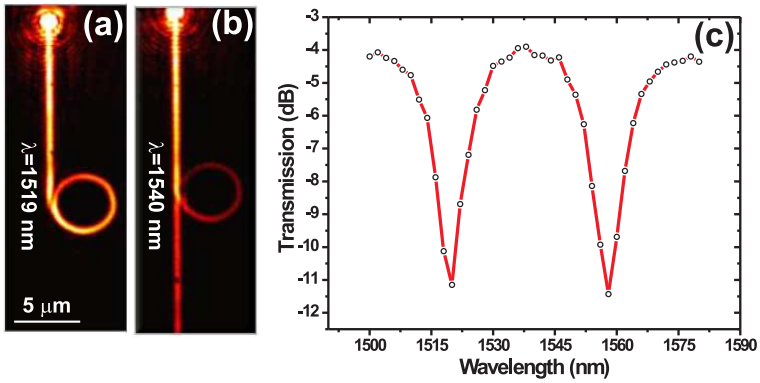

Figure 5.15: *(a) and (b) Leakage radiation images of a SPP mode in a DR1-doped dielectric-loaded surface plasmon WRR on a planar Au film excited on and off resonance, respectively.(c) Measured transmission curve of the WRR showing two rejection bands at 1519 nm and 1557 nm. Courtesy of l'Université de Bourgogne,Dijon.*

grating was provided to render the transmitted mode into a radiative one for efficient out-coupling whereby the width of the grating and filling factor were chosen to be 1.3μm and 50% respectively. This was based on the effective mode index of the DLSPP mode which is 1.29 for a waveguide of width and height of 600nm each. The stop-band characteristic of resonator structures made of undoped and doped PMMA on planar Au films were evaluated using LRM. A typical images of a doped resonator on and off resonance is shown in Fig. 5.15(a) and (b). At the resonant excitation wavelength, here $\lambda = 1519$nm, the transmission of the device is minimum. The spectral response of the WRR is plotted in Fig. 5.15(c) where the transmission T is defined by:

$$T = 10 \log \frac{I_{out}}{I_{in}} \tag{5.1}$$

The input and output intensities I_{in} and I_{out} were evaluated by averaging the detected signal along the waveguide over two 3μm $\times$ 500nm areas placed before and after the ring resonator, respectively. The extinction ratio of the device reaches upto 7dB. This value is typical for WRR

with ring radius $R = 5.480\mu$m and coupling gap $d = 150$nm as also shown in Chapter 4. The quality factor for this device was evaluated at $Q = \lambda_{res}/\triangle\lambda = 190$, where λ_{res} is the resonant wavelength and $\triangle\lambda$ is the full-width at half-maximum of the resonance.

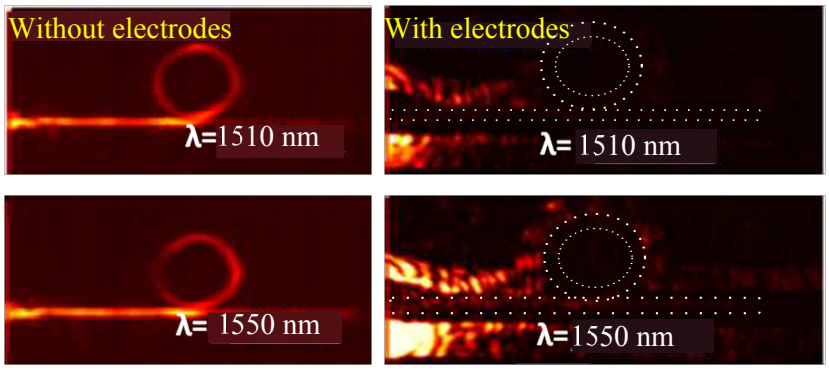

Figure 5.16: *(Left) Leakage radiation images of the disk-resonator structure made of DR1-PMMA on top of a planar Au film.(right)Leakage radiation images of the disk-resonator structure made of DR1-PMMA on top of structured Au film i.e. electrodes, which contributes significantly to the background noise.Courtesy: l'Université de Bourgogne, Dijon.*

For the structures without any electrodes below, the characteristic transmission dips could be resolved. However, in order to resolve the transmission dips for the WRRs patterned on electrodes, background noise correction had to be implemented. The difference in WRR transmission for the two cases (with and without the electrodes) is shown in Fig. 5.16. Corresponding real and Fourier images are also shown in Fig. 5.17(a) and (d).

The electrodes contribute to optical background due to predominantly due to scattering at the edges. One possibility to circumvent it has been to modify the LRM setup shown in Fig. 5.18 and measure using Fourier plane filtering of the LRM.

Drezet et al. demonstrated efficient surface plasmon filtering by placing appropriate beam stops in a conjugated Fourier plane of the microscope [74]. Following this approach, spatial filters were implemented to block the directly transmitted light from the excitation, thereby improving the

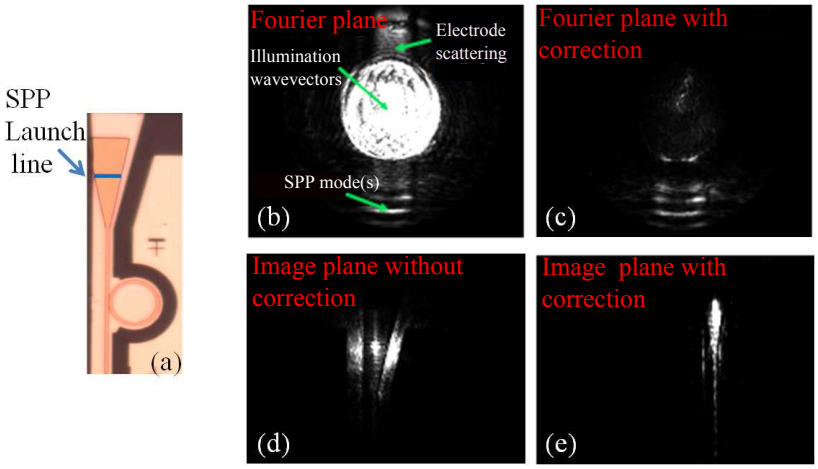

Figure 5.17: *(a) Schematic of the WRR where the SPP is launched via a line defect within the funnel region, (b) Fourier space image when the laser is focused onto the line defect and DLSPPW mode in WRR on top of electrodes are excited, (c) Fourier plane image with filtering in order to select the DLSPPW modes, done via positioning a mask in the Fourier plane to block the illumination and scattering contribution from the electrodes, (d) Direct space LRM image corresponding to (b), (e) Direct space LRM image corresponding to (c). Courtesy of l'Université de Bourgogne, Dijon.*

accuracy of the measurements to a level where a transmission curve can be reasonably obtained as illustrated in Fig. 5.17, which is important for observing modulations on applied voltage. The guided DLSPPW mode appears in the Fourier plane as a bright line as shown in Fig. 5.17(b) which represents in-plane wavevectors having $\kappa_{||} = n_{\text{eff}} \times \kappa_0$, whereas the excitation light is located in the center of the Fourier plane. By blocking the latter one by a mask, most of the excitation and scattered light is suppressed and the DLSPPW mode is highlighted in the image (see Fig. 5.17(e)).

The response of WRR doped with poled DR1 molecules combined with the electrode layout discussed above, was investigated. A typical image on and off resonance of the device for a null bias was recorded respectively. After the demonstration of detection of the WRR mode, the next step was

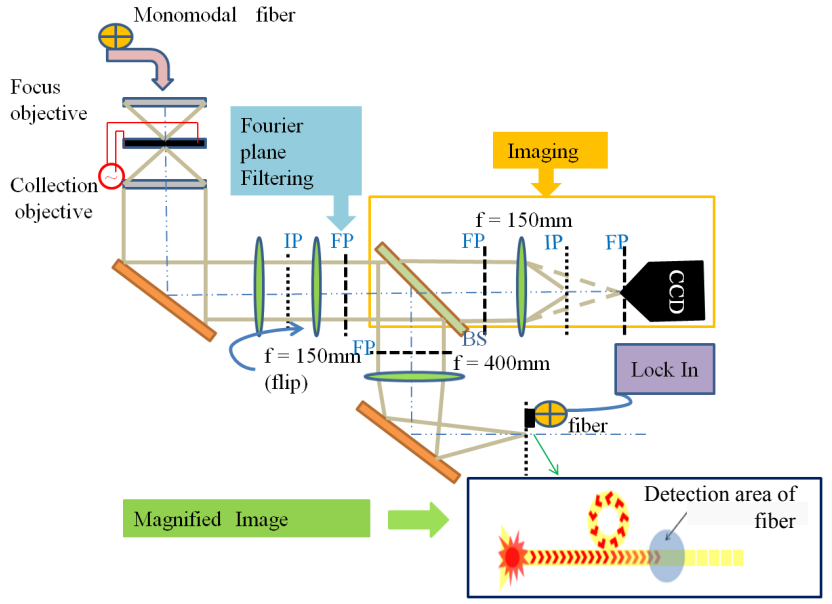

Figure 5.18: *Setup of the LRM. The leakage radiation collected from the SPP is divided into two paths, one part goes to the CCD and the other is collected by the optical fiber. Fourier plane (FP) filtering is used to get rid of background noise due to scattering of the light at the electrode. A magnified image of the sample is produced at the image plane (IP) where a fiber is placed to measure the output transmission of the WRR.*

to observe the modulation of DLSPPW mode upon electrical activation of the DR1 doped polymer. In order to investigate the dynamic or temporal response of the doped polymer WRRs, the standard technique of end-fire in/out coupling used before was not sufficient. Since a camera has limited time resolution, a confocal-type detection using an optical fiber coupled to a photomultiplier was used (Fig. 5.18). The position of the fiber core was adjusted on this conjugated image plane to detect the output region of the WRR. From the known core diameter and the magnification of the conjugated plane, the confocal detection area was estimated to cover a diameter of approximately 3μm. The optical fiber was connected to a photomultiplier and lock-in has been used for sensitive detection of the modulated laser intensity. A good agreement of WRR transmission was obtained between the two measurements i.e. one acquired via CCD and

another with the optical fiber (data not shown here). The wavelength dependance of I_{out} for a null bias is shown in Fig. 5.22(a). Despite a remaining noise due to limited spatial filtering, two rejection bands are clearly visible on the curve at 1517nm and 1554nm with an extinction ratio around 2.

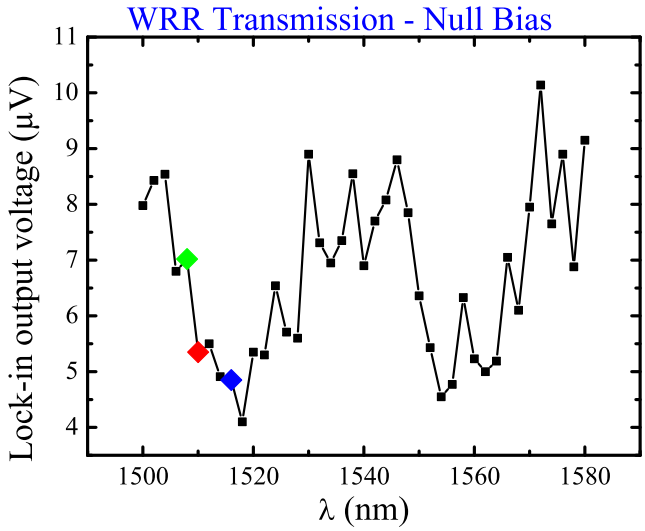

Figure 5.19: *WRR transmission measured with optical fiber and lock-in detection. Green, red and blue points indicate wavelengths (1508, 1510 and 1516 nm, respectively) at which the transmission modulation is measured. Courtesy: l'Université de Bourgogne, Dijon*

We monitor the evolution of I_{out} for three wavelengths as indicated by colored dots in Fig. 5.19 in the proximity of the first dip to observe modulation as a function of a static electric field applied between the in-plane electrodes. Figure 5.20 shows the results. A strong relative variation occurs as the electric field is increased up to 8MV/m for the three wavelengths. The trend for low electric field indicates a red-shift of the resonance with voltage. A sharp fall of the output amplitude is observed after 8MV/m where I_{out} oscillates around its value at null bias.

To further investigate, we focused on the kinetics of WRR output signal I_{out}. The I_{out} temporal response is correlated with the microscopic mechanisms responsible for the observed variation. Kinetics were measured

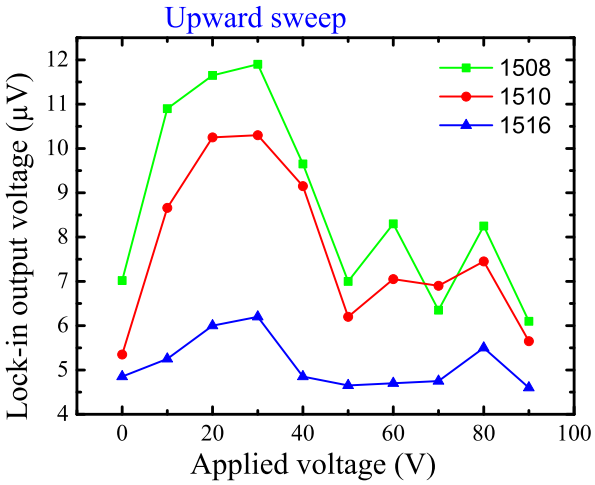

Figure 5.20: *Shows the evolution of transmission for each of the wavelengths (1508nm (green), 1510nm (red) and 1516nm (blue), respectively) as the voltage is sweeped upwards till 90V. Courtesy: l'Université de Bourgogne,Dijon*

by monitoring the change in the temporal response of the sample to a 0-100V square signal voltage (0-25MV/m), modulated at low frequency (50mHz). The typical time response of the WRR output at its highest voltage sensitivity (green curve in Fig. 5.20) is displayed in Fig. 5.22. Note due to a different alignment of the experimental setup between measurements, the WRR output amplitude in Fig. 5.22 cannot be compared to Fig. 5.20. The rise time of I_{out} following the voltage step is in the range of 1.3s and was measured consistently over a series of devices. Fall times are typically shorter by 20-30%. This slow time response is clearly not in favor of an electro-optical effect where photonic devices containing the same DR1 molecules were reported operating at kHz range [102,103]. At this timescale the signal variation has to be attributed most likely to either thermal changes due to electrical leakage current or electrostriction effects. The measured residual current flowing between the electrodes was not exceeding 1nA for the largest voltage applied (100V). At this low current value, thermal effect can be neglected [16,104]. Electrostriction due to the volume contraction of the polymer when a DC voltage is applied, has been observed before [105]. Therefore, we believe that the

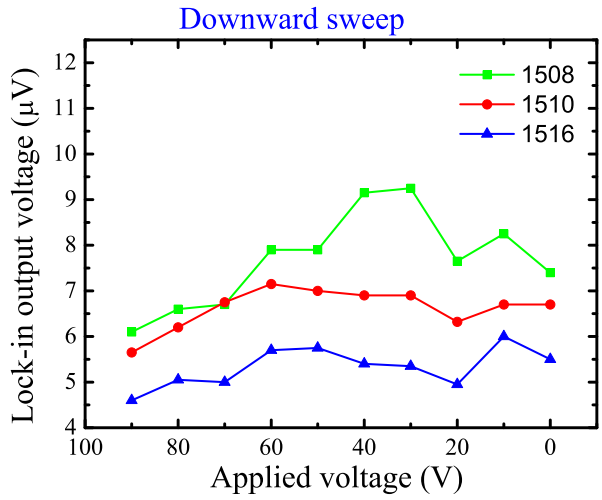

Figure 5.21: *Shows the evolution of transmission for each of the wavelengths as voltage is decreased from 90V to 0V. Courtesy: l'Université de Bourgogne,Dijon.*

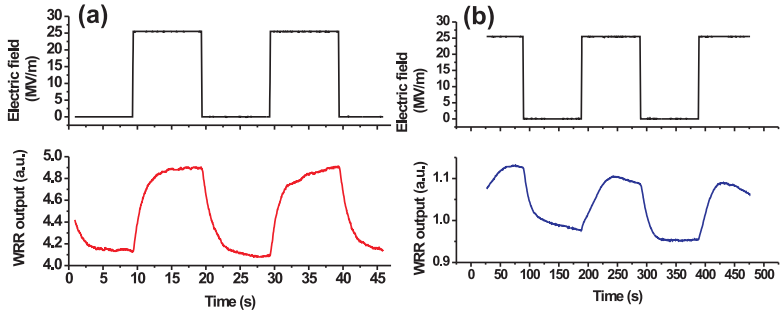

Figure 5.22: *(a) PMMA-DR1 WRR output response time for an electric field step of 25 MV/m.(b) Response of a WRR made of undoped PMMA.*

electrostrictive effects in PMMA play a dominating role in the variation of the WRR transmission.

To confirm this, undoped PMMA WRRs were fabricated on the electrode and the response dynamic was measured as shown in Fig. 5.22(b). To fully recover the response time, the voltage modulation was decrease to

5 mHz. While the variation depth is approximatively equal in doped and undoped WRR (15%), rise and fall times are ten times slower in undoped WRR. This indicates that the presence of DR1 molecules seems to accelerate the electrostrictive process given that the PMMA thickness for both cases is similar. The reason for this behavior could be due to the modified plasticity of the doped PMMA compared to the pure one. Also, because the kinetics is dominated by the slowest time response, one cannot completely rule out the existence of an electro-optical effect at a much faster time scale. The response time of the doped WRR can be a mixed contribution of electrostrictive and electrooptical effects. An hysteresis independent of the electric field polarity was systematically measured, most likely due to a fatigue caused by voltage stress. This kind of behavior tends to support the claim that the properties of electro-active DR1-PMMA plasmonic resonator is dominated by electrostriction effects responsible for a relative variation of the WRR output transmission.

5.5 Summary

Two different classes of electro-active materials were identified and evaluated in terms of their nonlinear coefficients, the origin of nonlinear behavior, material processing and nonlinear optical characterization. One belongs to the family of low T_g polymers which show high changes of the refractive index $10^{-2} - 10^{-3}$ without any poling required. The other was disperse red 1 (i.e. DR1) dye embedded in PMMA matrix showing smaller index changes $\Delta n \approx 10^{-4}$ and requires poling. However, the latter was finalized based on the deciding factor which has been compatibility to the fabrication procedures.

The electrode design, which is crucial for any successful EO device, was studied. Even though the vertical electrode geometry was favorable in terms of generating strong field in the polymer ring, but it was very difficult to implement in reality due to non-feasibility in terms of fabrication as well as contacting the electrode on top of the ring. As an alternative in-plane electrodes were used which involved fabrication of these electrodes before the WRRs were placed on top. The Au electrodes also support the SPP propagating on the Au/polymer interface. However, the electrostatic field within the electrodes is substantially lower as com-

pared to the vertical geometry contributing largely due to the stray field in the polymer. The electrodes were successfully fabricated and tested up to 100V without any problems indicating high robustness.

The active dielectric-loaded surface plasmon waveguide ring resonators was successfully characterized via LRM. By applying an electric field between the electrodes, the transmission of the WRR was in excess of 10%. By investigating the kinetics of the transmission when a stress voltage is applied, a response time of the order of a second was observed. This slow kinetics was attributed to a dominating electrostrictive effect directly affecting the geometry of the structure. Such effects should be considered seriously in future designs of electro-active plasmonic devices using similar configurations.

Chapter 6

Active II: All-optical Plasmonic Functionalities

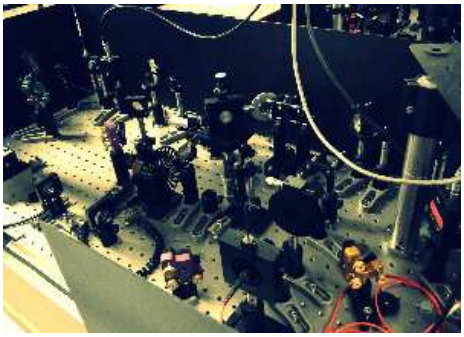

Beyond EO devices, all-optical devices in which the optical properties can be modified by a control light signal are important components of integrated optical communication systems. Nonlinear materials needed for implementing all-optical functionality often have trade-off between the achievable nonlinearities and the switching speed. Nevertheless even the slow nonlinearities are useful in applications where small footprint components can be realized to achieve optically programmable and reconfigurable photonic circuitry. Fully-functional integrated optical circuits which are capable of overcoming the fundamental diffraction limit require "active" plasmonic components capable of modulating and switching of SPP signals.

Different methods for controlling the propagation of SPP using all-optical control have been analyzed in the past and one common approach is based on the use of dielectric loads on top of the metallic layer and to alter the effective refraction index of the propagating SPPs. In order to achieve

this, the dielectric load must be made of an active material, the optical properties of which can be controlled via a pump light. On these lines, Pacifici et al. demonstrated an all optical modulator based interaction between SPPs in a thin layer of CdSe quantum dots (QDs) [14] and, Pala et al. with photochromic molecules [66]. Krasavin et al. proposed switching by controlling the structural phase of gallium at the interface with a gold film [106].

In this chapter we combine the use of two different and sensitive geometries for SPP and LSP respectively, with an active material for experimentally demonstrating optical control. For the control of a propagating SPP, we utilize a compact resonant plasmonic element based on a dielectric-loaded waveguide ring resonator (WRR) made from an active polymer. For modulating the LSP signal we use a plasmonic dimer configuration with gaps ranging from 10nm (narrow) to 200nm. The active polymer in both cases is realized by doping a host matrix, PMMA with disperse red 1 (DR1) molecules, which provide large changes of the refractive index due to the trans-cis isomerization when pumped with light near the absorption resonance.

The chapter starts with discussing the properties of trans-cis isomerization and resulting photo-orientation of the azobenzene molecules. Changes in refractive index due to this phenomenon were measured to be as high as $\Delta n \approx 10^{-3}$ using a pump-probe method with cross polarized scheme. Next, this active dielectric polymer was patterned on top of a planar Au film to produce sensitive plasmonic ring resonators with high quality factors. Transmission changes of almost a factor of three under milliwatt ($\approx 100\text{W/cm}^2$ by intensity) control powers is demonstrated via near-field microscopy setup (Experimental characterization was done at Prof. Zayats group at King's college, London). Finally, ideas and challenges related to the characterization of dimers spin-coated with the active polymer are discussed.

6.1 Photo-orientation with DR1

Since the backbone of modern communication is optical, and some of the materials required for the related devices are exploiting photochem-

ical phenomena, different types of chromophores have been investigated for a variety of applications, such as lithography, nonlinear optical devices, all-optical switches, and even data storage. The azobenzene class of chromophores is characterized by the azo linkage (- N = N -) that bridges two phenyl rings. This extended aromatic structure gives rise to azobenzene's intense optical absorption and related optical properties. Most of the azobenzene molecules (azos) can undergo an efficient photochemical isomerization that can occur when the chromophore absorbs a photon. The two states are a thermally stable trans-, and a meta-stable cis-configuration. Light anywhere within the broad trans-azo absorption band will elicit photochemical isomerization (with high quantum efficiency near the $\lambda_{\max}$). The cis-configuration will then typically relax photoinduced or thermally back to the trans state with a lifetime that depends sensitively upon the particular azo's substitution pattern, as well as on local conditions [107]. Irradiation of the cis-form with light within its (possibly distinct) absorption band can also elicit the photochemical cis-to-trans isomerization. More detailed description is given in the upcoming paragraphs.

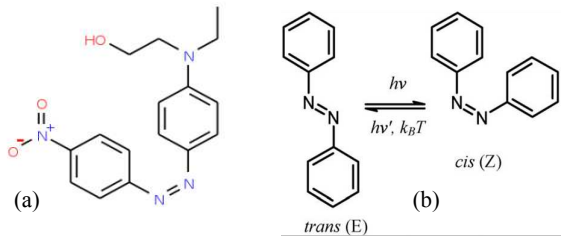

Figure 6.1: *(a) Chemical structure of disperse-red 1 (DR1) which belongs to the pseudo-stilbenes type of azobenzenes.(b) The trans-to-cis-conversion in azobenzene takes place photoinduced. The reverse conversion to the stable trans-state is triggered thermally or photoinduced. Alternatively, the cis-to-trans-conversion can be effectuated with a distinct wavelength of light.*

There are different classes of azobenzenes but we are mainly interested in the pseudo-stilbenes as they exhibit the best photo-switching response. This makes them ideal candidates for a variety of applications. They are

characterized by a strongly asymmetric electron distribution, which result in having a push-pull donor (electron-donating) and acceptor (electron-withdrawing) groups on the opposite side of the benzene rings (called a 'push/pull' substitution pattern) as shown in Fig. 6.1(a). The pseudo-stilbenes possess a strong and broad absorption feature throughout the visible, have non-linear optical properties owing to the asymmetric electron distribution. For instance, the dipole of the pseudo-stilbenes can be oriented in an electric field, and the higher order moments of the electron distribution give rise to a significant non-linear response as for disperse-red 1 (DR1), a commercially available pseudo-stilbene, also used for the electro-optical control of SPP in Chapter 5.

In case of all-optical control of DR1, absorption of light at frequencies near the trans-absorption resonance causes the molecule to change from the trans-to the cis-configuration. This isomerization process is a photo-induced molecular motion as it involves rotation or inversion about the azo-bond, with twisting of the phenyl rings [107]. During this process the distance between the two carbon atoms is drastically reduced (from 0.99nm in trans-state to 0.55nm in cis-state) and the molecule's dipole moment as well as the material polarizability undergoes a substantial change (see Fig. 6.1(b)) leading to dramatic changes in the material refractive index. This provides large negative nonlinearity on the order of 10^{-8}cm^2/W to 10^{-11}cm^2/W. Due to a good overlap between trans- and cis-absorption spectra [108], the pump light also initiates the reverse isomerization process accompanied in addition by the thermal cis-trans relaxation [109]. All of these causes the molecules to oscillate between the trans-and cis-states under pump illumination [107, 110]. Since the absorption probability for the trans-DR1 is much higher for molecules which are predominantly parallel to the pump polarization, the isomerization will result in depletion of population of such molecules, producing light-induced anisotropy. Additionally, over longer pumping times, the trans-cis-trans isomerization cycling leads to the statistical photo-orientation of the DR1 molecules perpendicular to the polarization of the pump light as shown in (Fig. 6.2), which produces another, slower, mechanism for light-induced anisotropy [107, 110, 111].

In this photo-orientation process, an azo molecule preferentially absorbs light polarized along its transition dipole axis (long axis of the molecule)

where the probability of photon absorption varies as $\cos^2\varphi$, where φ is the angle between the light polarization and the azo dipole axis. Azos oriented along the polarization will absorb light with high probability, whereas those oriented at 90° to the incident polarization will absorb far less light. Each time a chromophore undergoes a trans-to-cis-to-trans isomerization cycle, its position will vary in a small way. Thus, starting from an initial uniform angular distribution of chromophores, those that lie along the polarization direction will absorb and reorient, resulting in a statistical depletion of the population of chromophores oriented in the polarization direction, also giving rise to a strong birefringence in the material. The photo-orientation is reversible: isotropy can be restored using circularly polarized light, or a new orientation direction can be selected by irradiation with a different polarization.

Azobenzene photo-isomerization and light-induced birefringence occurs at a wide time range, starting with seconds [108, 110], and also reaching the picosecond range [112]. This depends on various factors, including the type of azobenzene, the environment surrounding, the pumping wavelength and power. In the absence of radiation, the cis-isomer thermally decays to the trans-isomer. The birefringence relaxation ranges from minutes to milliseconds [108, 109, 111, 113]. In some cases, illumination with unpolarized white light is needed to restore random distribution of DR1 molecules [114]. Overall, the light-induced birefringence, the on-and off-times essentially depend on which of the two initiating mechanisms is dominant.

6.1.1 Study of Trans-cis Isomerization in DR1-PMMA Composites

In this section the isomerization in planar DR1-PMMA composite films upon irradiation by pump light near the main absorption band ($\lambda = 520nm$) is studied. A single pump and probe setup was used for characterizing these films, providing a useful reference for understanding and observing the isomerization and photo-orientation of the chromophores when doped in a host material such as PMMA. The change of the refractive index due to the isomerization with respect to different setup parameters such as varying pump powers was studied. Also, different

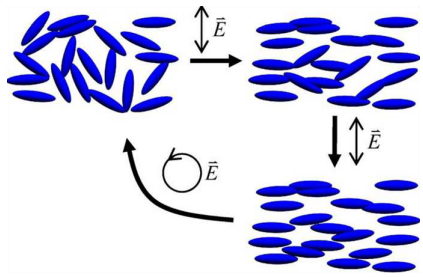

Figure 6.2: *When irradiated with polarized light, an initially isotropic distribution of chromophores will become progressively aligned after repeated isomerizations. Photo-isomerization is reversible process and irradiation with circularly polarized light can restore isotropy. This Figure is reproduced from Yager et al. [107]*

concentrations of DR1 molecules in PMMA were tested in order to optimize the maximum refractive index change. Next, we discuss the composite material processing techniques used in order to obtain homogenous and good quality films.

6.1.1.1 Preparation of DR1/PMMA Layers

Thin films of nonlinear DR1/PMMA composite were fabricated in the following way. DR1 and PMMA were separately mixed in chlorobenzene and left stirring overnight. Later, DR1 was filtered and mixed into different weight percentages into PMMA, e.g. 0.1-20%. Different concentrations were tested in order to determine the most appropriate for observing strong nonlinear response and 1% was determined to be the optimum. Layers of DR1/PMMA composites were made by spincoating layers of thickness d = 440nm on BK7 glass substrate (0.5mm thick) and then baking at 65°C for 4hours in an oven and left overnight at room temperature for all solvent to evaporate.

6.1.1.2 Pump-Probe Setup

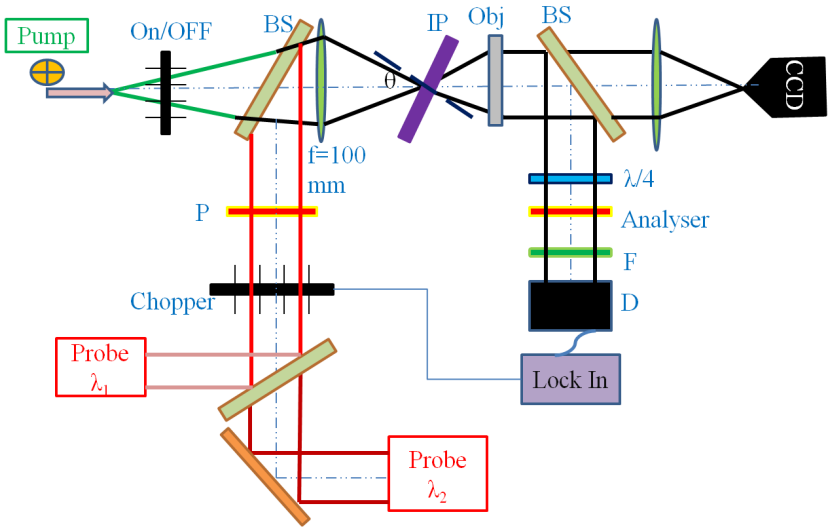

Figure 6.3: *Experimental pump-probe set-up for measurement of optical switching effect: BS, beam splitter; F, filter; f, lens; D, detector; P, polarizer. The setup is modified to include two laser probe sources at* $\lambda_1 = 633nm$ *and* $\lambda_2 = 700nm$ *and a CCD camera for imaging the areas containing dimers.*

Optically-induced refractive index change in the composite DR1/PMMA films was estimated in pump-probe experiments. As shown in Fig. 6.3, a beam of linearly polarized pump laser ($\lambda_{\text{pump}} = 532\text{nm}$) focussed onto the sample caused trans-cis isomerization of DR1 molecules accompanied by their reorientation perpendicular to the polarization direction, which modulated the relative phase between p- and s-components of the probe laser ($\lambda_{\text{probe}} = 633\text{nm}$). The latter was monitored as a change in the probe transmission power for the sample placed between two crossed polarizers [99]. The sample was placed at an angle $\theta = 45°$ with respect to the optical axis.

If the polarizer and analyzer are considered tilted with an angle θ with respect to the optical axis, for a linearly polarized beam transmitted through the sample, the effective indices of refraction for the s- and p-polarization components are given the effective index of refraction n_p

by:

$$\frac{1}{n_p^2} = \frac{\cos^2\theta}{n_0^2} + \frac{\sin^2\theta}{n_e^2} \tag{6.1}$$

where n_o and n_e are the ordinary and extraordinary indices of refraction, respectively. The phase difference between the two polarization components, after passing through the sample is given by:

$$\delta = \frac{\pi d}{\lambda \cos\varphi}\Delta n \tag{6.2}$$

where d is the sample thickness and λ is the probe wavelength. This phase change was monitored as a change in the signal transmission power with the sample placed between two crossed polarizers, and connected to a lock-in amplifier for sensitive detection, for which the probe beam is chopped at an appropriate frequency. To introduce a constant retardance phase σ that allows the transmitted power to be adjusted to a desired value, a waveplate is placed before the analyzer. Typically, the working point (I_c) is selected to be half of the maximal optical intensity (I_0). For this case, the transmitted power across the polarizer-analyzer or the optical intensity of the light after interference can be written as:

$$I_c = 2I_0 \sin^2\frac{\delta}{2} \tag{6.3}$$

From the measured intensity values, Δn can be calculated from the above equations. This setup allows us to observe the orientation at the molecular level and its effect on the phase of the probe beam by monitoring its transmission through a straightforward technique.

6.1.1.3 Refractive Index Change- Measurements

The dynamic modulation of the refractive index change derived from the transmission data at the above described setup is presented in Fig. 6.4. The dip in the transmission corresponds to the pump ON which triggers the isomerization in the DR1-PMMA composite films and hence, cause changes of index (Δn).

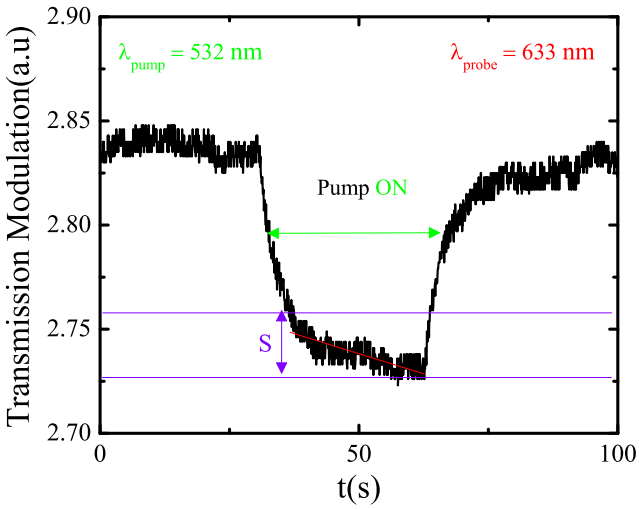

Figure 6.4: *The figure shows the modulation dynamics for 110 mW pump power and a probe wavelength of $\lambda = 633nm$, the duration of the pump is marked by green line. The slope S indicates a second decay on a slower timescale.*

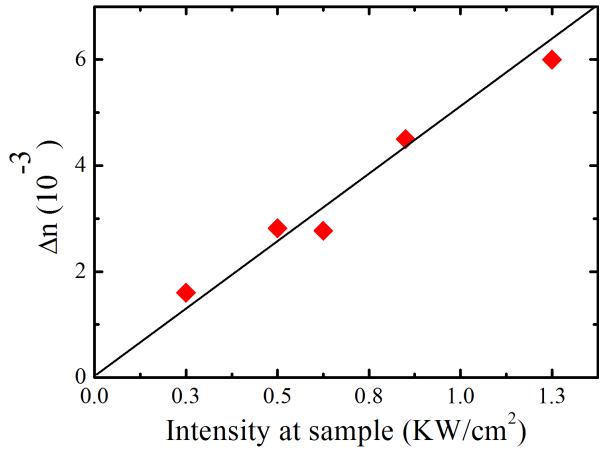

Figure 6.5: *Modulation of the refractive index of a 440nm thick PMMA/DR1 film by pump light.*

The role of the pump power on the isomerization was investigated and the resulting Δn changes obtained from the dynamics at various pump

powers is presented in Fig. 6.5. The optically induced refractive index change increases linearly with the pump power with the absolute values reaching as much as 6×10^{-3}, indicating larger optically-induced molecular changes at higher pump powers with no observed saturation. Such large changes in Δn are more than sufficient for significant modulation of SPP mode transmission through the WRR component (Fig. 4.3(b)). Furthermore, the change is most likely induced through optical nonlinearity, and not thermally, since pure PMMA films did not show the effect of such scale. The observed on- and off-times are in agreement with previous observations [108–110]. Furthermore, the timescale of the processes and complete reversibility of the change suggests the angular hole mechanism for photoinduced birefringence.

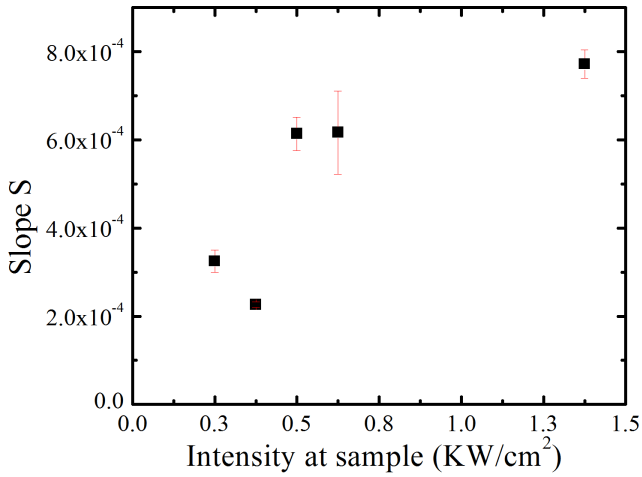

Figure 6.6: *Variation of the slope S with increasing pump Power.*

An analysis of the modulation dynamics is shown in Fig. 6.4, where the slope of the dip, S, indicates two mechanisms taking place. S indicates a further change in the orientation of the DR1 molecules on a much slower timescale. Moreover, Fig. 6.6 shows that S doubles when the pump intensity is increased from 0.3 to 1.3KW/cm^2, showing a saturation tendency for higher powers. This could maybe attributed to the thermal effects.

6.2 All-optical Active Dielectric-loaded Waveguides

Using the approach described in the previous sections, a compact and efficient active plasmonics component for dielectric-loaded SPP waveguides at telecom wavelengths was demonstrated. In order to utilize the large changes in refractive index due to the isomerization in DR1-PMMA, the WRR configuration was fabricated out of this material.

Finite element method (FEM) numerical simulations as presented in previous chapters show that by optimizing the WRR design (defined by the parameters ring radius R, and Ring-to-waveguide separation g), 100% modulation contrast with the wavelength can be achieved. If the refractive index of of the ring material, n, is changed by an external signal (either optical or electric), the effective index of the ring mode is modified and the resonance is shifted. As mentioned before, due to high sensitivity of the WRR component, changes of $\Delta n \approx 10^{-3}$ are sufficient to significantly switch/modulate the mode transmission (but not 100%).

Next, details of the fabrication of these active components and the subsequent characterization via near field microscopy is discussed.

6.2.0.4 Fabrication

To fabricate nonlinear WRR components, an PMMA/DR1 film was deposited in a similar way (as described in previous sections) onto a 65nm gold film. The components were patterned using electron beam lithography and then chemically developed. The ring was implemented in a form of racetrack to enlarge the coupling length (L_c = 1, 2 and 3μm). This increases the waveguide-ring edge-to-edge gap to the value of 500nm and thus improve the reliability of fabrication process. The ring radius R was chosen to be 5μm. Figure 6.8 shows brightfield microscopy images of the fabricated racetrack resonators for varying L = 1, 2 and 3μm.

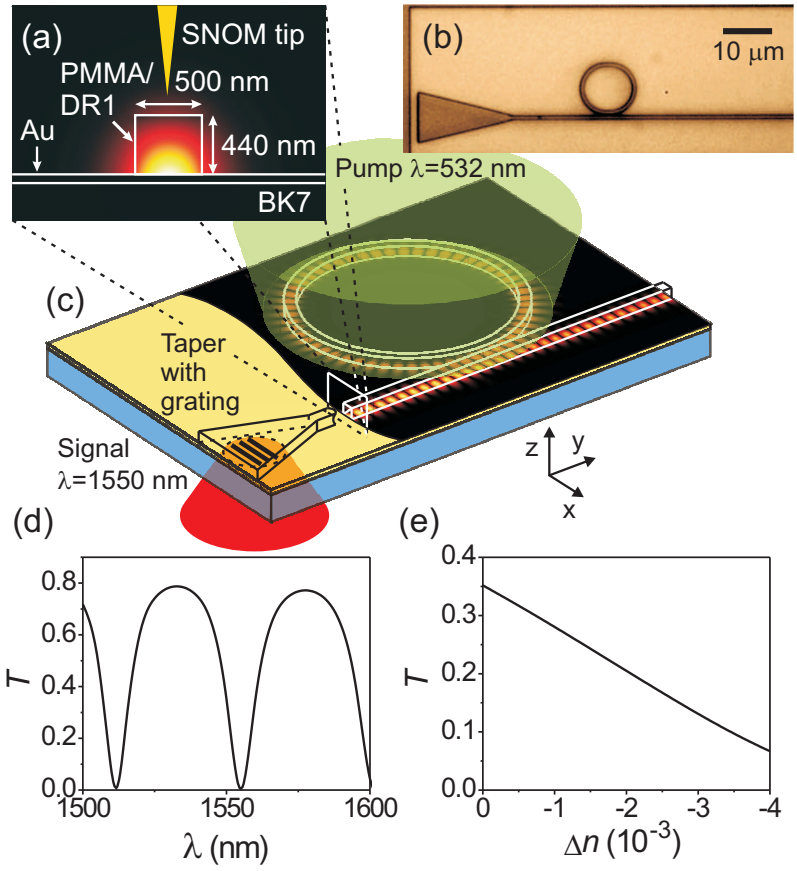

Figure 6.7: *(a) Cross-section of the 440 by 500nm^2 WRR waveguide with P_y power flow profile of the fundamental TM_{00} SPP mode in it. (b) Microscope image of a DR1/PMMA ring resonator component. (c) Sketch of the experimental setup along with the calculated $|Re(E_z)|$ cross-section of the SPP mode 10 nm above the metal interface.(a),(c) Courtesy of A. Krasavin, King's college.*

6.2.0.5 Characterization with Near-field Microscopy

The transmission of the DLSPPW mode through racetrack WRRs was investigated using SNOM operating in the tapping mode [115]. The 1550nm light from a laser diode was mechanically modulated and focused

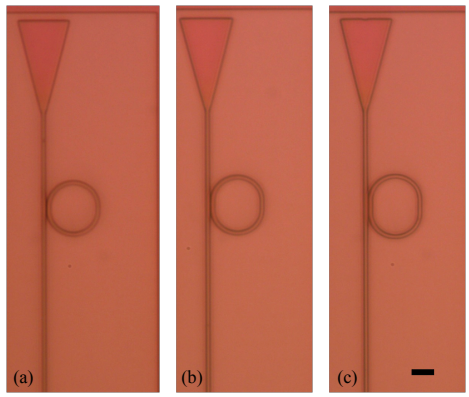

Figure 6.8: *Brightfield microscopy images of three different kinds of racetrack resonators fabricated on DR1/PMMA composite on Au film of 50 nm. (a) L = 1μm (b) L = 2μm and (c) L = 3μm. Scalebar is 5μm*

on the slit grating at the tapered waveguide region (Fig. 6.7(c)) using an ultrazoom objective system equipped with IR/visible camera. The slit grating was fabricated using an focused ion beam to supply the necessary momentum and launch the SPP wave. The near-field image of the SPP mode propagation was mapped by a metal-coated nanoaperture optical fibre. The signal from the fibre was detected by a femtowatt photoreceiver and sent to a lock-in amplifier, having a frequency reference from the chopper controller.

A typical near-field map along with the topography of the sample is presented in Fig. 6.9(b) and (a) respectively. The SPP wave generated by the slit grating propagates along the funnel, being adiabatically focused in the DLSPP waveguide. At the funnel region on the near field image a characteristic SPP interference pattern can be noticed, which has been observed before in both numerical simulations and in nearfield studies [83]. To the left of the funnel one can observe an SPP wave propagating at the gold/air interface corresponding to SPPs escaping the funnel. Further, a reflection of this wave from the ring can be observed. After focusing in the waveguide, the SPP mode propagates along it, being partially coupled to the ring mode in the region adjacent to the ring. It can be seen that the mode in the ring partly gradually escapes from the racetrack, producing a glow of light above it and a characteristic

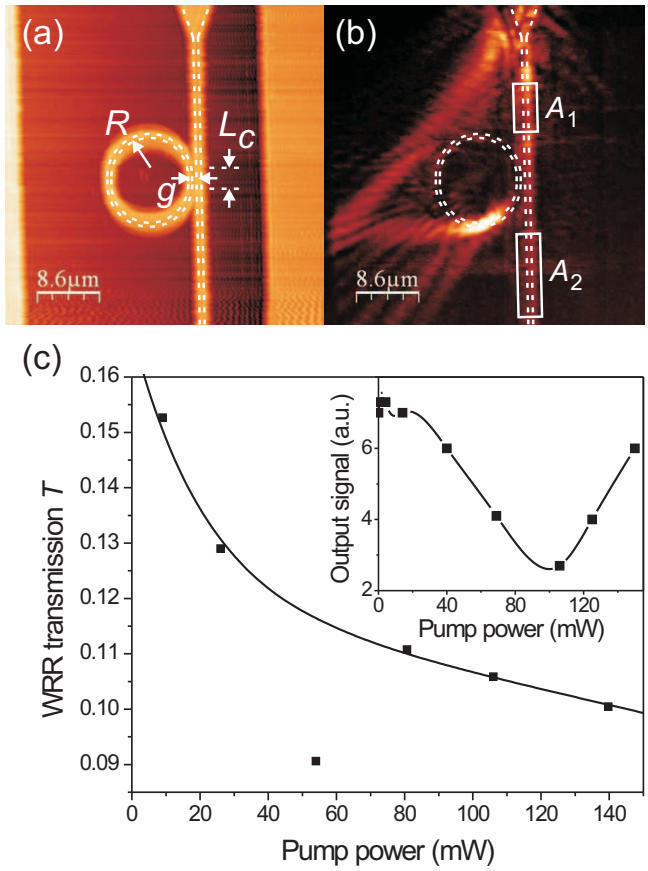

Figure 6.9: *(a) Topographical and (b) near-field images of SPP mode transmission through a racetrack resonator. (c) The SPP mode transmission through the WRR component as a function of the pump power derived from near-field images (e.g. (b)). The line is to guide the eye only. The inset represents the WRR transmission signal measured by a SNOM tip placed at the WRR output (see text for details).*

SPP wave interference pattern in the area outside the ring. The intensity of the escaped light is greatly exaggerated in respect to the intensity of the mode, because it is directly collected by the SNOM tip, while the intensity of the DLSPPW mode is collected from the small evanescent field on the top of the waveguide (Fig. 6.7(a)). The indirect confirmation

that the mode in the ring exists along the whole its length is that the interference produced by the escaped SPP waves can be observed in the outer area all around the ring.

To study an all-optical modulation of the SPP mode transmission a pump laser beam from $\lambda = 532$nm laser diode was weakly focused (diameter of the spot ≈ 0.1mm onto the WRR region (Fig. 6.7(c)) and consequent SNOM images at various pump powers were acquired. For each pump power the transmission was calculated as the ratio between the SPP intensities averaged over waveguide areas A_1 and A_2, before and after the ring region correspondingly (Fig. 6.9(b)). The resulting dependence of the WRR transmission on the pump power is presented in Fig. 6.7(c). The transmission is essentially decreased as the structure is pumped, which happens when the initial transmission point is on the increasing region of the WRR wavelength characteristic. Initially the transmission decrease is linear, then it saturates, which can be due to achieving the minimum transmission point for WRR or due to saturation of the refractive index change in DR1/PMMA composite. Finally, it is noted that the decreasing nature of the WRR transmission rules out the possibility of the transmission change due to the detection of pump light coupled into the waveguide. Also, a more dynamic approach of monitoring the SPP modulation is used for another WRR component. The SNOM probe was positioned at the output end of the waveguide where the SPP mode is decoupled into free-space photons. The collected signal was studied as a function of the pump power (inset to Fig. 6.9(c)). Apparently, due to a different transmission curve (slightly different radius of the ring inside the fabrication uncertainties) the probe wavelength was closer to the minimum transmission and by changing the pump power, the resonance could be scanned through.

In both experiments a strong modulation of the transmission signal of the WRR was observed. Even for low pump powers of 20mW a significant change in WRR transmission of more than 20% is achieved. The relative transmission change is almost doubled up to $\approx 40\%$ as the pump power reaches 140mW. Although performance of such component is limited by the relaxation timescale [$\mathcal{O}$(milli-seconds)], the large optically controlled change in the SPP mode transmission, makes it a promising tool for active plasmonics circuitry.

In conclusion, an efficient all-optical active plasmonics component is demonstrated on the basis of a waveguide ring resonator. Large nonlinear effect in PMMA/DR1 waveguide material based on trans-cis isomerization led to refractive index changes up to 4×10^{-3}. Combined with highly resonant nature of WRR transmission, this results in a prominent SPP switching effect at milliwatt pumping power.

6.3 All-optical Response of Gold Dimers

Localized surface plasmons (LSP) are charge density oscillations confined to metallic nanoparticles. LSPs result in an enhancement of its scattering and absorption. These resonances are governed by the type of metal and are highly sensitive to the shape, size, and the surrounding media. Through the precise control of these properties due recent advances in synthesis and lithographic techniques, LSPs can be tuned over the entire visible spectral range. On the one hand they have gained tremendous interest due to their ability to concentrate light down to the nano-scale in the so called hot spots. On the other hand the sensitivity of LSP resonance to their surrounding make them very attractive for sensing and active plasmonic devices.

The sensitivity of the LSPs is determined by both the spectral features of the plasmon resonance and the spatial distribution of the associated mode. For designing active plasmonic components, the resonance bandwidth plays an important role. Sharp narrow resonances having high quality factors Q, make it easier to resolve the effect of a small change of surrounding. However, due to the strong absorption in the metals at visible frequencies, the resonances are typically rather broad but by coupling two (Dimers) or more metallic nanoparticles one can achieve sharp spectral features. Moreover, this coupling between closely spaced nanoparticles creates a strong field confinement within the subwavelength gap due to the *near-field* interaction and leads to a shift in the resonance which can be understood by a simple dipole-dipole interaction model [116]. Due to the electric field of the incident light, there is a strong accumulation of surface charges in the gap that leads to a strong electromagnetic field. There also exists *far-field* interaction effects which have been reported when the grating constant of the particle arrangement pattern exceeds

the wavelength of the interacting light [116]. However, in this work the grating constant is kept to be 400nm.

In this experiment the sensitive nature of the near-field coupling in dimers is utilized. For dimers with very small gap sizes, its is possible to achieve a significant shift as the magnitude of the shift is dependent on the perturbation induced by the local change of the refraction index to the mode volume. Dimers made of gold (Au) with thickness $\approx$ 40nm and size $\approx$ 100nm and varying gap sizes are embedded in DR1/PMMA. When optical pump shines on the areas containing dimers, the refractive index of the dimer environment is significantly altered due to the isomerization of DR1 molecules. The response of the dimers for a wavelength in the resonance band is studied for different dimers of different gap sizes.

6.3.0.6 Fabrication

The samples were fabricated in the following way: 40nm thick gold was thermally evaporated in high vacuum onto cleaned glass substrates. Then a 60nm-thick negative resist (AR-N 7500.08, Allresist, Germany) was spin-coated onto the gold layer. A pre-exposure bake was done at 85°C on the hotplate for 1minute. 100μm $\times$ 100μm areas containing dimers of different gap sizes were patterned via e-beam lithography at 30kV. The variation in gaps sizes extended from overlapping ones and 0nm (touching case) to gaps of about 5-200nm and the period was kept to be 400nm. After exposure, samples were developed in an AR 300-47 developer and DI water mixture (4:1) for a three minutes. The formation of masking nanostructures was confirmed by an optical microscope, followed by a pre-etching baking of the resist in the oven for 1hour at 130°C. The desired nanopatterns are transferred to the underlying gold layer by reactive ion etching (PlasmaLab 100, Oxford Instruments). The unprotected gold layer was removed in argon plasma by directional Ar ion bombardment. After removing the unprotected gold, the remaining resist was etched away by isotropic etching in mild oxygen plasma. This process was developed previously within the plasmon nano-optics group for making dimers for sensing purposes [31].

Subsequently the DR1-PMMA solution (1wt%) prepared in a similar

manner as described in previous sections was spin-coated onto the dimers. The thickness of the polymer was measured to be ≈ 466nm and was baked at 65°C for 4hours in an oven and left overnight at room temperature for all solvent to evaporate.

6.3.0.7 Pump-Probe Measurements

The pump-probe setup was modified for measuring the response of small sample areas containing nanostructures as shown in Fig. 6.3. The light transmitted through the sample is collected by an objective. The collected light passes through a beam splitter where a part is collected via the detector and another part is transmitted to the lens which focuses the beam onto a CCD camera for imaging of the dimer areas. A notch filter filters out the pump beam before the probe hits the detector which was connected to a lock-in for sensitive detection.

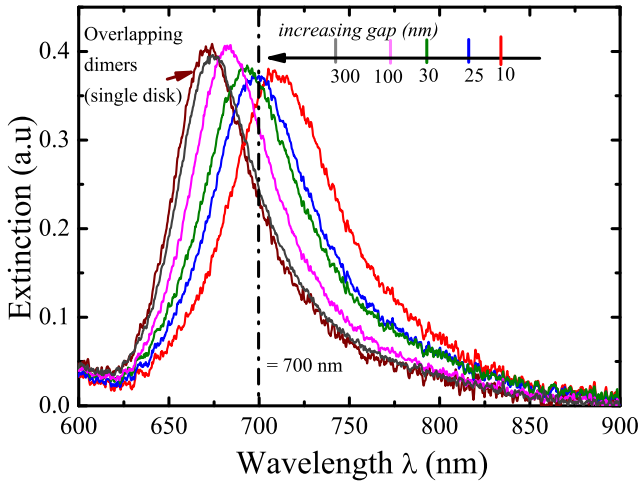

Figure 6.10: *Extinction spectra of dimers with different gaps.*

Figure 6.10 shows extinction ($-log(Transmission)$) spectra for the fabricated arrays of different gap sizes when probed by extinction spectroscopy which was used not only to measure their resonance properties but also to assess the gap size. The extinction through different areas was measured, with a complete range of gap sizes, ranging from separated metallic

nanoparticles (gap >100nm) to fused dimers. After spincoating the fabricated dimers with DR1-PMMA solution ($n \approx 1.5$) the resonance shows a huge red-shift with the peaks for different dimers (made of gold) lying close to 700nm (Fig. 6.10). Therefore, another probe at $\lambda = 700$nm was added and its path was superimposed with the probe at $\lambda = 633$nm. The change of refractive index is the highest for wavelengths close to the main absorption band where the absorption losses are also usually high. And as we spectrally move further away from the main absorption band, the effect on index change also slightly decreases. Also, slightly different dynamic modulation for $\lambda = 700$nm is observed as shown in (Fig. 6.11). The sign of change in refractive index, Δn, leads to a peak in transmission instead of a dip (as compared with 633nm).

For the pump-probe measurements, the transmission at the probe wavelength (chopped at a frequency of 1KHz) through the areas containing dimers was measured via lock-in detection. The pump was modulated ON/OFF at regular intervals of time (every 5th and 15th second) for a duration of 5s as shown in Fig. 6.11. But due to the varied absorption for different dimers areas and the sensitivity of modulation to the inhomogeneity of the spincoated DR1/PMMA layer, the data obtained could not be compared and the sensitivity of the dimers with narrow gaps could not be justified as expected before. Since the trans-cis isomerization causes an index change in the entire surrounding areas and not just within the gap, the contribution of index change throughout the surrounding media was thought to be more dominating than the index change within the dimer gap. The latter is responsible for the modification of the near-field distribution of the plasmonic mode associated with the dimers and the subsequent shift of the resonance in the far-field. But since the modulation cannot be normalized with respect to the reference signal, due to the absorption by metallic nanoparticles, it was not possible to distinguish the enhanced contribution of isomerization of thick DR1/PMMA layer to the coupled plasmonic resonances. Moreover, the dimer peaks could only be partially excited due to the oblique angle of incidence at 45°.

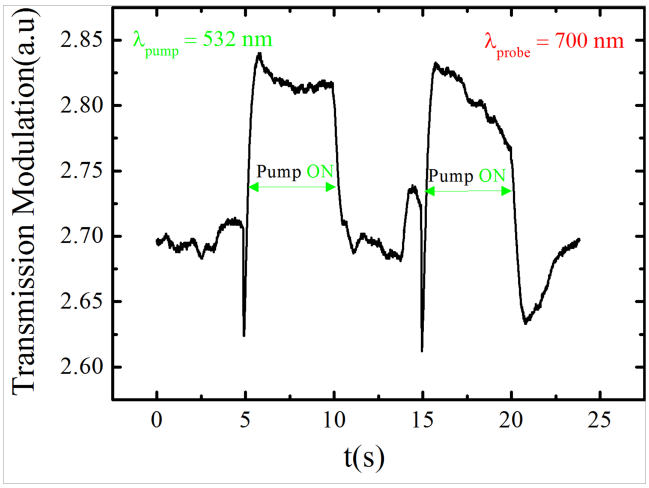

Figure 6.11: *Modulation dynamics for probe at $\lambda = 700nm$ shows a peak in transmission when the pump is ON.*

6.4 Summary

In conclusion, a highly efficient nonlinear plasmonic component on the basis of waveguide ring resonator device has been demonstrated. The large nonlinear effect in PMMA/DR1 waveguide material based on trans-cis isomerization led to refractive index changes up to 4×10^{-3}. These changes could be observed based on the transmission through a cross polarized scheme. The large change in refractive index combined with highly resonant nature of WRR transmission, resulted in the reversible transmission changes by almost a factor of 4 between high and low transmission states at milliwatt ($\approx 100\text{W/cm}^2$) control powers. Such components could be used for optically reconfigurable and programmable plasmonic circuitry.

The effect of the change in refractive index in a dielectric coated on top of dimers with varying gap sizes was also studied. But the response originating form the gap between the dimers could not be resolved in the far field due to the dominating bulk effect of the thick DR1/PMMA layers.

Chapter 7

Active III: Hybrid Plasmonic Nanoresonators

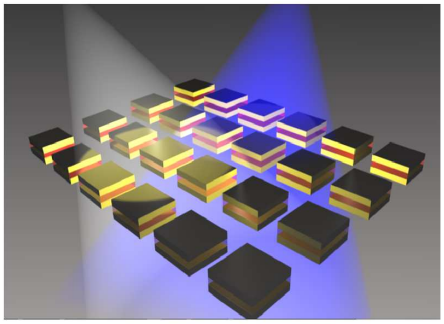

Beyond the active control of propagating surface plasmons, further advancement can be achieved by means of 3D nanoscale plasmonic structures supporting LSP. Optical radiation in these plasmonic nanostructures take the form of intense, localized electric field distributions. These highly confined optical fields provide an exciting opportunity to study the enhanced light-matter interactions at the nanoscale. A step forward in the control towards active nanoscale functionalities can potentially be accomplished in hybrid plasmonic components, which combine the use of active organics and metallic nanostructures. Insights into the hybrid interactions on the ultrafast timescales pave way towards understanding the different competing processes and possibly novel phenomena that arises as a result of hybridization. Additionally, plasmonic nanostructures due to their fast temporal responses (femtoseconds to picoseconds) make attractive candidates for ultrafast applications.

One such attractive configuration is the metal-insulator (dielectric)-metal

(MIM) type. A MIM structure consists of a sandwich of metal-dielectic-metal layers which can sustain SPPs. In fact, when the dielectric layer becomes very thin, SPPs from each metal-dielectric interface couple with each other, and generate SPP modes with a higher wave vector. The propagation distance of the SPP mode is typically very short, but provides a very strong field confinement in the dielectric layer, whose lateral extent is limited to only tens of nanometres. MIM geometries might not have attracted attention as transmission lines due to their limited propagation lengths, but they are attractive in terms of the larger wave vectors supported by them. Scaling down from extended MIM films supporting SPPs to MIM nano-sized cavities supporting LSPs, enables the realization of stronger confinement. These cavities have smaller mode volumes as compared to dielectric cavities, on the order of $\lambda/4$.

The confinement of MIM plasmons in resonator structures is a relatively unexplored area. There have been experimental demonstrations in the past of single MIM nanostructures. Miyazaki et al. [117] have shown cavity resonators in MIM waveguides of finite lengths, and more recently Kuttge et al. [118] have studied the modes in MIM disk resonators using cathodoluminescence imaging spectroscopy. But all these have been demonstrations of *passive* MIM cavities. (Moreover, a dimer configuration can also be considered as an asymmetric MIM configuration, and has been popular in the plasmonic community for either achieving enhancement of Raman signals, or for biosensing applications [31].) From these, it can be expected that in these geometries, the advantage of the strong energy confinement of MIM cavities outweighs the disadvantage of losses due to heating in the metal.

This work extends the concept of *passive* MIM cavities by integrating an active polymer in the MIM cavity, and creating an array of such hybridized cavities, that we coined as *mini-MIMs*. The focus of this work is on controlling the resonance features of such these hybrid cavities on an ultrafast scale and not on controlling the SPP propagation. The active polymer in this case is a π-conjugated poly(p-phenylenevinylene)(PPV) layer, which shows higher state excitation when pumped optically, and thereafter creates bound electron-hole polaron pairs. The interaction of such molecular excitations with plasmonic polarizations is investigated using ultrafast transient absorption spectroscopy, which allows for the

observation in 'real time'. Moreover, the pi-conjugatiobn in PPV is a crucial factor in attaining high optical nonlinearities, and indeed, PPV and its derivatives have been considered for applications in all-optical switching of optical signals at relatively low light intensities due to their high value of the nonlinear refractive index, n_2, or alternatively value of the third-order susceptibility, χ^3. Numerous studies reported the χ^3 values of PPV reaching 10^{-9} esu (about 10^{-17} m^2/V^2) for wavelengths $\approx 1.3\mu$m [119, 120]. With these high nonlinearities one can expect that even thin films may produce strong third-order nonlinear optical effects. In this case, the pump drives a nonlinear change in the polymer core whereas the probe feels the altered optical response of the system, which is the result of enhanced sensitivity of the mini-MIM resonance to the changes in the polymer, located at the "hot spot" of these nanostructures. As a result, strong spectral shifts in the mini-MIM transient signature accompanied by novel phenomenon of narrowing of the transient signal at early times is observed.

This project was supported by the BE-AGAUR scholarship for a research stint abroad for a period of 6 months and was done at the Centre for Nanoscale Materials (CNM) at Argonne National Laboratories, USA, in collaboration with Dr. Gary Wiederrecht. The samples were fabricated and characterized at CNM. The FMMDVL simulations were done using a code developed by Dr. Stefan Enoch (Institut Fresnel, Marseille), whereas the electromagnetic field maps were provided by Dr. Jan Renger. The reactive ion etching for patterned samples was done at ICFO by Dr. Jan Renger. The preparation of the PPV precursor solution and PPV layer was performed by Dr. Xavier Elias Pera and Rafael Betancur respectively at ICFO.

7.1 MiniMIMs: Design and Properties

The SPP dispersion relation (given by Eq. 2.3) for a dielectric on top of a semi-infinite homogenous metal has already been discussed in Chapter 2. For more complex geometries (multilayers, corrugations, etc.), an analytical expression for the dispersion relation is difficult to obtain and could be calculated numerically as shown in Fig. 7.1 for the case of an extended MIM system. Also, later in this work the optical modes sus-

tained by an array of MIM nanostructures was analyzed, a schematic for which is shown in Fig. 7.2(a).

In this work, we have employed a Fourier Modal Method (FMM) [69,70] to compute the dispersion relations of surface plasmon modes existing for multilayered metal-dielectric-metal planar films and nanostructured arrays. An extended MIM structure as shown in Fig. 7.1 consists of a sandwich of metal-dielectric-metal layers which can sustain SPPs. The metal (Au in this case) is infinite in both directions and the dielectric is assumed to have a constant refractive index $n = 1.6$.

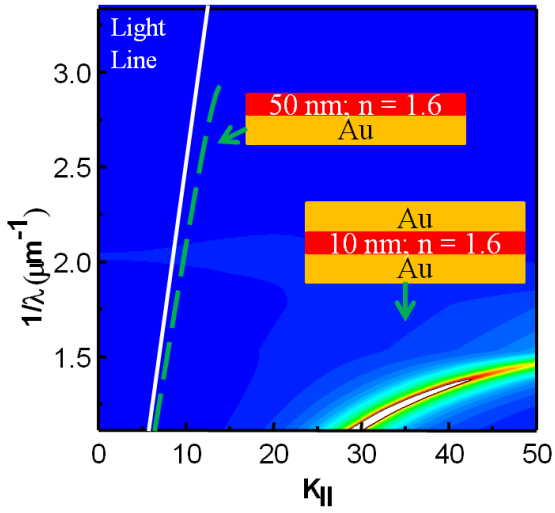

Figure 7.1: *Dispersion relation calculated using Fourier modal method (FMM) method for the antisymmetric MIM mode supported by planar films Au and polymer with refractive index n = 1.6 in between. The top and bottom Au layers extend infinitely above the polymer.*

Typically, the surface plasmon coupling between two close metal/dielectric interfaces causes the splitting of the SPP mode into two modes, ones with high and low energy. The high energy modes are not taken into account here. Fig. 7.1 shows the dispersion relation calculated for a 10nm thick

dielectric layer in a geometry as shown in the inset. As can be seen in the figure, the MIM modes for planar films lie far beyond the light line having larger wave vectors. As the thickness of the dielectric in between is increased the modes appear at smaller wave vectors close to the light line. Larger wave vectors make it possible to realize smaller cavities.

If instead of planar metal-dielectric-metal layered system, we truncate the layers in both X- and Y-directions to convert it into a three-dimensional resonator, as depicted in Fig. 7.2, we confine the propagation of the mode to a cavity length L. Assuming that the plasmon mode supported by such a geometry is reflected by the end faces, the fundamental cavity mode will be excited when:

$$\kappa = \frac{2\pi}{\lambda_{\text{mode}}} = \frac{\pi}{L} \tag{7.1}$$

assuming a diffraction-limited lateral resonator width L.

Here, κ is the corresponding wave vector of the propagating plasmon. For example, for an incident wavelength $\lambda_0 = 800\text{nm}$ where $\kappa \approx 18.6\mu\text{m}^{-1}$, we have cavity length $L \approx 200\text{nm}$. The value for κ was numerically calculated for finite and homogenous metal-insulator-metal layers. Throughout this work we assume square resonators where $L = L_X = L_Y$.

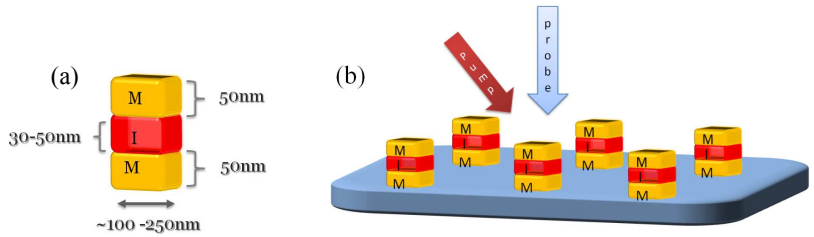

Figure 7.2: *(a) Schematic of an individual mini-MIM, i.e. a MIM square nanoparticle of size ranging from 100-250nm, also showing the respective thicknesses of each layer whereas (b) shows them arranged in an array with a given periodicity (500nm). The pump drives a nonlinear change in the polymer core whereas the probe feels the change optical response of the system.*

Next the optical properties of 2D arrays made of such individual resonators was numerically calculated. Specifically, the absorption of these

arrays on a glass substrate is calculated as shown in Fig. 7.2(b) as a function of the resonator length L. The structures were illuminated in normal incidence with a polarization in the plane of the nanostructures. The mismatch between the obtained resonance wavelength in Fig. 7.3 and the design wavelength can be explained by taking into account the phase of the reflection from the end surfaces (ϕ) as suggested in Ref. [121]. Consequently, the Eq. 7.1 is modified to:

$$\kappa = \frac{\pi - \phi}{L} \tag{7.2}$$

In this case, $\phi \approx 20$ degrees is a reasonable assumption, given that the end interface is heterogenous due to multiple metal-dielectric interfaces.

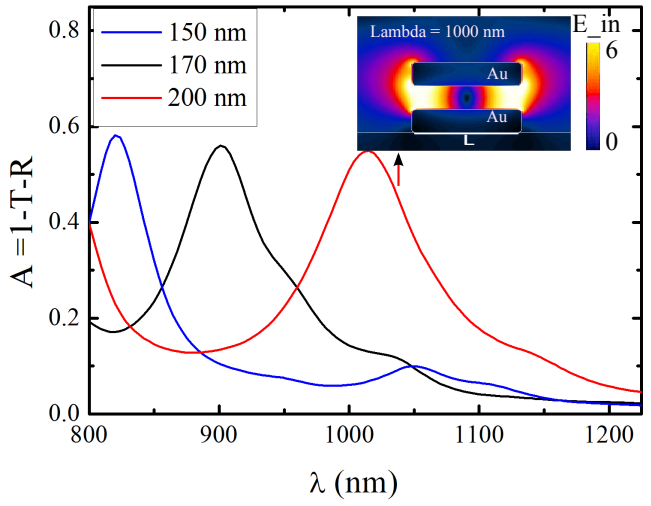

Figure 7.3: *The absorption spectra calculated using varying lengths L of mini-MIMs shows a red shift for larger sizes. The inset shows the computed electric field distribution at the plasmonic resonance for L= 200 nm.*

As shown in Fig. 7.3, the numerically calculated absorption spectra for a periodic array of MIM nanosquares varies as the length L is increased (150-200nm). The periodicity of the square array is 500nm and each nanosquare is a multilayer, consisting of Au (top and bottom) and a dielectric (in-between), with a refractive index $n = 1.6$. It is observed that it is possible to tune across a wide spectral range by slightly changing

the size of the nanosquares, i.e. L. Dependence with respect to other structural parameters such as the core thickness t and the core refractive index n was also investigated.

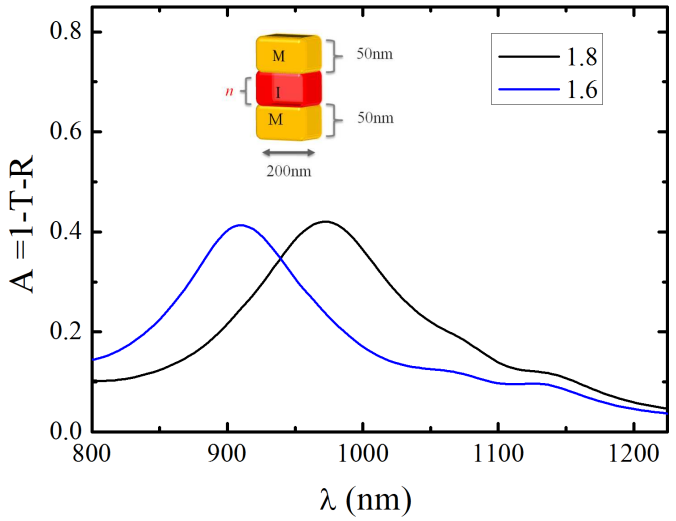

Figure 7.4: *The absorption spectra calculated numerically (as* $(1-T-R)$ *where* T *and* R *are transmission and reflection) for varying refractive index* n *when the size is kept constant at 200nm. The Au thickness is kept constant at 50nm for both top and bottom layers.*

The mini-MIM mode is designed such that large electric fields are concentrated at the center within the dielectric core, as shown in inset of Fig. 7.3. Due to this, these nanocavities are extremely sensitive to any perturbation in this region. Hence, it is foreseen that the conditions for mini-MIM plasmon mode, and therefore the overall absorption, can be altered by either a change in the refractive index of the dielectric n or its thickness t, as shown in Figs. 7.4 and 7.5. This can be achieved by replacing the dielectrics with active materials, such as all-optic materials whose refraction indices can be slightly changed by an external control signal. Note that in Fig. 7.5, as the thickness t is varied from 20nm to 50nm for (L = 200nm and period = 500nm), the shift in the absorption is significantly greater as compared to the change in absorption for 50nm to 70 nm (larger gap). This can be directly correlated to the fact the coupling between the top and bottom interfaces gets more sensitive as one approaches thinner dielectric layers for which the MIM modes have

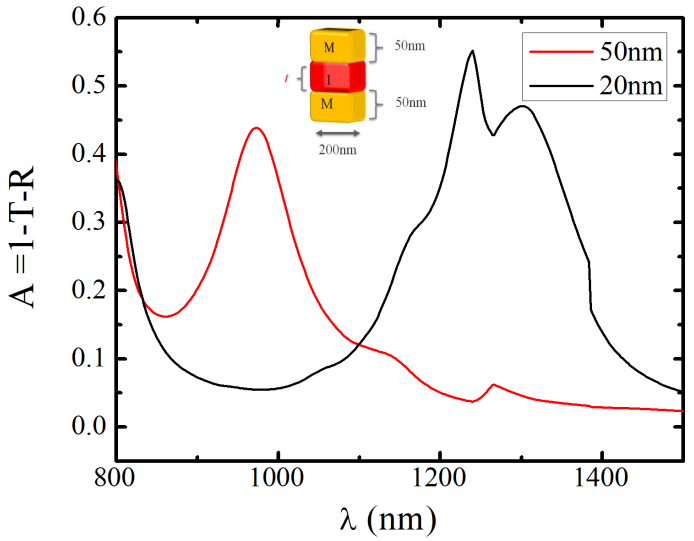

Figure 7.5: *The absorption spectra calculated numerically (as* $(1-T-R)$ *where* T *and* R *are transmission and reflection) for varying thickness* t *of the polymer core when the size is kept constant at 200nm. The Au thickness is kept constant at 50nm for both top and bottom layers.*

larger in-plane wave vectors. As the thickness t is increased beyond a certain limit, the change in wave vector becomes less significant as the modes lie very close to the light line (which is the limiting factor in this case lest the mode is rendered radiative).

Other parameters such as the dielectric index of the environment and the thickness of the metallic layer (above the bulk limit i.e. 15nm) have a not-so-dramatic impact on the mode and are not discussed in much detail here for the same reason. This could be attributed to the field of the MIM mode confined mostly within the core and much weakly in the surrounding media.

7.2 Fabrication

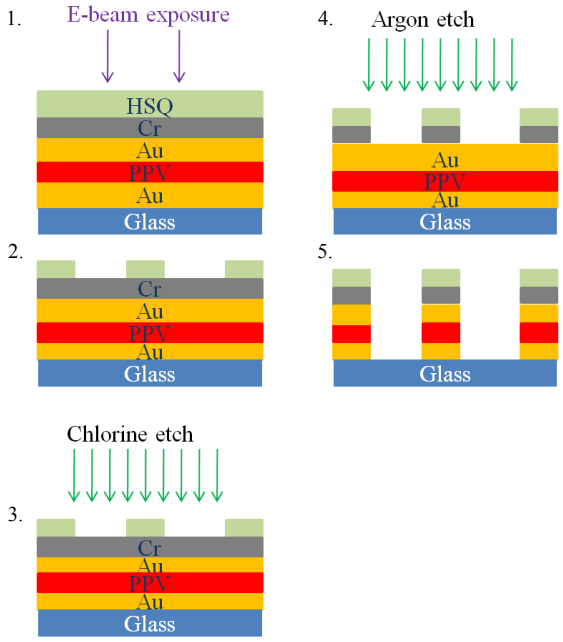

Figure 7.6: *Overview of the various fabrication steps.*

PPV films were prepared according to the standard precursor route in which first a precursor solution is prepared. More details with respect to this are given elsewhere [122]. PPV films were obtained by spincoating the solution of the precursor polymer onto glass substrates and thermally converted under vacuum at elevated temperatures ($\approx 220°C$) for 3-5hours.

The fabrication of the mini-MIMs was realized via a multi-step fabrication scheme as shown in Fig. 7.6. First, 50nm Au layer was thermally deposited on $\approx$ 0.5mm glass substrate. Next, a 30-50nm layer of PPV is coated on top of the Au layer. After this, another layer of Au ($\approx$ 50nm) was deposited on PPV to complete the planar MIM system. The patterning of the areas containing nanostructures (L ranging from 150 - 250 nm) arranged in a square lattice (periodicity 500nm) was done by exposing with a 100keV (JEOL) electron beam a 250nm-thick negative tone resist, hydrogen silsesquioxane (HSQ), layer on top of the multilay-

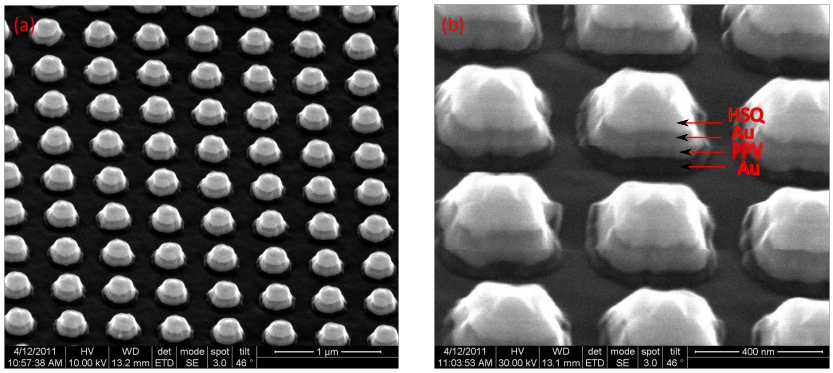

Figure 7.7: *(a)and (b) show SEM images of the fabricated mini-MIM samples. The sizes of mini-MIMs for (b) is larger and hence more squarish than that of (a).*

ers. A thin chromium (Cr) layer ≈ 5nm was deposited before spincoating HSQ on the top to create better adhesion of HSQ on Au surface. Proximity effect correction (PEC) was used for patterning of the nanostructures in order to ensure good edge quality for square cavities. The development was carried out in a hot solution of tetramethyl ammonium hydroxide TMAH:H_2O (ratio 3:1) at 50°C for 2 minutes. The sample was then treated with H_2O at 50°C, used as a stopper. Care was taken to avoid peeling off of the Au layers from glass surface due to poor adhesion sometimes. After development, the Cr layer was etched using a chlorine plasma in plasma etching tool (MARCH). Then via reactive ion etching (RIE) techniques (Oxford tool), the exposed regions i.e. ones not covered with HSQ were etched with argon plasma at 0°C all the way through the multilayers till the glass substrate to form the mini-MIM nanoresonators as shown in Fig. 7.6. A snapshot of the fabricated mini-MIMs is displayed in Fig. 7.7. The structural shape bears closer resemblance to a prismatic structure compared to cube due to the slopes created on the sides which are inevitable with Ar plasma as it is a purely physical sputtering process. A more careful look at the different layers of the fabricated samples shows that the end structures are symmetric due to the HSQ (Glass) remaining on the top. Also, there is a small amount of Au still remaining at the bottom (3-4 nm). The Au layer was delibrately not etched until completion to assist the coupling between the mini-MIMs. As the size of the structures increases, their resemblance to squares also

increases as can be seen in Fig. 7.7.

7.3 Characterization

The fabricated samples now contain a sandwich configuration with an exciton-supporting- polymer lying in between two plasmon-supporting metals pads. The dynamics of exciton-plasmon coupling in mini-MIMs were characterized using ultrafast femtosecond spectroscopy. We used a pump-probe scheme in which a pump laser pulse is used to excite the sample and a second, variably delayed probe pulse is used to monitor its time evolution. More details with respect to the setup and results will be discussed in next sections after a general introduction to this technique.

7.3.1 Transient Absorption Spectroscopy

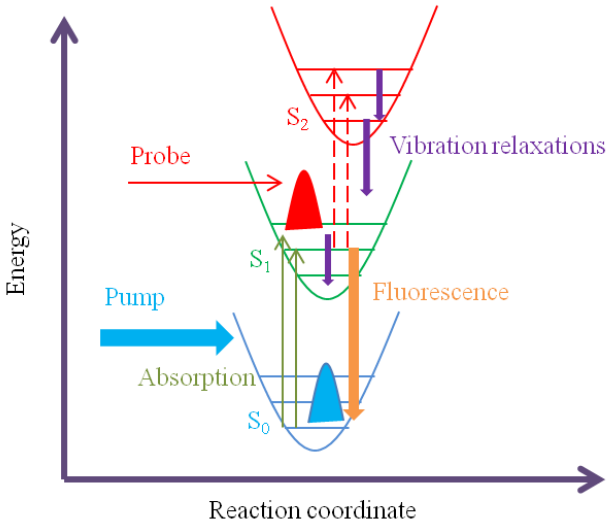

Figure 7.8: *(a) Schematic depicting the principle of Transient Absorption Spectroscopy(TAS) and the possible transitions at molecular level.*

Transient absorption spectroscopy (TAS) is a pump probe technique for investigating the excited state behavior of molecules in the form of molec-

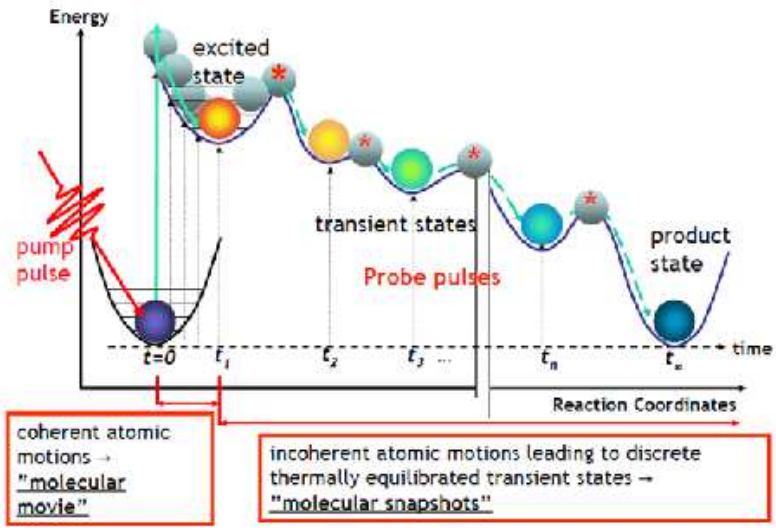

Figure 7.9: *Molecular snapshots with TAS allows to observe the various coupling and scattering mechanisms in "real time". Image reproduced courtesy Chen et al. Argonne National Labs.*

ular snapshots, where the optical signatures of transient species are captured at different times. A schematic illustrating the principle of TAS is shown in Fig. 7.8 and Fig. 7.9. Experiments based on TAS are capable of providing dynamical information that cannot be obtained by conventional spectroscopic techniques. Berera et al. [123] provides a nice introduction to the principles of transient absorption spectroscopy and the following sections contain parts that have been reproduced from this reference. In TAS, a fraction of the molecules is promoted to an electronically excited state by means of an excitation pulse (Pump) via single photon excitation at a wavelength lower than the absorption maximum of the material. Depending on the type of experiment, this fraction typically ranges from 0.1% to tens of percents. A weak probe pulse which has such a low intensity that multiphoton/multistep processes are avoided during probing, is sent through the sample with a delay s with respect to the pump pulse. Typically, the probe pulse could be a tightly focussed white light continuum (WLC) pulse and depending on the interaction of the excited molecule with this selected wavelengths of the WLC and the duration of such as interaction, both spectral and kinetic signature of a molecule's

dynamics is monitored. A difference absorption (ΔA) spectrum is then calculated, i.e. the absorption spectrum of the excited sample minus the absorption spectrum of the sample in the ground state. By changing the time delay s between the pump and the probe and recording a ΔA spectrum at each time delay, a ΔA profile as a function of τ and wavelength λ, i.e. a ΔA (λ, τ) is obtained. Hence, one obtains data that can be represented in three dimensions, namely changes in absorbance, wavelength and time. Different possibilities are excited state energy migration, electron and/or proton transfer processes, isomerization, and intersystem crossing etc.

A ΔA spectrum could typically contain contributions from various processes such as ground state bleach, stimulated emission or excited state absorption. In the case of ground state bleach, the number of molecules in ground state decreases due to excitation to a higher state through the action of the pump pulse. Hence, the ground-state absorption in the excited sample is less than that in the non-excited sample resulting in a negative signal in the ΔA spectrum in the wavelength region of the ground state absorption. In the case of excited state absorption, optically allowed transitions from the excited (populated) states of a chromophore to higher excited states may exist at certain wavelengths, resulting in an absorption of the probe pulse at these wavelengths under the influence of the pump beam. Consequently, a positive signal in the ΔA spectrum is observed in the wavelength region of excited-state absorption. For stimulated emission, upon population of the excited state under the action of pump, stimulated emission to the ground state will occur when the probe pulse passes through the excited volume. Hence, the probe photons are not being absorbed, but emitted by the molecule. Thus, stimulated emission is another example of a signal causing a negative ΔA.

These three cases represent the most frequently encountered signals in transient absorption measurements. By monitoring the kinetics of these signals, the excited state dynamics of a molecule can be resolved. Several other phenomena that are possible to monitor such as singlet $\rightarrow$ triplet transitions, bleach recovery of the ground state, vibrational cooling and thermalization.

7.3.1.1 TAS of Localized Surface Plasmons

Metal nanoparticles have been used in time resolved techniques to study the electron dynamics. Over the past several years a major focus of research in this area has been to explore the fundamental photophysics of metal particles using ultrafast laser spectroscopy. However, at the surface plasmon resonance, a bleach is observed in the transient absorption spectra of metallic nanoparticles. The current understanding of the response of metal nanoparticles to an ultrafast laser pulse as per Hodak et al. is reproduced below:

When a 400nm laser pulse is used to excite the sample containing Au, electrons are promoted from the filled 5d band to empty states above the Fermi level in the 6sp band, as this color predominantly excites 5d $\rightarrow$ 6sp interband transitions [124–126]. The energy deposited by the pump laser is rapidly equilibrated (<200fs) among all the conduction band electrons by electron-electron scattering [127–129]. These processes occur before any significant energy exchange between the electrons and phonons in the case of pure Ag and Au particles. Due to the large increase in the electronic temperature (several thousand Kelvins) by ultrafast laser excitation, the occupation of the electronic states near the Fermi level changes. This in turn, affects the interband contribution to the dielectric constant [130, 131]. The changes of the dielectric constant at the interband transition broaden the plasmon band, creating a strong bleach signal at the band maximum and absorption signals in the wings of the band [132]. The magnitude of the bleach is proportional to the electronic temperature [133, 134]. As time progresses the electrons equilibrate with the lattice via electron-phonon coupling [135, 136]. This process can be monitored by measuring either the recovery of the bleach in the spectral signature or the decay of the transient absorption signal in the kinetics. A typical plasmon bleach of metal nanoparticles is observed as a dip in ΔA spectra. Usually, 100fs laser pulses can provide sufficient time resolution to study coupling between the excited electron distribution and the phonon modes of the particles.

The interaction of metal surfaces with optically excited molecules is interesting as molecular interactions with metal nanostructures produce new routes to new energy dissipation processes impacting a wide range

of fields such as ultrafast integrated optical circuitry and ultra-sensitive spectroscopic methods, giving rise to the field of *molecular plasmonics*. For example, due to the coupling to the electronic polarizations of the metal, strong modification of the emission lifetime of molecules can be affected by a change in photon density of states near a metal surface leading to quenching and/or enhanced emission [137]. Due to the enhanced optical near field or evanescent field accompanied by the plasmon resonances of a range of metallic nanostructures, these structures can act as a local source to interact with molecular adsorbates like in surface enhanced Raman scattering (SERS). Moreover, strong coherent coupling between excitons of molecular semiconductors and surface plasmons has been discovered due to the ultrafast polarization response of both the exciton and plasmon. This enables new possibilities to manipulate excitation processes on an ultrafast time scale where plasmon-exciton coupling can be used to manipulate the energy dissipation processes in molecules following the photoexcitation.

When coupled to metal nanoparticles, the excitation may not be purely molecular or plasmonic but may be described by a hybrid state with optical properties different than either component. Hence, the optical properties associated with the hybrid coupled system show mixed behavior with respect to each of the constituents. This provides a powerful means to tailor the optical properties of plasmonic systems for the desired optical functionalities. An effort towards this direction of observing such phenomena in the hybrid mini-MIMs is explored in the next sections.

7.3.2 Characterization Set-up: Mini-MIMs

TAS measurements for this experiment made use of a 35fs pulse width, 2kHz commercial Ti:Saph amplifier. Tunable pulses were generated with a white-light seeded optical parametric amplifier (OPA). The pulses from the oscillator are too weak for any meaningful spectroscopy and therefore have to go through an amplification process. Time delayed pulses of the white light produced in a 2mm thick sapphire plate were used to probe the samples. The pump pulses were centered at 470nm and generated at 1kHz. The repetition rate of 1-5kHz signifies relatively high pulse energy $\approx$ 5-100nJ. The spot size for the pulse was estimated to be $\approx$ 100μm

diameter and typically 2-20% of the molecules being promoted to the excited state. This value is only an estimation of the excitation density because it depends on several factors, namely, the exact size of the focus, the concentration of the chromophores, and their extinction coefficient as per Berera et al. [123].

The variable time delay between the pump and probe pulse is achieved with a so-called delay stage. The pump pulse generated by an OPA is sent through an optical delay line, which consists of a retroreflector (mirror) mounted on a high-precision motorized computer-controlled translation stage. Moving the mirror changes the path length of the light. Since the speed of light is a constant, the arrival time of the pulse at the sample changes accordingly. For example, displacing the mirror by 1micron gives a time delay of 2×3.3fs ($t = L/c$, L: length, c: speed of light). For a better temporal resolution, it is possible to have timing accuracy of ≈ 0.1fs. Since the delay line can be moved over 80cm, time delays up to 5ns can be generated between excitation and probe beams which is also the lower temporal limit for a TAS system. Processes that occur on a slower timescale than nano-seconds and faster than $\approx$ 100fs cannot be studied with this particular system.

A transient absorption experiment is done in the following manner: the time delay between excitation and probe beams is fixed. For sensitive detection, the pump beam passes through a mechanical chopper that is synchronized to a lock-in amplifier in such a way that every other pump pulse is blocked, i.e. before it reaches the sample. Thus, alternately the excitation of the sample is switched on and off. Consequently, the white-light continuum that is incident on the detector diode array alternately corresponds to a "pumped" and "unpumped" sample, and the detector alternately measures the intensity of the probe beam of a "pumped" and "unpumped" sample, I_{pumped} and I_{unpumped}. To further increase the signal-to-noise ratio, the probe beam is used as a reference (I_{ref}) which does not passes through the sample. A difference absorption spectrum can then be constructed as shown below:

$$\Delta A = A_{\text{exc}} - A_{\text{noexc}} = -\log\left(\frac{I_{\text{pumped}}/I_{\text{ref}}}{I_{\text{unpumped}}/I_{\text{ref}}}\right) = -\log\left(\frac{I_{\text{pumped}}}{I_{\text{unpumped}}}\right) \tag{7.3}$$

This is repeated each time the delay line is moved to another time delay between pump and probe. The information about the temporal evolution of the excited state which we are interested in, is collected by varying the temporal overlap between pump and probe pulse via the delay stage and measuring the time averaged transmission of the sample at each position of the delay. This way, absorbance difference spectra at many time points between 0fs and $\approx$ 5ns are collected, along with absorbance difference spectra before time zero to determine the baseline. In addition, to enable accurate recording of the instrument response function, many spectra are collected around the time that pump and probe pulse overlap in time (zero delay). As per Berera et al. this procedure is repeated several times to test reproducibility, sample stability, and long-term fluctuations of the laser system. In this way, an entire dataset $\Delta A(\lambda, \tau)$ is collected. [123]

In our experiments, the pump light was chosen at $\lambda = 470$nm in order to overlap with the optical resonance of the active polymer (PPV) and was polarized in the plane of the sample, i.e. along the MIM vertical direction. Next we discuss the ΔA results obtained for planar PPV films.

7.3.3 TAS Spectroscopy: Response of PPV

PPV belongs to the family of polymers which possess strong π-electron conjugation. In order to study the femtosecond response of the PPV films, TAS experiments were performed on the planar films of thickness $\approx 30 - 50$nm on bare glass substrates. This way the damage threshold for femtosecond pulses for PPV could also be evaluated.

Before this, bare PPV films were characterized by UV-VIS-NIR spectroscopy. Absorption peak of the PPV films extends from 300-500nm and shows a maximum at $\approx$ 400nm. Hence, the pump beam for femtosecond spectroscopy was chosen to be fixed at 470nm for all the experiments. PPV films turned out to be very robust withstanding high pump intensities without damage. We tested the films upto $\approx$ 100GW/cm^2 and noticed telltale signs of slight damage above 20GW/cm^2.

Figures 7.10 and 7.11 show the spectral and kinetic response of PPV when probed in the NIR with white light and for $I_{pump} \approx 10$ GW/cm^2. The

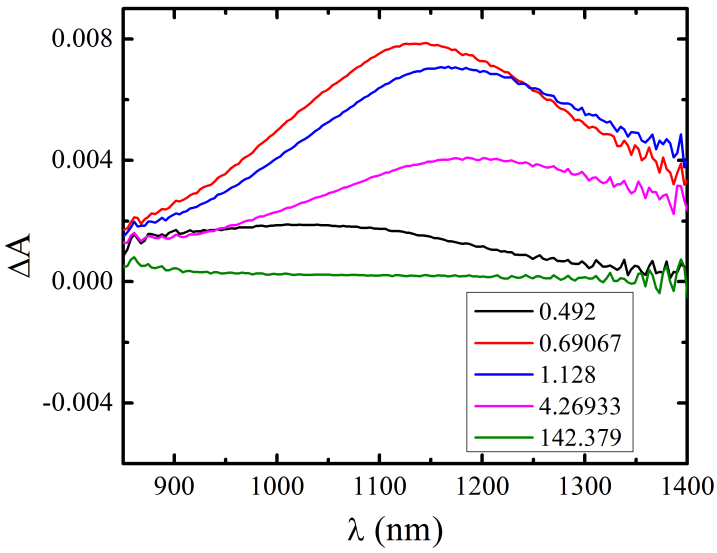

Figure 7.10: ΔA *spectral evolution at different delay times for a planar PPV film at for Pump at 470nm* (I_{pump}= *10* GW/cm^2*.)*

spectral response shows a broad peak in ΔA evolution at different times. This is an indication of an excited state absorption, i.e. optically allowed transitions from the excited (populated) states of a PPV to *higher* excited states exists in this wavelengths regime. This is a result of absorption of the probe pulse at these wavelengths under the influence of the pump beam. The differential absorption signature rises to its peak in $\approx$ 700fs and decays back to the half of the original intensity at 4ps, completely dying out at $\approx$ 107ps. After a more careful examination of the kinetics response (see Fig. 7.11), it is found that the decay signal has three main contributions as per the exponential fits. Within the first 1.94ps there is a sharp decay of the signal as compared to the second regime which extends to $\approx$ 50ps. The first regime is of greater interest as it captures the response at early time scales and is later important while studying the hybrid effects mixed with plasmonic response. The third regime is usually dominated by the phonon-phonon interactions till the signal completely dies out.

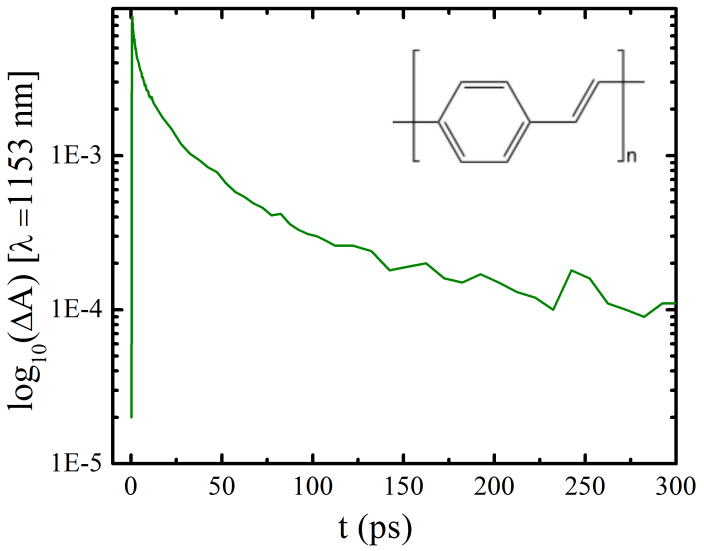

Figure 7.11: *Kinetics for PPV at $\lambda = 1153nm$. Inset shows the chemical structure representative of a PPV molecule with π-conjugation.*

In order to understand the origin of the excited state absorption, a deeper look into the different energy states of PPV is necessary. Figure 7.12, as per Frolov et al. [138] shows a configuration coordinate diagram of low-energy excited states in PPV polymers. As per Frolov et al. the various excitation manifolds are marked by dashed line boxes and narrow vertical arrows show optical transitions, whereas broad arrows indicate nonradiative relaxation pathways. Since a PPV chain is a molecular system having a center of inversion, its excited states have been classified as A_g where g stands for 'gerade' or even parity states and B_u stands for 'ungerade' or odd parity states, corresponding to one photon and two-photon allowed transitions, respectively. In single pump-probe experiments typically one is able to excite the $1B_u$ excitonic state. The A_g states, which are not observable by one-photon absorption, can usually be found from the two-photon absorption spectrum. In the case of PPV films in this study it is obvious that excitation into the $1B_u$ state takes place with the pump at 470nm ($\approx$ 2.63eV). Moreover, what is more interesting is the fact that with probe energy of ($\approx$ 1.12eV), a

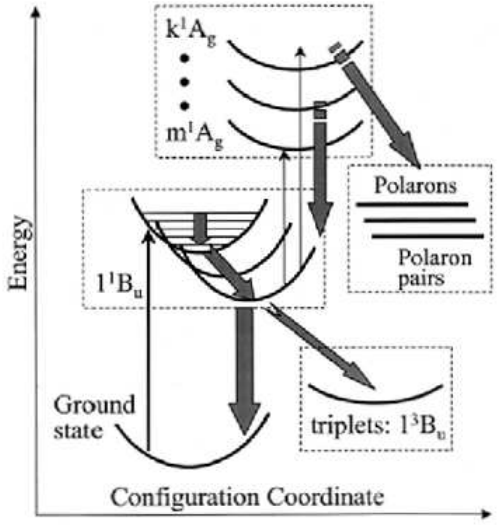

Figure 7.12: *Configuration coordinate diagram of excited states in PPV polymers showing different excitation levels [Scheme reproduced from [138]]*

further excitation into the A_g band takes place. This is in accordance with the data presented in Fig. 2 of the paper by Frolov et al. [138] (We assume that the structure of PPV and the PPV derivatives follow a similar trend which is reasonable.) According to the paper, there are prominent bands of two different A_g states, m^1A_g at 3.2eV and k^1A_g at 3.6eV, which they have determined using both two-photon absorption and transient photomodulation spectroscopies. Typically, optical excitation into either of these states is followed by subpicosecond nonradiative relaxation to the lowest excited state. They found out that m^1A_g obeys the Vavilov-Kasha rule (stating that fluorescence typically occurs from the lowest excited electronic state and its quantum yield is independent of the excitation wavelength) and decays back to $1B_u$ via internal conversion within 200fs. However, k^1A_g exhibits anomalous behavior and relaxes into a longer-lived, nonemissive state, which is attributed to a bound electron-hole polaron pair. This nontrivial result indicates that k^1A_g may be categorized as a charge-transfer state and such states are thought to be a prerequisite for carrier photogeneration.

In this experiment it is highly likely that the k^1A_g band is excited given the matching pump and probe energies (2.63 and 1.12eV respectively).

7.3.4 TAS Response of Mini-MIMs

After having studied the spectral and kinetic response for pure PPV films on bare glass, the next step was to study the TAS response for mini-MIMs fabricated on a glass substrate. In order to get a spectral overlap with the observed ΔA signal of PPV, the size of the structures was tuned in the range of $L \approx 200 - 300$nm. This ensured a characteristic hybrid response due to the contribution from both plasmonic mode as well as that of PPV under the influence of the pump and probe beams.

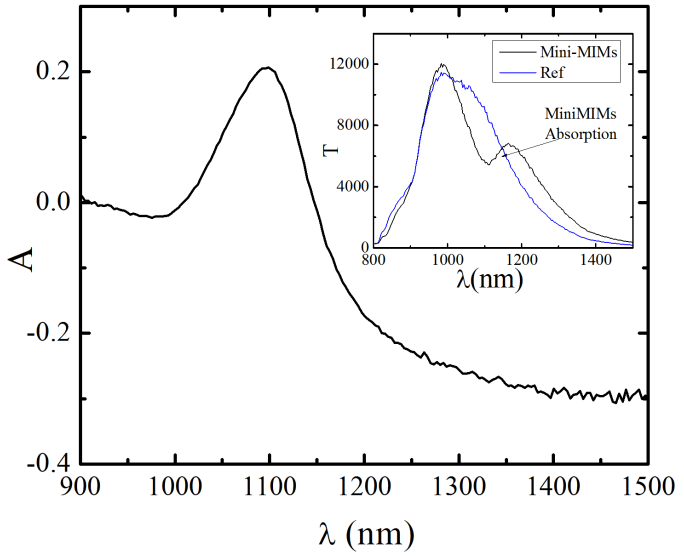

Figure 7.13: *Experimentally measured ground state absorption of mini-MIMs. Inset shows the transmission data for the same sample and the reference which was the signal measured outside the fabricated areas.*

In order to confirm the plasmonic MIM mode, absorption spectra of the areas containing mini-MIMs of different sizes was extrapolated from the transmission of the probe beam i.e. NIR white light. Figure 7.13 shows the measured absorption for an area containing mini-MIM nanostructures

where the absorption peaks at ≈ 1096nm and the FWHM in the order of ≈ 85nm. This implies a lifetime of ≈ 50fs for the plasmonic mode. The absorption A is calculated from the transmission data (see inset of Fig. 7.13) as $A = -\log \frac{T_{\text{mini-MIMs}}}{T_{\text{ref}}}$, where T_{ref} is the transmission through sample without mini-MIMs, as shown in blue in the inset. There is a small difference of transmission recorded at different locations on the sample due to the topographical changes resulting from the leftovers of etched Au which was still remaining (≈ 4nm) on glass.

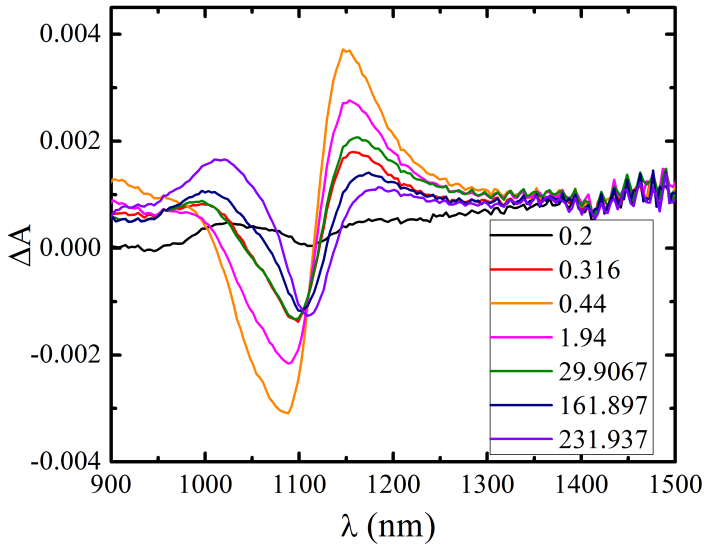

Figure 7.14: *The transient ΔA signature for mini-MIMs evolving from a strong derivative like shape to a plasmon bleach as a function of time.*

The absorption peak at 1096nm ensures interaction with the PPV layer as it lies well within the desired spectral range (1000-1300nm). Next, the influence of the pump and probe beam on the hybrid nanoparticles was studied and their differential absorption ΔA recorded at various time intervals. The spectral response for pump intensity of 80μW or 10GW/cm^2 is shown in Fig. 7.14. The derivative like shape of ΔA signal suggests red-shifts of absorption induced by the pump. The magnitude of the ΔA peaks at 440fs, showing a strong derivative shape. The dip (δD) at blue wavelengths coincides with the spectral location of the expected plasmon

bleach and the peak (δP) at wavelength $\approx$ 1150nm could be attributed to the excited state contribution of PPV. This signature from the hybrid nanostructures confirms the mixed response from both the plasmons and π-conjugated electrons in PPV. However, interestingly this shape converts back into a regular bleach shape expected for plasmons due to phonon-phonon interactions at later timescales for example $\approx$ 200ps.

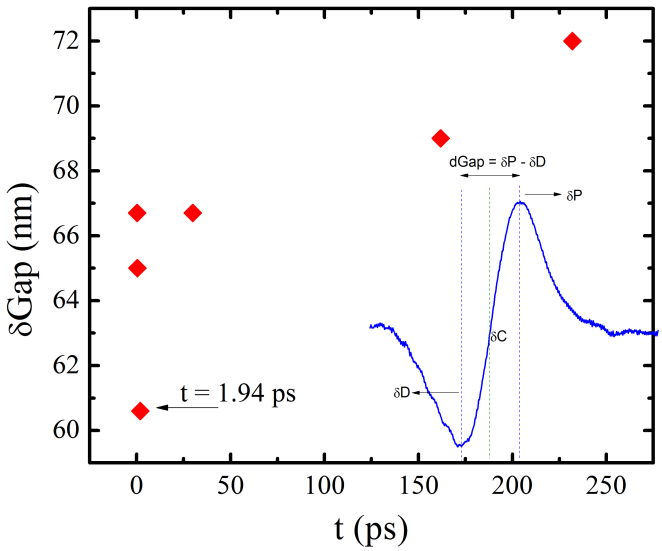

Figure 7.15: *The difference between the dip and the peak of the ΔA signal measured as δGap indicates a strong narrowing at early timescales, a characteristic feature observed for the mini-MIMs.*

An outstanding feature of the transient absorption signature of hybrid mini-MIM modes is the narrowing at early femtosecond timescales as shown in Fig. 7.15. In the figure, the gap, (δGap see also inset) which is the difference between the dip, δD and the peak, δP is measured at different times. Strong narrowing of δGap is observed at the early timescales up to 1.94ps after which it recovers back to the original value at t $\approx$ 20ps and goes on to increase later with increasing times. The broadening of δGap at late timescales is not surprising as this broadening could again most likely be attributed to phonon-phonon interactions.

In order to understand more in detail the strong shifts and narrowing of ΔA signature at early timescales, we analyze this data and identify the possible reasons for the observed phenomena in the next section.

7.4 Discussion

In order to investigate further the amount of shift in the absorption causing the derivative like shape of the differential absorption, the shifted absorption A, at a given time t was reconstructed from the original absorption curve (without Pump) and the differential absorption, ΔA curve at the time t by using the following mathematical relation:

$$f_A(\lambda + \Delta\lambda) = \Delta A \Delta\lambda + f_A(\lambda) \tag{7.4}$$

where, $f_A(\lambda)$ and $f_A(\lambda+\Delta\lambda)$ are the original and extrapolated absorption curves and $\Delta\lambda$ is the spectral shift between the two.

Figure 7.16 shows the extrapolated absorption curves for $t = 440$fs (solid black) and $t = 29$ps (solid violet), and the ΔA curves for each of these times (black and violet squares respectively). The ground state extinction of the mini-MIMs (dashed red) is the same as shown previously in Fig. 7.13. $\Delta\lambda \approx 30$nm was chosen based on curve fits. However, it is important to note that in order to obtain a good fit an assumption solely based spectral shift was not sufficient to reproduce the curves. Additionally, narrowing of the spectral band had to be taken into account. This is in fact also supported by the extrapolated curve for $t = 440$fs (solid black) in Fig. 7.16 which is not only shifted by 30nm (peak to peak) but also accompanied by a strong narrowing of ≈ 50nm which is about 35% of the FWHM of the ground state absorption/extinction (dashed red). Moreover, one observes that at $t = 29$ps, the extrapolated curve (solid violet) almost relaxes back to the original values and does not show any spectral shift or narrowing effects. It might be broadened slightly due to thermal effects kicking in because of the phonon-phonon interactions. Also the ΔA curve for this time (violet) shows signature resembling more like an expected plasmon bleach with dying absorption for PPV at the red end.

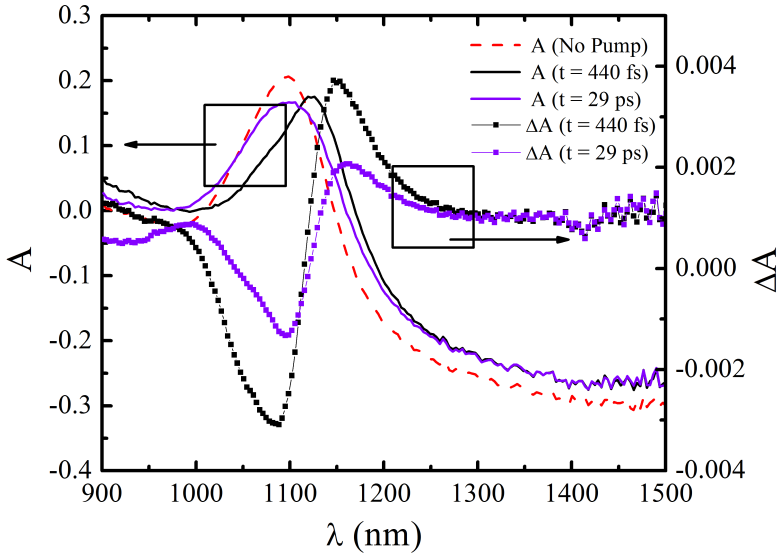

Figure 7.16: *Reconstructed absorption curves (solid) for time $t = 440fs$ (black) and $t = 29ps$ (violet), extrapolated from the ΔA (squares) at the respective times and the ground state absorption (dashed red).*

In order to reach a hypotheses for the interesting results obtained, it is important to understand the role of pump power for the effects noticed. The effect of magnitude of the pump power on the ΔA signal is shown in Fig. 7.17 which shows an expected increase in the signal for increasing pump powers which can be attributed to the increasing electron temperatures due to increased pump intensity. Figure 7.18 shows this increase is almost linear with respect to the pump power (for the δD (blue) marked in Fig. 7.17). Also, the effect of narrowing of the ΔA signal becomes significantly enhanced, with δGap (red) reducing from 80nm to 65nm as the pump power is doubled (see Fig. 7.18).

It is possible to understand the origin of the induced spectral shifts observed for the hybrid response of the mini-MIMs containing an active π-conjugated polymer in the center of the localized MIM mode. When the pump is 'ON', the higher state excitation into the kA_g takes place

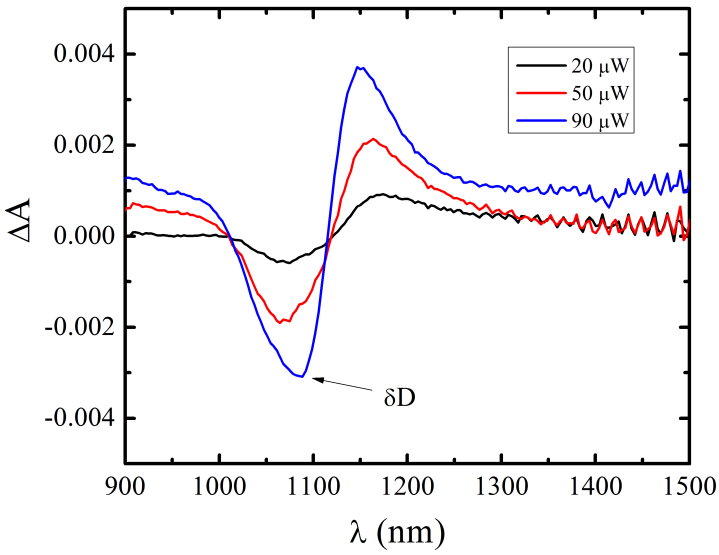

Figure 7.17: *Effect of increasing pump power at $\lambda = 470nm$ for the ΔA signal.*

propelled by the absorption of the probe. Following the Kramer-Kronig law, a change in the absorption or the imaginary refractive index should drive a corresponding change in the real part of refractive index as well and vice verse. This could explain for the index change of PPV due to increased polarizability arising from the higher state excitation. As the mini-MIM modes are engineered to have a strong electric field confinement within the PPV layer, an alteration of index of PPV would produce a shift in the absorption.

On the other hand narrowing at the early timescales is quite an unusual effect which to our knowledge has not been reported before for such a scenario. Earlier timescales are particularly interesting as it provides more information related to absorption compared to longer timescales, usually associated with radiative decays or phonon-phonon interactions in a molecular system. One possible explanation is that it could be attributed to the creation of bound electron-hole polaron pairs following the excitation into the kA_g band in PPV [138]. This could increase the

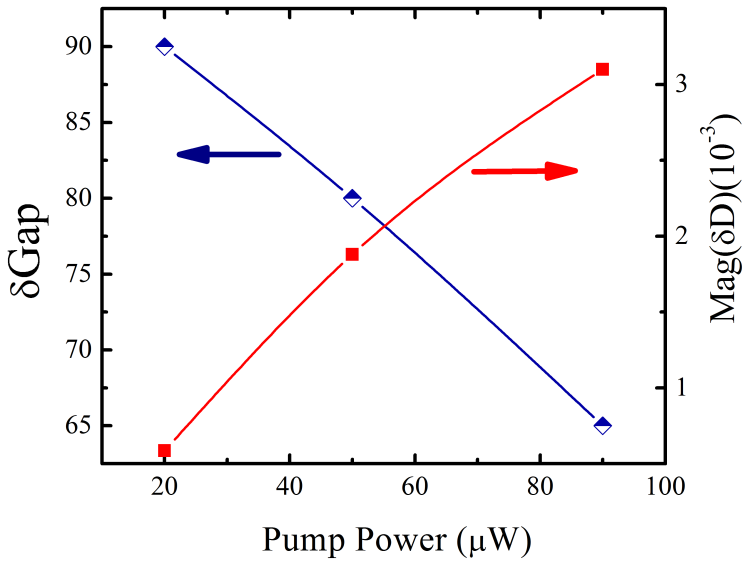

Figure 7.18: *Effect of increasing pump power at $\lambda = 470nm$ for the δGap (blue) and the magnitude of the dip ($Mag(\delta D)$)(red).*

degree of collective oscillations extending across the entire MIM structure due to the added effect of coherence from the generated polarons, which could be responsible for the narrowing. This effect could also be enhanced by the increase in the polarizability of the PPV.

7.5 Summary

In conclusion, the plasmonic resonance in an array of Metal-Insulator-Metal (MIM) square shaped cavities (mini-MIMs) has been investigated. These nanostructures enable squeezing of light to the order of $\lambda/4$. The electromafnetic field of such modes is strongly confined in the dielectric core and is very sensitive to any perturbation. Taking advantage of this, the dielectric core is replaced by an active polymer such as PPV which due to its interaction with the plasmonic resonance gives rise to novel hybrid phenomena at the nanoscale.

Due to the extreme sensitivity of the plasmonic MIM mode to any changes, the plasmonic response of the mini-MIMS is thereby altered significantly, resulting in a remarkable spectral shift of $\approx$ 30nm. Moreover, these changes are accompanied by novel phenomenon of strong narrowing seen at early timescales which could be attributed to increased oscillations extending across the entire MIM cavity due to added coherence of electron-hole polaron pairs generated at those timescales. The mini-MIMs presents an excellent opportunity to study the fundamental interactions of optically induced higher state transitions in a π-conjugated polymer in the presence of a plasmonic mode (simultaneously optically induced). This results in a hybrid response which is a manifestation of the coupling between the plasmonic polarizations and the molecular excitations. These ultrasmall active plasmonic cavities explores control of such hybrid interactions, enabling further advancement in the directions of ultrafast coherent control of molecular excited states as well as ultrafast switching in plasmonics-based components.

Conclusion

In recent years, plasmonics has drawn tremendous attention in the scientific community, impacting several important and interesting applications ranging from biosensing, cancer treatment, integrated nano-circuitry and solar energy conversion. The nano-concentration of optical energy, and the ability to control such highly confined plasmonic fields at the metal-dielectric interface are both challenging and promising. An interesting method of achieving such control is by combining plasmonics with active dielectrics, paving the way for studying novel phenomena associated with light-matter interactions at the nanoscale. The design and creation of new hybrid plasmonic-active materials that have unique nonlinear optical and photo-electrical responses hold tremendous potential in nanoscience.

Research studies in this thesis have been geared towards addressing different aspects of active control in hybrid plasmonic nanostructures. On one hand, passive plasmonic prototypes such as dielectric Bragg mirrors and coupled dielectric resonators have been developed. Using both theoretical and experimental techniques, these have been studied carefully in terms of their critical parameters for enhanced performance. On the other hand, different types of active dielectric platforms have been studied in terms of their nature/origin, and the optimization of their linear and nonlinear optical properties. By incorporating active materials in hybrid plasmonic systems, control over propagating surface plasmons has been experimentally demonstrated via electro-optical and all-optical methods. Beyond active control, insights into the hybrid interactions at ultrafast timescales have been drawn that pave way towards understanding different competing processes, and possibly novel phenomena that arise as a result of hybridization. Metal-Insulator-Metal nanocavities or *mini-MIMs*, which are employed to achieve this, have been shown to make attractive candidates for ultrafast applications.

This thesis has been structured in the following manner: after a basic introduction to the area of active plasmonics, and how this field has

evolved over the years, the basics of plasmonics, and the sensitivity of a plasmon to refractive index change are discussed. Importantly, the criteria for developing hybrid plasmonic nanomaterials are detailed. Several challenges in terms of optimizing the characteristic properties in both plasmonic configurations and active materials are highlighted.

Initially, a grating composed of dielectric ridges on a flat Au layer has been demonstrated to control the propagation of SPPs by opening a gap in its dispersion relation. These structures draw analogy to the standard optical Bragg stacks design. The properties of the gap have been analyzed as a function of varying grating parameters. The influences of the dielectric grating height and the filling factors conform well to the analogous standard optical system. Also, the performance of these dielectric gratings as SPP Bragg mirrors has been demonstrated. The results show very good reflecting properties up to 85%. Since these plasmonic structures show the ability to tune the band-gap, they could be potential candidates for active modulation of surface plasmons. Combining this plasmonic prototype with suitable nonlinear materials could be an interesting research study for the future.

Following that, the use of dielectric-loaded plasmonic waveguide (DL-SPPW) based coupled resonator systems have been highlighted. Another variant of the plasmonic ring resonator (WRR), namely the plasmonic disk resonator (WDR), has been proposed. The efficiency and the compactness offered by this component operating at telecom wavelengths have been studied by combining SNOM characterization and numerical modeling. In order to optimize the device performance in terms of the modulation depth and wavelength selectivity, the role of various important parameters such as the disk radius and gap separation have been analyzed. The disk resonator design has been shown to be superior to its ring counterpart because of the ease of fabrication and smaller radiation, and slightly better performance in the wavelength selection for integrated photonic circuitry.

Next, transition was made towards incorporating active materials in hybrid plasmonic nanostructures based on active dielectric-loaded surface plasmon WRR/WDRs. Electro-active modulation of SPP in this configuration has been studied by doping the dielectric host matrix with an

electro-optical material. Details for the fabrication of a novel design with in-plane electrodes done via multi-step lithography procedure with high resolution have been presented. Characterization using leakage radiation microscopy (LRM) showed a 16% relative change in the transmission by electrical control. The temporal response of the device has been analyzed, and conclusions pertaining to the dominant role played by the electrostriction of the host matrix in the transmission response have been drawn. These results could be relevant for future design of electro-active plasmonic devices in implementing plasmonics based nano-circuitry.

In addition, details regarding all-optical control of a propagating surface plasmon in a WRR when combined with the nonlinearity based on trans-cis isomerization in a polymer have been chalked out. Large changes in the refractive index due to trans-cis isomerization have been observed by doping the host matrix (Poly Methyl Methacrylate: PMMA) with DR1 molecules, when pumped with light near absorption resonance. It has been shown that transmission in a DLSPPW WRR changes by a factor of 4 between high and low transmission states of the device, at milliwatt control powers (100W/cm^2 intensity), with the performance limited by the slow relaxation of the disperse red 1 (DR1) molecules (cis-trans).

Finally, ultrafast spectral and temporal dynamics due to electromagnetic coupling between the molecular interactions in a pi-conjugated polymer with plasmonic resonances in a periodic arrangement of hybrid MIM nanocavities has been investigated. Coined as "mini-MIMs", these plasmonic nanostrutures enable squeezing of light to the order of $\lambda/6$. Intense, localized electric field distributions at their core nanostructures alter their overall ultrafast absorption due to the induced polarizability change in the polymer. As a result, strong spectral shifts in the transient signature of these nanostructures have been observed. This was accompanied by a novel phenomenon of narrowing of the transient signal at early times due to the enhanced coherence interactions. These results provide interesting insights into ultrafast light-matter interactions in hybrid nanomaterials.

It has been shown, therefore, that plasmonic configurations based on dielectric based SPP mirrors and coupled resonator systems (WRR/WDR) are highly sensitive, compact and efficient candidates for SPP modula-

tion. The design and creation of novel hybrid plasmonic-active nanostructures that modulate the hybrid optical response via all-optical and electro-optical control have been demonstrated. Through ultrafast studies of MIM based nanocavities, the control of ultrafast absorption at the nanoscale via the interactions between plasmonic polarization and molecular excitations has been explored. These results are promising for a wide range of applications ranging from integrated optical nanocircuitry, biosensing, energy conversion and ultra-sensitive spectroscopic methods.

List of Journal Publications

- S. Randhawa, M. U. González, J. Renger, S. Enoch and R. Quidant, "Design and properties of dielectric surface plasmon Bragg mirrors," *Optics Express*, vol. 18, no. 14, pp. 14496-14510, 2010.

- S. Randhawa, A. V. Krasavin, T. Holmgraad, J. Renger, S. I. Bozhevolnyi, A. V. Zayats and R. Quidant, "Experimental demonstration of dielectric-loaded plasmonic waveguide disk resonators at telecom wavelengths," *Applied Physics Letters*, vol. 98, pp. 161102, 2011.

- S. Randhawa, A. V. Krasavin, J.-S. Bouillard, J. Renger, R. Quidant and A. V. Zayats, "Optically-programmable nonlinear photonic component for dielectric-loaded plasmonic circuitry," *Optics Express*, vol. 19, no. 25, pp. 25222-25229, 2011.

- S. Randhawa, S. Lachèze, J. Renger, A. Bouhelier, R. E. de Lamaestre, A. Dereux and R. Quidant, "Performance of electro-optical plasmonic ring resonators at telecom wavelengths," *Optics Express*, vol. 20, no. 3, pp. 2354-2362, 2012.

- S. Randhawa, G. P. Wiederrecht, J. Renger, L. Ocola, N. F. Scherer and R. Quidant, "Ultrafast control of absorption in arrays of hybrid plasmonic MIM nanocavities," In preparation, 2012.

Bibliography

[1] S. Maier, "Plasmonics – towards subwavelength optical devices," *Current Nanoscience*, vol. 1, no. 1, pp. 17–22, 2005.

[2] R. Wood, "On a remarkable case of uneven distribution of light in a diffraction grating spectrum," *Philosophical Magazine*, vol. 4, pp. 396–402, 1902.

[3] U. Fano, "The theory of anomalous diffraction gratings and of quasi-stationary waves on metallic surfaces (Sommerfeld's waves)," *Journal of the Optical Society of America*, vol. 31, no. 3, pp. 213–222, 1941.

[4] A. Otto, "Excitation of nonradiative surface plasma waves in silver by the method of frustrated total reflection," *Zeitschrift für Physik*, vol. 216, pp. 398–410, 1968.

[5] E. Kretschmann and H. Raether, "Radiative decay of non-radiative surface plasmons excited by light," *Zeitschrift für Naturforschung*, vol. 23, no. 12, pp. 2135–2136, 1970.

[6] H. Raether, *Surface Plasmons on Smooth and Rough Surfaces and on Gratings*. Springer-Verlag, 1988.

[7] K. Kneipp, H. Kneipp, I. Itzkan, R. Dasari, and M. Feld, "Surface-enhanced Raman scattering and biophysics," *Journal of Physics: Condensed Matter*, vol. 14, no. 18, pp. R597–R624, 2002.

[8] T. Chinowsky, L. Jung, and S. Yee, "Optimal linear data analysis for surface plasmon resonance biosensors," *Sensors and Actuators B: Chemical*, vol. 54, no. 1-2, pp. 89–97, 1999.

[9] M. Mar, B. Ratner, and S. Yee, "An intrinsically protein-resistant surface plasmon resonance biosensor based upon a RF-plasma-deposited thin film," *Sensors and Actuators B: Chemical*, vol. 54, no. 1-2, pp. 125–131, 1999.

[10] L. Jung, K. Nelson, C. Campbell, P. Stayton, S. Yee, V. Pérez-Luna, and G. López, "Surface plasmon resonance measurement of binding and dissociation of wild-type and mutant streptavidin on mixed biotin-containing alkylthiolate monolayers," *Sensors and Actuators B: Chemical*, vol. 54, no. 1-2, pp. 137–144, 1999.

[11] K. Kneipp, Y. Wang, H. Kneipp, L. Perelman, I. Itzkan, R. Dasari, and M. Feld, "Single molecule detection using surface-enhanced Raman scattering (SERS)," *Physical Review Letters*, vol. 78, no. 9, pp. 1667–1670, 1997.

[12] S. Nie and S. Emory, "Probing single molecules and single nanoparticles by surface-enhanced Raman scattering," *Science*, vol. 275, no. 5303, pp. 1102–1106, 1997.

[13] D. Courjon and C. Bainier, "Near field microscopy and near field optics," *Reports on Progress in Physics*, vol. 57, no. 10, pp. 989–1028, 1994.

[14] D. Pacifici, H. Lezec, and H. Atwater, "All-optical modulation by plasmonic excitation of CdSe quantum dots," *Nature Photonics*, vol. 1, pp. 402–406, 2007.

[15] M. Dicken, L. Sweatlock, D. Pacifici, H. Lezec, K. Bhattacharya, and H. Atwater, "Electrooptic modulation in thin film barium titanate plasmonic interferometers," *Nano Letters*, vol. 8, no. 11, pp. 4048–4052, 2008.

[16] J. Gosciniak, S. Bozhevolnyi, T. Andersen, V. Volkov, J. Kjelstrup-Hansen, L. Markey, and A. Dereux, "Thermo-optic control of dielectric-loaded plasmonic waveguide components," *Optics Express*, vol. 18, no. 2, pp. 1207–1216, 2010.

[17] V. V. Temnov, G. Armelles, U. Woggon, D. Guzatov, A. Ceballada, A. Garcia-Martin, J.-M. Garcia-Martin, T. Thomay, A. Leitenstorfer, and R. Bratschitsch, "Active magneto-plasmonics in hybrid metal-ferromagnet structures," *Nature Photonics*, vol. 4, pp. 107–111, 2010.

[18] D. Martín-Becerra, J. B. González-Díaz, V. V. Temnov, A. Ceballada, G. Armelles, T. Thomay, A. Leitenstorfer, R. Bratschitsch,

A. García-Martín, and M. U. González, "Enhancement of the magnetic modulation of surface plasmon polaritons in Au/Co/Au films," *Applied Physics Letters*, vol. 97, p. 183114, 2010.

[19] P. Drude, "On the electron theory of metals," *Annalen Der Physik*, vol. 1, no. 3, pp. 556–613, 1900.

[20] N. Christensen and B. Seraphin, "Relativistic band calculation and the optical properties of gold," *Physical Review B*, vol. 4, no. 10, pp. 3321–3344, 1971.

[21] N. Christensen, "The band structure of silver and optical interband transitions," *Physica Status Solidi (B)*, vol. 54, no. 2, pp. 551–563, 1972.

[22] M.-L. Thèye, "Investigation of the optical properties of Au by means of thin semitransparent films," *Physical Review B*, vol. 2, no. 8, pp. 3060–3078, 1970.

[23] R. Beach and R. Christy, "Electron-electron scattering in the intraband optical conductivity of Cu, Ag, and Au," *Physical Review B*, vol. 16, no. 12, pp. 5277–5284, 1977.

[24] G. Parkins, W. Lawrence, and R. Christy, "Intraband optical conductivity of $\sigma(\omega, t)$ of Cu, Ag, and Au: Contribution from electron-electron scattering," *Physical Review B*, vol. 23, no. 12, pp. 6408–6416, 1981.

[25] J. Smith and H. Ehrenreich, "Frequency dependence of the optical relaxation time in metals," *Physical Review B*, vol. 25, no. 2, pp. 923–930, 1982.

[26] M. Fox, *Optical Properties of Solids*. Oxford University Press, 2010.

[27] E. Kretschmann and H. Raether, "Radiative decay of nonradiative surface plasmons excited by light," *Z. Naturforsch. A*, vol. 23, p. 2135, 1968.

[28] D. Heitmann, "Radiative decay of surface plasmons excited by fast electrons on periodically modulated silver surfaces," *Journal of Physics C: Solid State Physics*, vol. 10, p. 397, 1977.

[29] R. Ritchie, "Plasma losses by fast electrons in thin films," *Physical Review*, vol. 106, pp. 874–881, 1957.

[30] G. Mie, "Beiträge zur optik trüber medien, speziell kolloidaler metallösungen," *Ann. Physik*, vol. 25, pp. 377–445, 1908.

[31] S. Acímović, M. Kreuzer, M. González, and R. Quidant, "Plasmon near-field coupling in metal dimers as a step toward single-molecule sensing," *ACS Nano*, vol. 3, no. 5, pp. 1231–1237, 2009.

[32] E. Ozbay, "Plasmonics: Merging photonics and electronics at nanoscale dimensions," *Science*, vol. 311, no. 5758, pp. 189–193, 2006.

[33] R. Zia, J. Schuller, A. Chandran, and M. Brongersma, "Plasmonics: The next chip-scale technology," *Materials Today*, vol. 9, pp. 20–27, 2006.

[34] J.-C. Weeber, Y. Lacroute, and A. Dereux, "Optical near-field distributions of surface plasmon waveguide modes," *Physical Review B*, vol. 68, p. 115401, 2003.

[35] A. Hohenau, J. Krenn, A. Stepanov, A. Drezet, H. Ditlbacher, B. Steinberger, A. Leitner, and F. Aussenegg, "Dielectric optical elements for surface plasmons," *Optics Letters*, vol. 30, no. 8, pp. 893–895, 2005.

[36] J.-C. Weeber, M. González, A.-L. Baudrion, and A.Dereux, "Surface plasmon routing along right angle bent metal strips," *Applied Physics Letters*, vol. 87, p. 221101, 2005.

[37] A. Krasavin and A. Zayats, "Passive photonic elements based on dielectric-loaded surface plasmon polariton waveguides," *Applied Physics Letters*, vol. 90, no. 21, p. 211101, 2007.

[38] T. Holmgaard, Z. Chen, S. Bozhevolnyi, L. Markey, A. Dereux, A. Krasavin, and A. Zayats, "Bend- and splitting loss of dielectric-loaded surface plasmon-polariton waveguides," *Optics Express*, vol. 16, no. 18, pp. 13585–13592, 2008.

[39] A. Drezet, D. Koller, A. Hohenau, A. Leitner, F. Aussenegg, and J. Krenn, "Plasmonic crystal demultiplexer and multiports," *Nano Letters*, vol. 7, no. 6, pp. 1697–1700, 2007.

[40] S. Bozhevolnyi, V. Volkov, E. Devaux, J.-Y. Laluet, and T. Ebbesen, "Channel plasmon subwavelength waveguide components including interferometers and ring resonators," *Nature*, vol. 440, pp. 508–511, 2006.

[41] W. Barnes, T. Preist, S. Kitson, and J. Sambles, "Physical origin of photonic energy gaps in the propagation of surface plasmons on gratings," *Physical Review B*, vol. 54, no. 9, pp. 6227–6244, 1996.

[42] S. Kitson, W. Barnes, and J. Sambles, "Full photonic band gap for surface modes in the visible," *Physical Review Letters*, vol. 77, no. 13, pp. 2670–2673, 1996.

[43] L. Feng, M.-H. Lu, V. Lomakin, and Y. Fainman, "Plasmonic photonic crystal with a complete band gap for surface plasmon plariton waves," *Applied Physics Letters*, vol. 93, no. 23, p. 231105, 2008.

[44] T. Okamoto, J. Simonen, and S. Kawata, "Plasmonic band gaps of structured metallic thin films evaluated for a surface plasmon laser using the coupled-wave approach," *Physical Review B*, vol. 77, no. 11, p. 115425, 2008.

[45] J. Sánchez-Gil and A. Maradudin, "Surface-plasmon polariton scattering from a finite array of nanogrooves/ridges: Efficient mirrors," *Applied Physics Letters*, vol. 86, no. 25, p. 251106, 2005.

[46] M. González, J.-C. Weeber, A.-L. Baudrion, A. Dereux, A. Stepanov, J. Krenn, E. Devaux, and T. Ebbesen, "Design, near-field characterization, and modeling of 45° surface-plasmon Bragg mirrors," *Physical Review B*, vol. 73, no. 15, p. 155416, 2006.

[47] M. González, A. Stepanov, J.-C. Weeber, A. Hohenau, A. Dereux, R. Quidant, and J. Krenn, "Analysis of the angular acceptance of surface plasmon Bragg mirrors," *Optics Letters*, vol. 32, no. 18, pp. 2704–2706, 2007.

[48] S. Bozhevolnyi, J. Erland, K. Leosson, P. Skovgaard, and J. Hvam, "Waveguiding in surface plasmon polariton band gap structures," *Physical Review Letters*, vol. 86, no. 14, pp. 3008–3011, 2001.

[49] A.-L. Baudrion, J.-C. Weeber, A. Dereux, G. Lecamp, P. Lalanne, and S. Bozhevolnyi, "Influence of the filling factor on the spectral

properties of plasmonic crystals," *Physical Review B*, vol. 74, no. 12, p. 125406, 2006.

[50] J.-C. Weeber, A.-L. Baudrion, A. Bouhelier, A. Bruyant, G. C. des Francs, R. Zia, and A. Dereux, "Efficient surface plasmon field confinement in one-dimensional crystal line-defect waveguides," *Applied Physics Letters*, vol. 89, no. 21, p. 211109, 2006.

[51] I. Radko, A. Evlyukhin, A. Boltasseva, and S. Bozhevolnyi, "Refracting surface plasmon polaritons with nanoparticle arrays," *Optics Express*, vol. 16, no. 6, pp. 3924–3930, 2008.

[52] G. Stegeman, N. Glass, A. Maradudin, T. Shen, and R. Wallis, "Fresnel relations for surface polaritons at interfaces," *Optics Letters*, vol. 8, no. 12, pp. 626–628, 1983.

[53] S. Griesing, A. Englisch, and U. Hartmann, "Refractive and reflective behavior of polymer prisms used for surface plasmon guidance," *Optics Letters*, vol. 33, no. 6, pp. 575–577, 2008.

[54] L. Feng, K. Tetz, B. Slutsky, V. Lomakin, and Y. Fainman, "Fourier plasmonics: Diffractive focusing of in-plane surface plasmon polariton waves," *Applied Physics Letters*, vol. 91, no. 8, p. 081101, 2007.

[55] Q. Wang, X. Yuan, P. Tan, and D. Zhang, "Phase modulation of surface plasmon polaritons by surface relief dielectric structures," *Optics Express*, vol. 16, no. 23, pp. 19271–19276, 2008.

[56] J. Grandidier, S. Massenot, G. C. des Francs, A. Bouhelier, J.-C. Weeber, L. Markey, A. Dereux, J. Renger, M. González, and R. Quidant, "Dielectric-loaded surface plasmon polariton waveguides: Figures of merit and mode characterization by image and Fourier plane leakage microscopy," *Physical Review B*, vol. 78, no. 24, p. 245419, 2008.

[57] K. MacDonald, Z. Sámson, M. Stockman, and N. Zheludev, "Ultrafast active plasmonics," *Nature Photonics*, vol. 3, pp. 55–58, 2009.

[58] G. Wiederrecht, J. Hall, and A. Bouhelier, "Control of molecular energy redistribution pathways via surface plasmon gating," *Physical Review Letters*, vol. 98, no. 9, p. 083001, 2007.

[59] R. Oulton, V. Sorger, T. Zentgraf, R.-M. Ma, C. Gladden, L. Dai, G. Bartal, and X. Zhang, "Plasmon lasers at deep subwavelength scale," *Nature*, vol. 461, pp. 629–632, 2009.

[60] A. Krasavin and A. Zayats, "Silicon-based plasmonic waveguides," *Optics Express*, vol. 18, no. 11, pp. 11791–11799, 2010.

[61] R. Briggs, J. Grandidier, S. Burgos, E. Feigenbaum, and H. Atwater, "Efficient coupling between dielectric-loaded plasmonic and silicon photonic waveguides," *Nano Letters*, vol. 10, no. 12, pp. 4851–4857, 2010.

[62] T. Holmgaard, Z. Chen, S. Bozhevolnyi, L. Markey, and A. Dereux, "Dielectric-loaded plasmonic waveguide-ring resonators," *Optics Express*, vol. 17, no. 4, pp. 2968–2975, 2009.

[63] J. Grandidier, G. C. des Francs, S. Massenot, A. Bouhelier, L. Markey, J.-C. Weeber, C. Finot, and A. Dereux, "Gain-assisted propagation in a plasmonic waveguide at telecom wavelength," *Nano Letters*, vol. 9, no. 8, pp. 2935–2939, 2009.

[64] A. Kumar, J. Gosciniak, T. Andersen, L. Markey, A. Dereux, and S. Bozhevolnyi, "Power monitoring in dielectric-loaded surface plasmon-polariton waveguides," *Optics Express*, vol. 19, no. 4, pp. 2972–2978, 2011.

[65] J. Fan, K. Bao, C. Wu, J. Bao, R. Bardhan, N. Halas, V. Manoharan, G. Shvets, P. Nordlander, and F. Capasso, "Fano-like interference in self-assembled plasmonic quadrumer clusters," *Nano Letters*, vol. 10, no. 11, pp. 4680–4685, 2010.

[66] R. Pala, K. Shimizu, N. Melosh, and M. Brongersma, "A nonvolatile plasmonic switch employing photochromic molecules," *Nano Letters*, vol. 8, no. 5, pp. 1506–1510, 2008.

[67] P. Evans, G. Wurtz, W. Hendren, R. Atkinson, W. Dickson, A. Zayats, and R. Pollard, "Electrically switchable nonreciprocal transmission of plasmonic nanorods with liquid crystal," *Applied Physics Letters*, vol. 91, p. 043101, 2007.

[68] R. Boyd, *Nonlinear Optics*. Academic Press, 3rd ed., 2008.

[69] M. Nevière and E. Popov, *Light Propagation in Periodic Media: Differential Theory and Design*. Marcel Dekker, Inc., 2003.

[70] L. Li, "Formulation and comparison of two recursive matrix algorithms for modeling layered diffraction gratings," *Journal of the Optical Society of America A*, vol. 13, no. 5, pp. 1024–1035, 1996.

[71] M. Kretschmann, T. Leskova, and A. Maradudin, "Conical propagation of a surface polariton across a grating," *Optics Communications*, vol. 215, no. 4-6, pp. 205–223, 2003.

[72] A. Nikitin and L. Martín-Moreno, "Scattering coefficients of surface plasmon polaritons impinging at oblique incidence onto one-dimensional surface relief defects," *Physical Review B*, vol. 75, no. 8, p. 081405, 2007.

[73] A. Bouhelier and G. Wiederrecht, "Surface plasmon rainbow jet," *Optics Letters*, vol. 30, no. 8, pp. 884–886, 2005.

[74] A. Drezet, A. Hohenau, A. Stepanov, H. Ditlbacher, B. Steinberger, N. Galler, F. Aussenegg, A. Leitner, and J. Krenn, "How to erase surface plasmon fringes," *Applied Physics Letters*, vol. 89, no. 9, p. 091117, 2006.

[75] S. Massenot, J. Grandidier, A. Bouhelier, G. C. des Francs, L. Markey, J.-C. Weeber, A. Dereux, J. Renger, M. González, and R. Quidant, "Polymer-metal waveguides characterization by Fourier plane leakage radiation microscopy," *Applied Physics Letters*, vol. 91, no. 24, p. 243102, 2007.

[76] A. Stepanov, J. Krenn, H. Ditlbacher, A. Hohenau, A. Drezet, B. Steinberger, A. Leitner, and F. Aussenegg, "Quantitative analysis of surface plasmon interaction with silver nanoparticles," *Optics Letters*, vol. 30, no. 12, pp. 1524–1526, 2005.

[77] A. Giannattasio and W. Barnes, "Direct observation of surface pplasmon-polariton dispersion," *Optics Express*, vol. 13, no. 2, pp. 428–434, 2005.

[78] J. Renger, S. Grafström, and L. Eng, "Direct excitation of surface plasmon polaritons in nanopatterned metal surfaces and thin films," *Physical Review B*, vol. 76, no. 4, p. 045431, 2007.

[79] S. Bozhevolnyi, *Plasmonic Nanoguides and Circuits*. Pan Stanford, 2008.

[80] T. Holmgaard, S. Bozhevolnyi, L. Markey, and A. Dereux, "Dielectric-loaded surface plasmon-polariton waveguides at telecommunication wavelengths: Excitation and characterization," *Applied Physics Letters*, vol. 92, no. 1, p. 011124, 2008.

[81] T. Holmgaard, Z. Chen, S. Bozhevolnyi, L. Markey, A. Dereux, A. Krasavin, and A. Zayats, "Wavelength selection by dielectric-loaded plasmonic components," *Applied Physics Letters*, vol. 94, no. 5, p. 051111, 2009.

[82] A. Krasavin and A. Zayats, "All-optical active components for dielectric-loaded plasmonic waveguides," *Optics Communications*, vol. 283, no. 8, pp. 1581–1584, 2010.

[83] T. Holmgaard, S. Bozhevolnyi, L. Markey, A. Dereux, A. Krasavin, P. Bolger, and A. Zayats, "Efficient excitation of dielectric-loaded surface plasmon-polariton waveguide modes at telecommunication wavelengths," *Physical Review B*, vol. 78, no. 16, p. 165431, 2008.

[84] A. Yariv, "Universal relations for coupling of optical power between microresonators and dielectric waveguides," *Electronic Letters*, vol. 36, no. 4, pp. 321–322, 2000.

[85] W. Barnes, A. Dereux, and T. Ebbesen, "Surface plasmon subwavelength optics," *Nature*, vol. 424, pp. 824–830, 2003.

[86] O. Tsilipakos and E. Kriezis, "Microdisk resonator filters made of dielectric-loaded plasmonic waveguides," *Optics Communications*, vol. 283, no. 15, pp. 3095–3098, 2010.

[87] K. Oda, N. Takato, and H. Toba, "A wide-FSR waveguide double-ring resonator for optical FDM transmission systems," *Journal of Lightwave Technology*, vol. 9, no. 6, pp. 728–736, 1991.

[88] M. Popovic, C. Manolatou, and M. Watts, "Coupling-induced resonance frequency shifts in coupled dielectric multi-cavity filters," *Optics Express*, vol. 14, no. 3, pp. 1208–1222, 2006.

[89] T. Nikolajsen, K. Leosson, and S. Bozhevolnyi, "Surface plasmon polariton based modulators and switches operating at telecom wavelengths," *Applied Physics Letters*, vol. 85, no. 24, pp. 5833–5835, 2004.

[90] B. Steinberger, A. Hohenau, H. Ditlbacher, A. Stepanov, A. Drezet, F. Aussenegg, A. Leitner, and J. Krenn, "Dielectric stripes on gold as surface plasmon waveguides," *Applied Physics Letters*, vol. 88, no. 9, p. 094104, 2006.

[91] B. Hecht, H. Bielefeldt, L. Novotny, Y. Inouye, and D. Pohl, "Local excitation, scattering, and interference of surface plasmons," *Physical Review Letters*, vol. 77, no. 9, pp. 1889–1892, 1996.

[92] P. Guenter, *Nonlinear Optical Effects and Materials*. Springer Series in Optical Sciences, Vol. 72, Springer-Verlag, 2000.

[93] H. Nalwa and S. Miyata, *Nonlinear Optics of Organic Molecules and Polymers*. CRC Press, 1997.

[94] K. Singer, M. Kuzyk, and J. Sohn, "Second-order nonlinear-optical processes in orientationally ordered materials: Relationship between molecular and macroscopic properties," *Journal of the Optical Society of America B*, vol. 4, no. 6, pp. 968–976, 1987.

[95] Y. Enami, C. Derose, D. Mathine, C. Loychik, C. Greenlee, R. Norwood, T.-D. Kim, J. Luo, Y. Tian, A.-Y. Jen, and N. Peyghambarian, "Hybrid polymer/sol-gel waveguide modulations with exceptionally large electro-optic coefficients," *Nature Photonics*, vol. 1, pp. 180–185, 2007.

[96] T.-D. Kim, J. Luo, J.-W. Ka, S. Hau, Y. Tian, Z. Shi, N. Tucker, S.-H. Jang, J.-W. Kang, and A.-Y. Jen, "Ultralarge and thermally stable electro-optic activities from Diels-Alder crosslinkable polymers containing binary chromophore systems," *Advanced Materials*, vol. 18, no. 22, pp. 3038–3042, 2006.

[97] M. Hochberg, T. Baehr-Jones, G. Wang, J. Huang, P. Sullivan, L. Dalton, and A. Scherer, "Towards a millivolt optical modulator with nano-slot waveguides," *Optics Express*, vol. 15, no. 13, pp. 8401–8410, 2007.

[98] C. Hernandez, *Photorefractive Polymer Composites with Improved Operational Stability and Performance*. PhD thesis, The University of Arizona, 2004.

[99] C. Teng and H. Man, "Simple reflection technique for measuring the electro-optic coefficient of poled polymers," *Applied Physics Letters*, vol. 56, no. 18, pp. 1734–1736, 1990.

[100] Y. Jiang, Z. Cao, G. Chen, X. Dou, and Y. Chen, "Low voltage electro-optic polymer light modulator using attenuated total internal reflection," *Optics & Laser Technology*, vol. 33, no. 6, pp. 417–420, 2001.

[101] F. Robin, S.Costea, G. Stark, R. Wüest, P. Strasser, H. Jäckel, A. Rampe, M. Levermann, and G. Piaszenski, "Accurate proximity-effect correction of nanoscale structures with nanoPECS," *Raith Application Note*, pp. 1–4, 2006.

[102] C. Nguyen, R. Hierle, and J. Zyss, "New electro-optic modulator based on polymer waveguide and loop structure," vol. 5351 of *Proceedings of SPIE*, 2004.

[103] S. Michel, J. Zyss, I. Ledoux-Rak, and C. Nguyen, "High-performance electro-optic modulators realized with a commercial side-chain DR1-PMMA electro-optic copolymer," vol. 7599 of *Proceedings of SPIE*, 2010.

[104] D. Perron, M. Wu, C. Horvath, D. Bachman, and V. Van, "All-plasmonic switching based on thermal nonlinearity in a polymer plasmonic microring resonator," *Optics Letters*, vol. 36, no. 14, pp. 2731–2733, 2011.

[105] K. Ohara, M. Hennecke, and J. Fuhrmann, "Electrostriction of polymethylmethacrylates," *Colloid & Polymer Science*, vol. 260, no. 2, pp. 164–168, 1982.

[106] A. Krasavin and N. Zheludev, "Active plasmonics: Controlling signals in Au/Ga waveguide using nanoscale structural transformations," *Applied Physics Letters*, vol. 84, no. 8, pp. 1416–1418, 2004.

[107] K. Yager and C. Barrett, "Novel photo-switching using azobenzene functional materials," *Journal of Photochemistry and Photobiology A: Chemistry*, vol. 182, no. 3, pp. 250–261, 2006.

[108] R. Loucif-Saibi, K. Nakatani, J. Delaire, M. Dumont, and Z. Sekkat, "Photoisomerization and second harmonic generation in disperse red one-doped and -functionalized poly(methyl methacrylate) films," *Chemistry of Materials*, vol. 5, no. 2, pp. 229–236, 1993.

[109] Z. Sekkat, D. Morichère, M. Dumont, R. Loucif-Saibi, and J. Delaire, "Photoisomerization of azobenzene derivatives in polymeric thin films," *Journal of Applied Physics*, vol. 71, no. 3, pp. 1543–1545, 1992.

[110] F.-S. Chien, C. Lin, and C. Hsu, "Local photo-assisted poling of azo copolymer films by scanning probe microscopy," *Journal of Physics D: Applied Physics*, vol. 41, no. 23, p. 235502, 2008.

[111] M. Dumont and Z. Sekkat, "Dynamical study of photoinduced anisotropy and orientational relaxation of azo dyes in polymeric films: poling at room temperature," vol. 1774 of *Proceedings of SPIE*, 1993.

[112] I. Lednev, T.-Q. Ye, R. Hester, and J. Moore, "Femtosecond time-resolved UV-visible absorption spectroscopy of trans-azobenzene in solution," *The Journal of Physical Chemistry*, vol. 100, no. 32, pp. 13338–13341, 1996.

[113] R. Rangel-Rojo, S. Yamada, H. Matsuda, and D. Yankelevich, "Large near-resonance third-order nonlinearity in an azobenzene-functionalized polymer film," *Applied Physics Letters*, vol. 72, no. 9, p. 1021, 1998.

[114] D. Zhang, X.-C. Yuan, A. Bouhelier, G. Yuan, P. Wang, and H. Ming, "Active control of surface plasmon polaritons by optical isomerization of an azobenzene polymer film," *Applied Physics Letters*, vol. 95, no. 10, p. 101102, 2009.

[115] J.-S. Bouillard, S. Vilain, W. Dickson, and A. Zayats, "Hyperspectral imaging with scanning near-field optical microscopy: Applications in plasmonics," *Optics Express*, vol. 18, no. 16, pp. 16513–16519, 2010.

[116] W. Rechberger, A. Hohenau, A. Leitner, J. Krenn, B. Lamprecht, and F. Aussenegg, "Optical properties of two interacting gold

nanoparticles," *Optics Communications*, vol. 220, no. 1-3, pp. 137–141, 2003.

[117] H. Miyazaki and Y. Kurokawa, "Squeezing visible light waves into a 3-nm-thick and 55-nm-long plasmon cavity," *Physical Review Letters*, vol. 96, no. 9, p. 097401, 2006.

[118] M. Kuttge, F. J. G. a de Abajo, and A. Polman, "Ultrasmall mode volume plasmonic nanodisk resonators," *Nano Letters*, vol. 10, no. 5, pp. 1537–1541, 2010.

[119] J. Swiatkiewicz, P. Prasad, and F. Karasz, "Anisotropy in the complex refractive index and the third-order nonlinear optical susceptibility of a stretch-oriented film of poly(p-phenylene vinylene)," *Journal of Applied Physics*, vol. 74, pp. 525–530, 1993.

[120] A. Samoc, M. Samoc, M. Woodruff, and B. Luther-Davies, "Tuning the properties of poly(pphenylenevinylene) for use in all-optical switching," *Optics Letters*, vol. 20, pp. 1241–1243, 1995.

[121] R. Gordon, "Reflection of cylindrical surface waves," *Optics Express*, vol. 17, no. 21, pp. 18621–18629, 2009.

[122] M. Samoc, A. Samoc, and B. Luther-Davies, "Third harmonic autocorrelation and wave mixing in a thin film of poly(p-phenylenevinylene)," *Optics Express*, vol. 11, no. 15, pp. 1787–1792, 2003.

[123] R. Berera, R. van Grondelle, and J. Kennis, "Ultrafast transient absorption spectroscopy: principles and application to photosynthetic systems," *Photosynthesis Research*, vol. 101, no. 2-3, pp. 105–118, 2009.

[124] H. Ehrenreich and H. Philipp, "Optical properties of Ag and Cu," *Physical Review*, vol. 128, no. 4, pp. 1622–1629, 1962.

[125] P. Johnson and R. Christy, "Optical constants of the noble metals," *Physical Review B*, vol. 6, no. 12, pp. 4370–4379, 1972.

[126] N. Ashcroft and N. Mermin, *Solid State Physics*. Harcourt Brace, 1976.

[127] W. Fann, R. Storz, H. Tom, and J. Bokor, "Direct measurement of nonequilibrium electron-energy distributions in subpicosecond laser-heated gold films," *Physical Review Letters*, vol. 68, no. 18, pp. 2834–2837, 1992.

[128] C. Schmuttenmaer, A. Aeschlimann, H. Elsayed-Ali, R. Miller, D. Mantell, J. Cao, and Y. Gao, "Time-resolved two-photon photoemission from Cu(100): Energy dependence of electron relaxation," *Physical Review B*, vol. 50, no. 12, pp. 8957–8960, 1994.

[129] R. Knorren, K. Bennemann, R. Burgermeister, and M. Aeschlimann, "Dynamics of excited electrons in copper and ferromagnetic transition metals: Theory and experiment," *Physical Review B*, vol. 61, no. 14, pp. 9427–9440, 2000.

[130] R. Rosei and D. Lynch, "Thermomodulation spectra of Al, Au, and Cu," *Physical Review B*, vol. 5, no. 10, pp. 3883–3894, 1972.

[131] R. Rosei, F. Antonangeli, and U. Grassano, "d bands Position and width in gold from very low temperature thermomodulation measurements," *Surface Science*, vol. 37, pp. 689–699, 1973.

[132] S. Link, C. Burda, Z. Wang, and M. El-Sayed, "Electron dynamics in gold and gold–silver alloy nanoparticles: The influence of a nonequilibrium electron distribution and the size dependence of the electron–phonon relaxation," *Journal of Chemical Physics*, vol. 111, no. 3, p. 1255, 1999.

[133] J. Hodak, A. Henglein, and G. Hartland, "Electron-phonon coupling dynamics in very small (between 2 and 8nm diameter) Au nanoparticles," *Journal of Chemical Physics*, vol. 112, no. 13, p. 5942, 2000.

[134] J. Hodak, I. Martini, and G. Hartland, "Ultrafast study of electron–phonon coupling in colloidal gold particles," *Chemical Physics Letters*, vol. 284, no. 1-2, pp. 135–141, 1998.

[135] H. Inouye, K. Tanaka, I. Tanahashi, and K. Hirao, "Ultrafast dynamics of nonequilibrium electrons in a gold nanoparticle system," *Physical Review B*, vol. 57, no. 18, pp. 11334–11340, 1998.

[136] J.-Y. Bigot, V. Haltè, J.-C. Merle, and A. Daunios, "Electron dynamics in metallic nanoparticles," *Chemical Physics*, vol. 25, no. 1-3, pp. 181–203, 2000.

[137] G. Wiederrecht, G. Wurtz, and A. Bouhelier, "Ultrafast hybrid plasmonics," *Chemical Physics Letters*, vol. 461, no. 4-6, pp. 171–179, 2008.

[138] S. Frolov, Z. Bao, M. Wohlgenannt, and Z. Vardeny, "Excited-state relaxation in π-conjugated polymers," *Physical Review B*, vol. 65, no. 20, p. 205209, 2002.